Ultrashort Pulse Excitation of Dense Upconversion Media

Principal Investigator: Stephen C. Rand

Division of Applied Physics
Randall Laboratory
University of Michigan, Ann Arbor, MI 48109-1120

FINAL TECHNICAL REPORT
(Report Period: 3/1/96-6/30/97)

November 10, 1997

19971217 071

REPORT DOCUMENTATION PAGE

Public reporting burden for this collection of information is estimated to average 1 hour per response, including the time for reviewing instructions, searching existing data sources, gathering and maintaining the data needed, and completing and reviewing the collection of information. Send comments regarding this burden estimate or any other aspect of this collection of information, including suggestions for reducing this burden, to Washington Headquarters Services, Directorate for information Operations and Reports, 1215 Jefferson Davis Highway, Suite 1204, Arlington, VA 22202-4302, and to the Office of Management and Budget, Paperwork Reduction Project (0704-0188), Washington, DC 20503.

1. AGENCY USE ONLY (Leave blank)	2. REPORT DATE	3. REPORT TYPE AND DATES COVERED
		Final 01 Nov 96 to 30 Jun 97

4. TITLE AND SUBTITLE

Ultrashort Pulse Excitation of Dense Upconversion Media

5. FUNDING NUMBERS

Grant
AFOSR
F49620-96-1-0076

61102F
2301/CS

6. AUTHOR(S)

Stephen C. Rand

7. PERFORMING ORGANIZATION NAME(S) AND ADDRESS(ES)

The Regents of the University of Michigan
DRDA   3003 S. State Street
        Wolverine Tower, Room 1058
        Ann Arbor, MI 48109-1274

8. PERFORMING ORGANIZATION REPORT NUMBER

DRDA 960589

9. SPONSORING/MONITORING AGENCY NAME(S) AND ADDRESS(ES)

United States Air Force
Air Force Office of Scientific Research
Building AFB, DC 20332-0001

10. SPONSORING/MONITORING AGENCY REPORT NUMBER

11. SUPPLEMENTARY NOTES

12a. DISTRIBUTION/AVAILABILITY STATEMENT

Approved for public release; distribution unlimited.

12b. DISTRIBUTION CODE

13. ABSTRACT (Maximum 200 words)

This project was initiated to identify conditions in dense upconversion media under which ultrashort pulses could lead to new applications. Four main results were obtained. First, a new channel for the generation of ultraviolet upconversion emission in Erbium-doped compounds was discovered. Second, an extremely promising imaging technique which relies on time-gated, ultrafast upconversion was demonstrated. Third, induced nonlinear response in dense upconversion materials was shown to be primarily dispersive in nature, even for resonant interactions, and we were able to explain how this apparently contradictory behavior arises. This revealed for the first time that cooperative nonlinearities could be useful in lossless, ultrafast applications. Fourth, a local mode of Yb in $CsCdBr_3$ crystals was identified with properties which should permit coherent control of upconversion by ultrashort pulses.

14. SUBJECT TERMS

Upconversion, ultrafast science, ultrashort pulses, imaging

15. NUMBER OF PAGES

16. PRICE CODE

17. SECURITY CLASSIFICATION OF REPORT	18. SECURITY CLASSIFICATION OF THIS PAGE	19. SECURITY CLASSIFICATION OF ABSTRACT	20. LIMITATION OF ABSTRACT
UNCLASSIFIED	UNCLASSIFIED	UNCLASSIFIED	UL

NSN 7540-01-280-5500

Standard Form 298 (Rev 2-89)

Abstract

This project was initiated to identify conditions in dense upconversion media under which ultrashort pulses could lead to new applications. Four main results were obtained. First, a new channel for the generation of ultraviolet upconversion emission in Erbium-doped compounds was discovered. Second, an extremely promising imaging technique which relies on time-gated, ultrafast upconversion was demonstrated. Third, induced nonlinear response in dense upconversion materials was shown to be primarily dispersive in nature, even for *resonant interactions*, and we were able to explain how this apparently contradictory behavior arises. This revealed for the first time that cooperative nonlinearities could be useful in lossless, ultrafast applications. Fourth, a local mode of Yb in $CsCdBr_3$ crystals was identified with properties which should permit coherent control of upconversion by ultrashort pulses.

Table of Contents

1. Introduction

Upconversion processes in condensed matter are generally divided into two types, with a distinction being drawn on the basis of whether energy is or is not absorbed in the medium. This division depends on whether incident light initiates population dynamics or not. In the case of excitation by light at resonant wavelengths one speaks of non-parametric upconversion, and relatively efficient redistribution of energy can occur within a medium as the result of atomic transitions of its constituents, generally after a delay determined by the timescale of internal transitions within the system. For non-resonant excitation, parametric upconversion can occur. This is usually less efficient, but the response is essentially instantaneous.

In this project we investigated both types of upconversion using ultrashort pulses, with two new applications in mind. First, we performed comparative spectroscopy with continuous-wave (cw) and ultrashort pulse lasers to search for new channels of excitation which might improve the prospects for non-parametric gain in the ultraviolet spectral region. The immense bandwidth of femtosecond pulses is expected to cause striking changes in the multi-photon absorption efficiency of *some systems*, by improving the overall spectral overlap of upconversion processes involving several non-resonant steps. Improvements would permit the realization of compact, solid state ultraviolet laser sources. Second, we investigated the application of upconversion for improved detection of signals in time-gated imagery of objects obscured by scattering media. Non-parametric and parametric upconversion were compared in this application for their ability to isolate the wavelength of the image-bearing signal from scattered light at the incident wavelength. Background light is the chief limitation to existing methods of optically imaging through highly scattering media.

2. Experimental Methods

2.1. Laser Sources

(i) Two existing, mode-locked Ti:sapphire lasers were used for most of the experiments reported here. Both were free-running homemade sources in which the mode-locking mechanism was passive Kerr-lens modulation. Dispersion compensation with prisms in one instrument resulted in stable pulses of approximately 100 fs duration. A short gain medium, special mirrors and third order compensation in the second instrument resulted in output pulses of 30 fs duration.

The first source was easily inter-convertible between cw and mode-locked operation. As a result it was used for experiments designed to compare non-parametric upconversion in crystals excited by either continuous or pulsed light. The second source, producing 30 fs pulses, was dedicated to imaging experiments requiring the shortest possible optical gating signal.

4

(ii) Finally, an optical parametric generator and a white light continuum generator were used as femtosecond tunable light sources for two experiments in Pr-doped and Tm-doped materials. These measurements required two different wavelengths to initiate upconversion processes.

The objective in this part of the project was to test a new detector concept requiring two synchronous pulses of different wavelengths resonant with transitions of the chosen ion. For Pr we used a parametric generator pumped by a regeneratively amplified Ti:sapphire laser system at 800 nm. Wavelengths near 800 nm and 1010 nm were obtained from the pump and signal beams. For Tm studies, wavelengths near 650 nm and 800 nm were needed. In this case, the red beam was obtained by filtering the output of a white light continuum obtained by doubling the pump and focusing into a sapphire platelet. In both experiments, input beams were then combined collinearly with the output of the filtered white light cell to form the required 2-color excitation source. Pulse repetition rate of the source was variable between 0.1-10 MHz and relative delay between pulse trains at the two wavelengths was controlled in the usual way with a mechanical delay stage.

2.2 Time-gated Upconversion Imaging

For experiments on upconversion imaging, the output of the 30 fs Ti:sapphire laser was divided into two beams. One beam was magnified and used to illuminate the object. The second served as the timing reference, or gating beam, and also contained a telescope for adjustable wavefront control. As indicated in Fig. 1, these beams were combined using Type I noncollinear phase-matching to provide complete spatial isolation of the cross-correlated signal beam. The signal beam emerged along the bisector of the object and gating beams when the relative delay of these beams was less than 100 fs. It then passed through an iris which blocked light from second harmonic generation of the individual fundamental beams. A dichroic notch filter provided further isolation from scattered light at the fundamental wavelength.
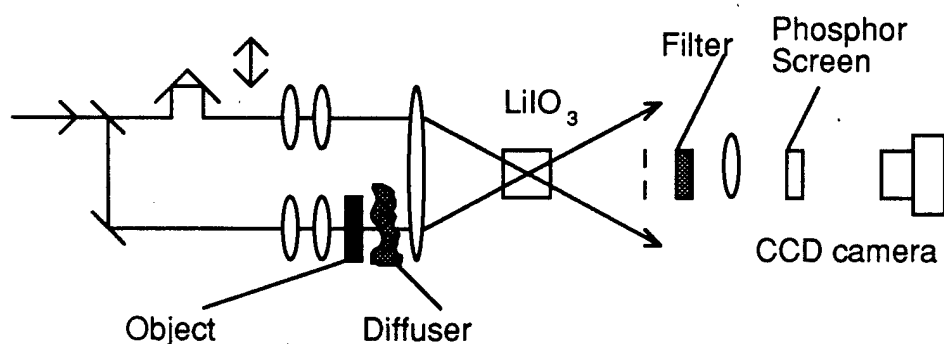

Fig. 1. Imaging apparatus to demonstrate imaging through highly scattering media using time-gated upconversion of 800 nm light to a wavelength of 400 nm in a crystal of $LiIO_3$. Delay of the gating (reference) pulse was controlled with a mechanical translation stage and a secondary image formed on a phosphorescent screen.

Signal light was relayed with an imaging lens to a phosphorescent screen fabricated on a glass slide with a thin layer of red fluorescent paint. This screen converted the image from the SHG wavelength of 400 nm to the 600 nm region, thereby permitting efficient matching to the spectral response of the detector in transmission. This also retained an in-line, transmissive geometry. Images were recorded electronically with a CCD camera as a function of delay between the incident beams.

2.3 Resonance Raman Spectroscopy in Dense Upconversion Media

A cw Ti:sapphire laser which was tunable in the 900-1000 nm region was used to perform resonance Raman spectroscopy of a new class of dense upconversion materials. The goal of this part of the project was to see if coherent control of upconversion might be possible, by developing an understanding of the vibrational interactions between rare earth impurities and their nearest neighbors during the interval of time immediately following interaction with an ultrafast pulse. This information is contained in the "local mode" portion of the Raman spectrum, and can be identified by spectroscopy on and off resonance with the species of interest.

First, high resolution absorption spectra of $Yb^{3+}:CsCdBr_3$ single crystals were recorded at 12 K, using a double beam spectrophotometer. The laser was then tuned to wavelengths near the various Stark components of infrared absorption lines of the Yb^{3+} ions. At each wavelength the complete Raman spectrum was recorded. Then, spectra were compared for evidence of features not contained in the host crystal Raman spectrum, "local modes" excited in conjunction with the cooperative upconversion processes of interest in this project. Local modes were expected to exhibit resonant enhancement near dipole-allowed absorptive transitions of the Yb impurity ions, and indeed one such mode was identified in spectra taken at liquid helium temperature.

3. Results

3.1. Discovery of Er Upconversion in the Red Spectral Region

While performing spectroscopic comparisons of upconversion generated by cw and pulsed excitation in $Er:LiYF_4$ crystals, a new upconversion channel in the red spectral region was discovered. The fluorescence emission spectrum and the unexpected wavelength which gave rise to it are indicated in Fig. 2.

Although the excitation wavelength corresponded precisely to an excited state-excited state transition of Erbium in a wavelength region quite isolated from ground state absorption, we found no evidence that the upconversion mechanism was of the "avalanche" type. That is, no threshold was observed for upconversion emission. Instead a smooth quadratic dependence on incident light intensity was measured experimentally.
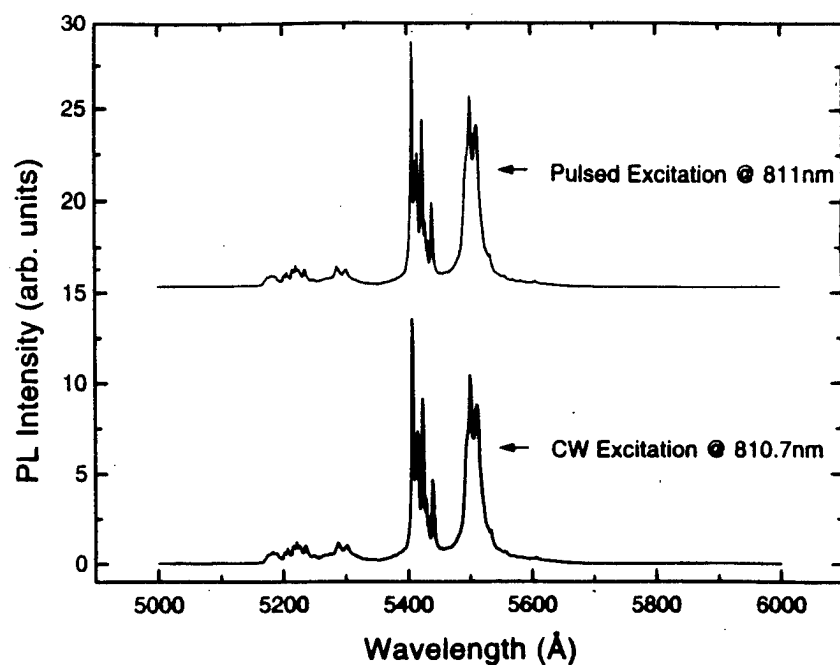
6

Figure 2(a). Upconversion fluorescence spectra of Er:LiYF$_4$ excited with laser light from a Ti:sapphire laser operated in both cw and mode-locked conditions.
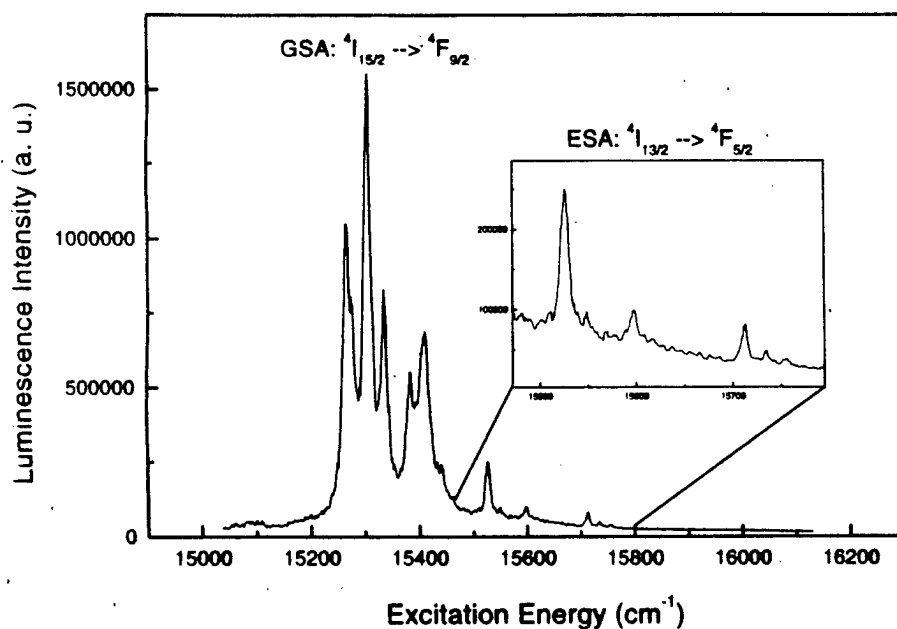

Figure 2(b). Fluorescence excitation spectrum of ultraviolet upconversion in Er:LiYF$_4$, showing the excited state resonance channel in the red spectral region.

The importance of this discovery is that it extends the list of ions which can potentially produce ultraviolet laser emission via upconversion of red pump light in the range 600-670 nm, through avalanche and other mechanisms, to include Nd, Pr, Tm, and Er.

3.2. Demonstration of Time-gated Upconversion Imaging

In recent years a number of techniques have emerged which successfully permit optical imaging through moderately opaque media. One technique uses ultrafast time-gating to select the least-scattered light from light pulses transmitted weakly through such media. However, an important limitation of such approaches arises from the inescapable presence of scattered light at the fundamental wavelength and intensity imbalances. In an attempt to circumvent this limitation, we investigated parametric upconversion of the image as a way to improve its contrast.

Our current extension of the time-gated imaging methodology captures the entire image in a single shot. No electronic processing of holographic fringe information is necessary, because we do not form a hologram in this approach. A real image is carried on the output wave resulting from cross-correlation of the 800 nm reference pulses and the object wave in a $LiIO_3$ crystal. This is simply imaged at 400 nm onto a transmissive phosphor screen monitored by a CCD camera. Details of the experiment and the results are given in the Appendix.

Two significant advantages have been identified for this approach to optical imaging through semi-opaque media. The first is that high quality images can be obtained directly, without the need for any electronic image processing, through diffusers which are severe enough to eliminate the "ballistic" component in transmitted light. The second is that the image is formed as the result of an intensity-intensity correlation process which reduces the sensitivity of the pattern in the image plane to phase fluctuations of the optical fields. This is advantageous, because the changes in speckle background which require averaging in imagery through dynamic scatterers when other methods are used are not present with this approach. In addition, theoretical considerations suggest that a version of our experiment in which the incident reference pulses are at the SHG wavelength instead of at the fundamental may have far more object specificity in dynamic scattering media (or in situations where phase contrast imagery is desired) than any existing technique.

3.3. Population Bottlenecks in 2-Color Upconversion

Non-parametric upconversion was also investigated as a potential method to isolate the detected image signal from light at the fundamental wavelength. The original concept was to use a Pr^{3+}-doped crystal or glass sample as an ultrafast gatable detector screen in front of a CCD camera. By forming an image at the upconversion wavelength instead of the fundamental wavelength, using resonant transitions of the dopant ions to provide reasonable efficiency, improved image contrast was expected. In this case, in order to preserve ultrafast gating capability, a 2-color approach was needed, as indicated in Fig. 3. One beam tuned to a ground state transition wavelength was to serve as the object beam

8

and the second beam was intended to upconvert the "first-excited ions" bearing image information from the "first-arriving light" through the diffuser medium.
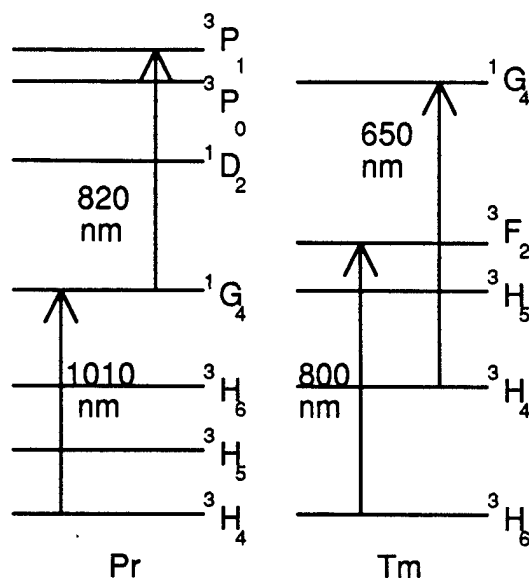

Figure 3. Schemes for non-parametric upconversion gating with Pr and Tm ions.

The wavelengths required for Pr:glass and Pr:LiYF$_4$ were successfully generated using the OPG source described earlier. It was intended that the $^1G_4$ state of Pr be used as the intermediate state in a resonant, two-photon absorption process because its lifetime was known to be short. Hence population was not expected to accumulate in this state between pulses and high repetition rates could be anticipated.

Unfortunately, the oscillator strength of the $^3H_4$-$^1G_4$ transition in both Pr:glass and Pr:LiYF$_4$ was so small that insufficient absorption of the OPG light occurred. This was confirmed in infrared absorption scans around the 1 micron region in both samples (Fig. 4 and 5). Blue upconversion emission intensity even at zero delay between the incident pulse trains was inadequate for imaging. To solve this problem we turned to another ion known to have a transition wavelength compatible with Ti:sapphire excitation which could combine with excitation at a second wavelength to yield very bright luminescence from a higher-lying state.

The wavelengths for excitation of Tm:LiYF$_4$ were generated from the fundamental beam of the Ti:sapphire system combined with filtered continuum light as described ealier. In this case the excitation dynamics were somewhat different. The 650 nm beam had to be maintained at a low average intensity to prevent avalanche upconversion from occurring, and several intervening states lay between the final state of the λ_1 transition and the initial state of the λ_2 transition.
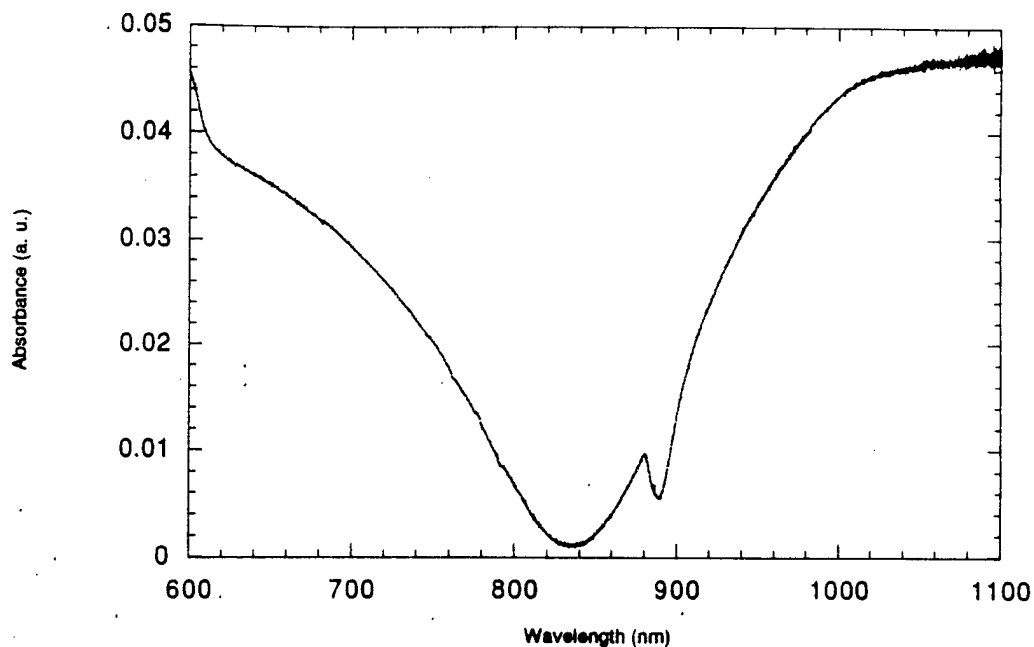
Figure 4. Enlargement of the unpolarized infrared absorption spectrum of Pr:glass (no baseline correction applied). No Pr features are observable near 1.0 μm.
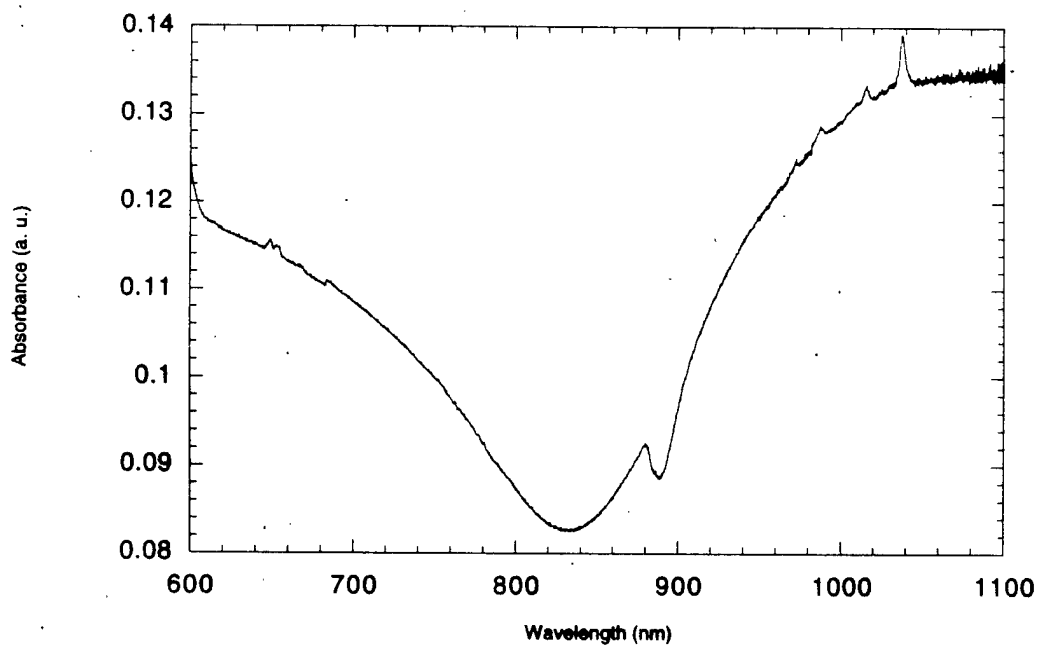

Figure 5. Enlargement of the unpolarized infrared absorption spectrum of Tm:LiYF$_4$ (no baseline correction applied). Spectral features near 1.0 μm are $^3H_4$-$^1G_4$ Pr transitions.

10

In this case, strong blue upconversion emission which required the presence of both beams was indeed observed. However two new problems were encountered in the Tm system. First, the decay $^3F_2$-$^3H_4$ was too slow and the lifetime of $^3H_4$ was too long. First-excited ions undoubtedly became interleaved in time with late-excited ions during the interstate decay. Second, the millisecond-scale lifetime of the $^3H_4$ state caused a bottleneck of population bearing "late-arriving light" information from *previous* pulses to accumulate in the level from which ultrafast upconversion gating was desired. This placed a severe restriction on the inter-pulse duty cycle which was acceptable. Unfortunately our laser source could not operate below a repetition rate of approximately 0.1 MHz. Nor did the CCD camera have enough intensity to image light gated from single pulse events.

Successful implementation of the concept of 2-color, non-parametric upconversion detection would necessitate that three basic requirements be met simultaneously. First, strong oscillator strengths are needed on the optical transitions. Second, the two-step absorption should ideally not involve relaxation of the intermediate state. Third, the lifetime of the intermediate state should be short, so as to avoid population bottlenecking. Hence in future work, different dopant ions and different transition combinations need to be considered for increased brightness. Also, host media which provide short excited state lifetimes should be sought.

3.4. Local Modes, All-optical Switching and Coherent Control of Upconversion in Dense Media

Non-parametric upconversion requires the interaction of pairs of dopant ions and phonons occasionally play a crucial, controlling role in some upconversion processes. For example, non-radiative processes play a dominant role in determining the efficiency of avalanche upconversion in Tm:LiYF$_4$[1]. All-optical switching has been demonstrated in systems of this type. Hence it is reasonable to assume that if the local modes of rare earth ions differ substantially from vibrational modes of the host lattice, some measure of control might be exercised over upconversion processes by controlling local mode excitation with short pulse techniques. Thus, it should be possible to exert coherent control over upconversion processes, and it may be possible to control the all-optical switching of cooperative upconversion using ultrafast pulse-shaping or other techniques. In the final stage of this project we therefore examined the local modes of Yb:CsCdBr$_3$ to see whether in this exemplary upconversion material a dominant mode could be identified, and whether it was well-isolated from host vibrational frequencies.

The main results obtained by Raman spectroscopy in Yb:CsCdBr$_3$ crystals are shown in Fig. 6. These were obtained using facilities at Los Alamos National Laboratory (details in the Appendix). The figure clearly shows the frequency of a dominant local mode of Yb ions in this material to be very different from that of host modes which are understandably more intense. The Yb absorption spectrum exhibits the same mode. This suggests that ultrafast pulse-shaping could be applied to excite this mode deliberately to enhance upconversion processes mediated by phonons in the first step of dynamic energy relaxation

11

in such an upconversion system. Thus we have identified a potential host material and a pathway with which to investigate coherent control of upconversion in dense media.
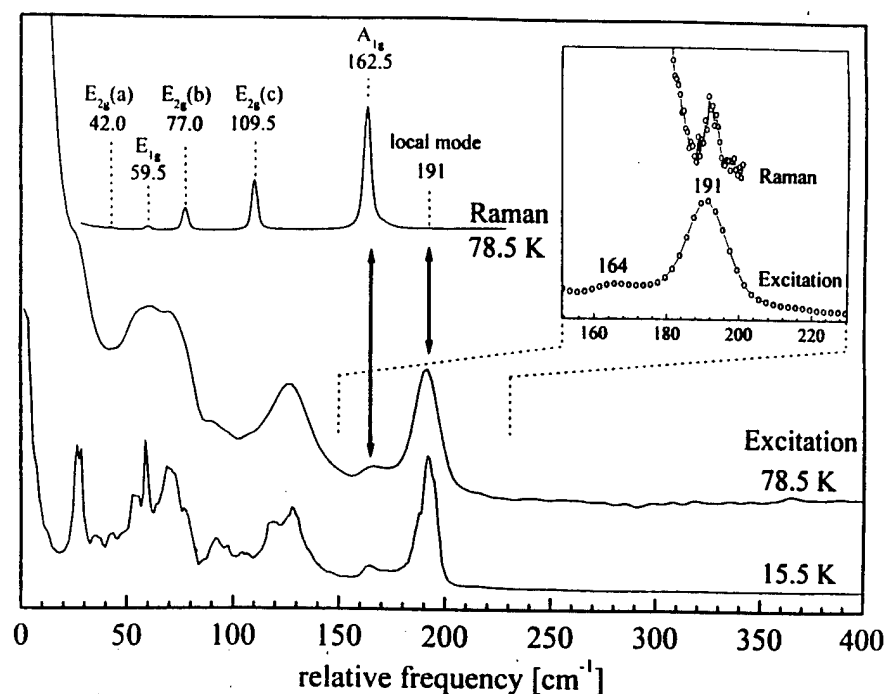

Figure 6. Raman spectrum of Yb:CsCdBr$_3$ compared with the Yb luminescence excitation spectrum at low temperatures.

Further Raman experiments in this interesting system are currently impeded by lack of availablility of an infrared Raman spectrometer. This will be essential for future work. Also, experiments to demonstrate all-optical switching in this material have been attempted, but have not succeeded due to inadequate cooling design of available cryostats. By careful comparison of techniques with respect o the original switching experiments, we have determined that samples must be cooled by direct immersion in liquid or vapor cryogens. Cryostats based on conductive cooling are inadequate for studies of this kind in which significant optical absorption causes sample heating. Consequently future work will require a dedicated infrared Raman facility and improved cryostats.

References:

1. H. Ni, "Avalanche Upconversion in Tm:LiYF$_4$, Tm:YAlO$_3$, and Tm:YAG, Ph. D. Dissertation, University of Michigan, Ann Arbor, 1994.

Appendices

The following attachments present reprints of articles and papers in which key results of this project have been presented in archival journals or at major international scientific conferences.

Invited Papers:

S.C. Rand, "Critical Coherence in Cooperative Photon-Atom Interactions", International Quantum Electronics Conference (IQEC '96), Sydney, Australia, July 14-19, 1996, paper ThM1.

S.C. Rand, "Critical Excited State Dynamics in Dense Rare Earth Systems", International Conference on the Physics of Quantum Electronics", Snowbird, Utah, January 12-15, 1997.

Contributed Papers:

A. Kuditcher, M.P. Hehlen, S.C. Rand, B. Hoover, and E. Leith, "Time-gated Harmonic Imaging through Scattering Media", Conference on Lasers & Electro-optics (CLEO'98), San Francisco, May 3-8 (1997), submitted.

Journal Articles:

M.P. Hehlen, A. Kuditcher, S.C. Rand, and M.A. Tischler, "Electron-phonon Interactions in Yb:CsCdBr$_3$", Journal of Chemical Physics, October (1997).

Q. Shu, H. Ni and S.C. Rand, "Nonlinear Dispersion of Avalanche Upconversion", Optics Letters 22,123(1997).

Q. Shu and S.C. Rand, "Critical Slowing Down and Dispersion of Avalanche Upconversion Dynamics", Physical Review B55, 8776(1997).

"Critical Coherence in Cooperative Photon-Atom Interactions"

by

Stephen C. Rand

Associate Professor

Division of Applied Physics, Randall Laboratory

University of Michigan

Ann Arbor, Michigan 48109-1120

ABSTRACT

Bistable upconversion luminescence observed in a "dense" medium
over a wide temperature range exhibits intrinsic hysteresis
governed by a critical degree of coherence in the Lorentz local field.

"Critical Coherence", S. C. Rand

Rare earth ions typically interact weakly with one another, even if they are nearest neighbors in a crystal. The inter-atomic coupling strength is generally insufficient to cause strong delocalization of optical excitation. This simply means that while many ions engage in non-radiative population dynamics as the result of coupling to other dopant ions, there is very little *spatial* coherence in their interactions. However, in every interaction between atoms and lasers, considerable *optical* coherence can be generated, and its dephasing rate can govern the population dynamics in a surprisingly critical way in dense systems.

Observations in concentrated crystals of $Cs_3Y_2Br_9$:10%Yb^{3+} have revealed intrinsically bistable upconversion emission by Yb^{3+} ions at low temperatures [1,2]. Hysteresis loops of diminishing size are observed as temperature increases, until optical bistability disappears altogether. A compilation of intensities at which switching occurs, for various temperatures, provides a diagram (due to M. Hehlen) of the boundaries for bistability in a temperature-intensity phase space. This plot, reproduced in Fig. 1, provides solid experimental evidence of a critical point for cooperative dynamics in this phase space.

The occurrence of the critical vertex, and its implications, can be understood using density matrix theory. An essential ingredient is the introduction of migration-induced dephasing. The migration process is shown to reduce the bilinear coupling of population and polarization which is essential to generate intrinsic bistability.

"Critical Coherence", S.C. Rand

Actual predictions of cooperative luminescent intensity versus incident intensity for various values of the energy migration rate constant β are shown in Fig. 2.

The curve with $\beta=10$ in Fig. 2 depicts the critical dephasing condition at which the hysteresis evident for lower β values disappears. Here, coherence required to sustain intrinsic bistability drops to a critical value. Mathematically, the luminescence intensity develops a saddle point as its two stable solutions merge and the emission curve no longer folds back on itself. At this point energy migration amongst excited atoms competes effectively for the nearest neighbour population undergoing upconversion dynamics, without altering excited state density. Increased migration reduces the time available for adjacent excited atoms to undergo cooperative upconversion. Hysteresis disappears when the migration (dephasing) rate exceeds the upconversion rate, at the point of "critical coherence" in phase space.

In dense systems of interacting atoms, we conclude that a bilinear dependence of internal dynamics on both level populations and system polarization permits optical coherence to control system evolution. This interesting connection between population dynamics and coherence in the local field opens the door to manipulation of the Lorentz field and study of critical behavior in nonlinear interactions of many kinds in dense systems.

References:

[1] M. Hehlen, H. Gudel, Q. Shu, J. Rai, S. Rai, and S.C. Rand, Phys. Rev. Lett. $\underline{73}$, 1103(1994).

[2] M. Hehlen, H. Gudel, Q. Shu and S.C. Rand, J. Chem. Phys. $\underline{104}$(4), 22 January 1996.

"Critical Coherence", S. C. Rand

Figure Captions

Figure 1. A phase diagram of experimental intensities at which switching up (unfilled squares) and switching down (filled squares) occurs in visible cooperative luminescence intensity in $Cs_3Y_2Br_9$:10% Yb^{3+} at various temperatures.

Figure 2. Calculated pair luminescence intensity (proportional to the square of the population inversion) versus incident intensity $|\Omega|^2$ on resonance, for different values of the migration rate constant β. The dashed curves indicate non-stationary solutions (unstable).

Temperature [K]
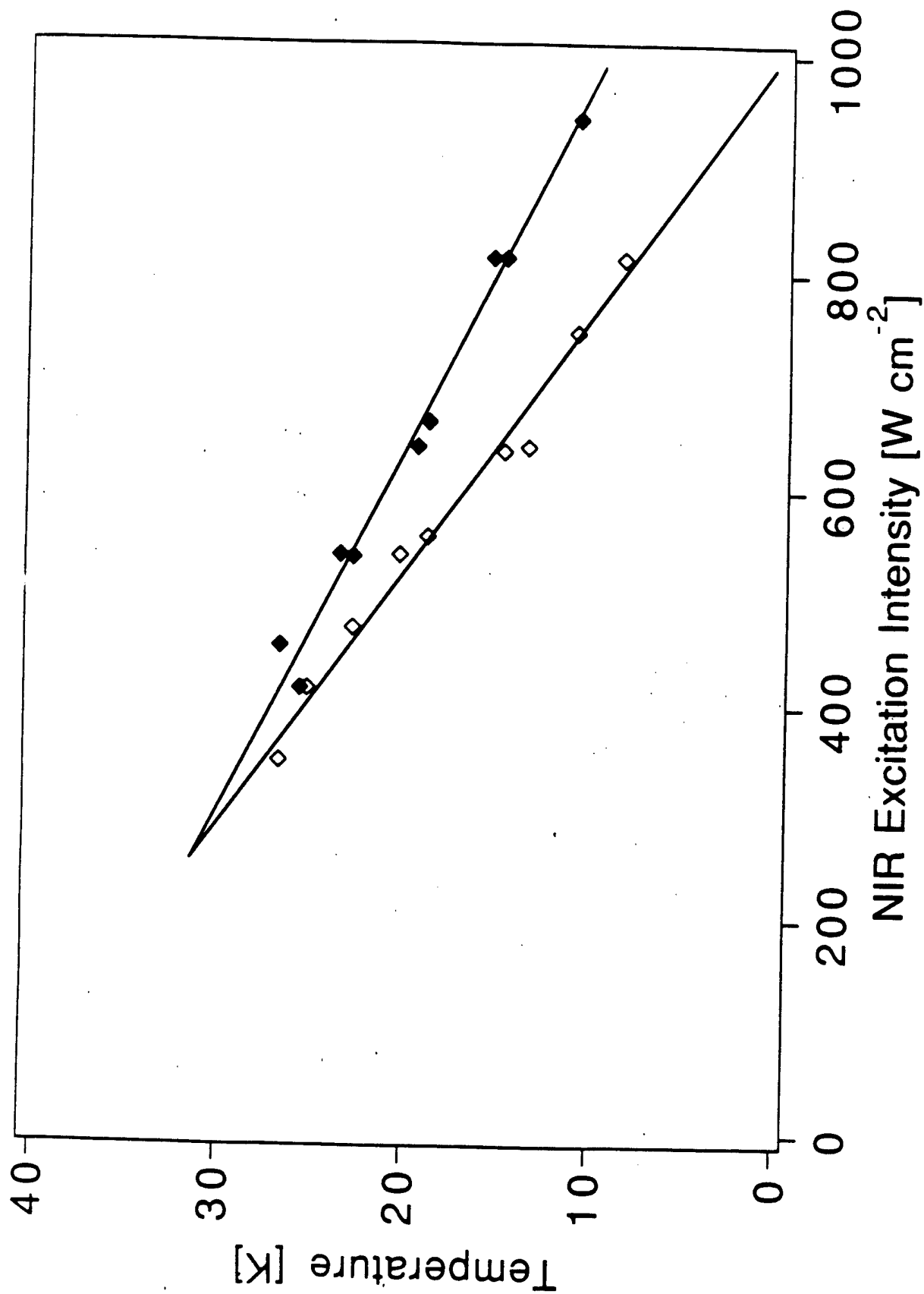
NIR Excitation Intensity [W cm^{-2}]
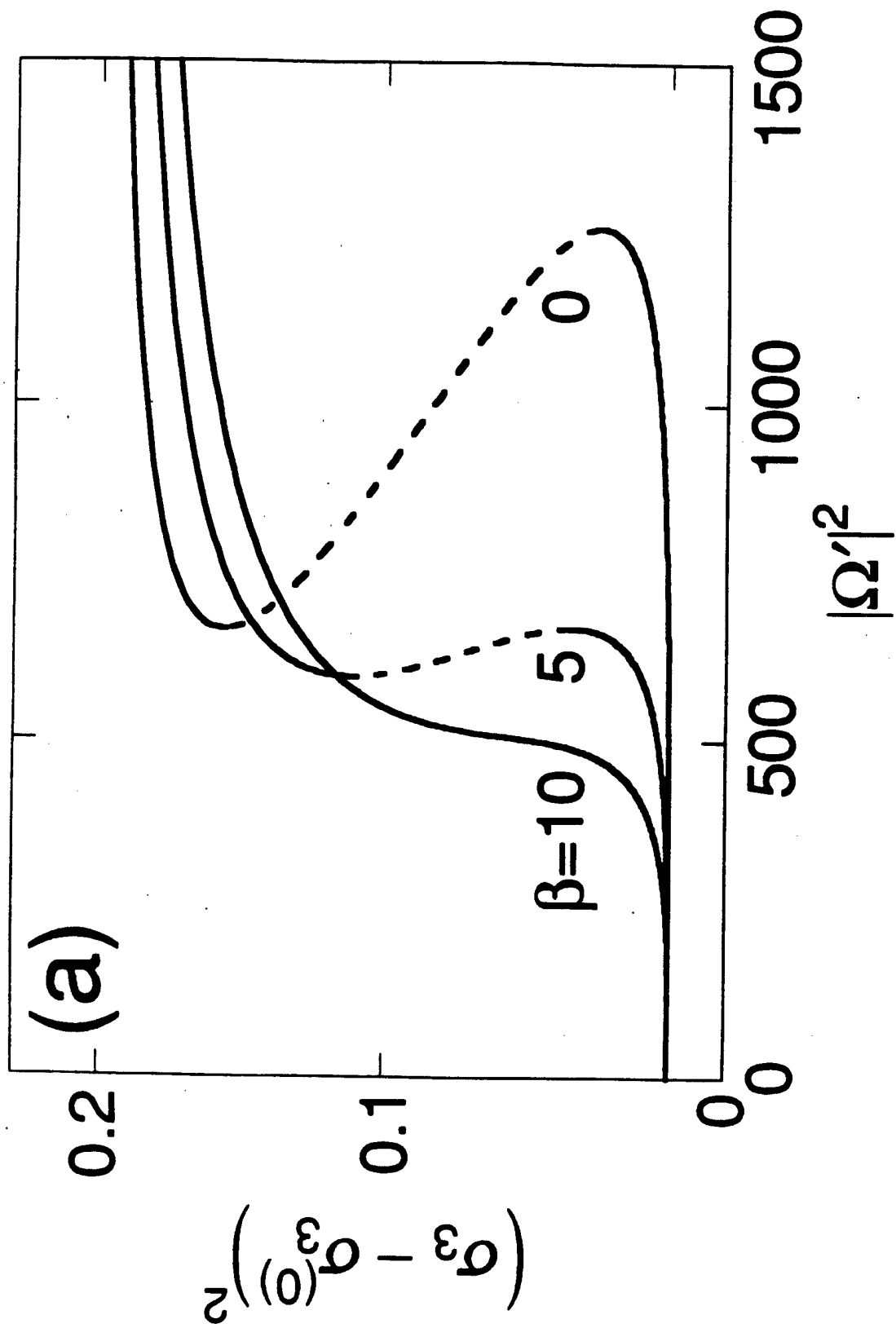
FIGURE 1.

FIGURE 2.

# Critical Excited State Dynamics in Dense Rare Earth Systems

S.C. Rand

Division of Applied Physics, Randall Laboratory
University of Michigan, Ann Arbor, MI 48109-1120
(FAX: 313-647-2718; scr@eecs.umich.edu)

Outline:

A. Introduction

- pair luminescence and avalanche dynamics
- observations of **intrinsic bistability** (pair luminescence) and **critical slowing down** (of avalanche dynamics) in dense media
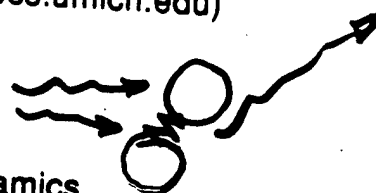
B. Intrinsic Bistability:

- mirrorless hysteresis in 10%Yb:$Cs_3Y_2Br_9$ optical pair emission
- critical phase diagram for Yb pair luminescence

C. Critical Slowing Down:

- four-wave mixing experiments in 1.5%Tm:$LiYF_4$, using optical excitation at an avalanche upconversion transition -- critical slowing down of the effective excited state lifetime
- criticality of effective decay times in Tm energy levels

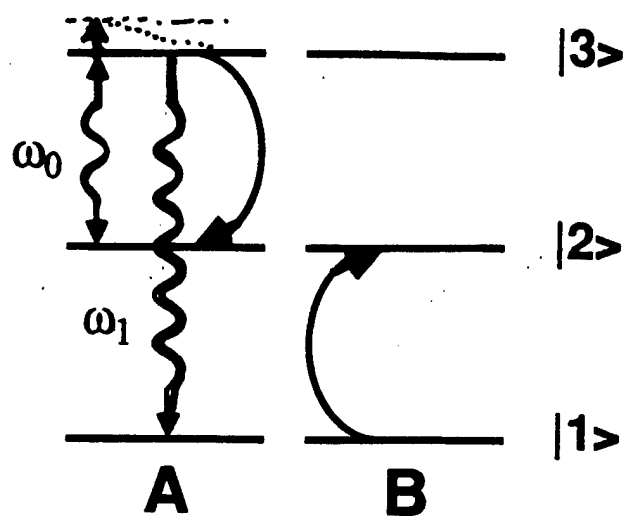D. Summary:

- possible distinctions between criticality mediated by local fields, and criticality mediated by local nonlinear dynamics.

Avalanche Dynamics

Cooperative Upconversion Dynamics

$|3\rangle$

$|2\rangle$

$|1\rangle$

ω_0

ω_1

ω_1

ω_0

A **B**

A **B**

(a)

(b)

Cryostat

Pair
Luminescence
Sample

Ti:sapphire laser

Det

Spectrometer

$|3\rangle$

$|2\rangle$

$|1\rangle$

ω_0

ω_1

A

B

ω_1

ω_0

A

B

(a)

(b)
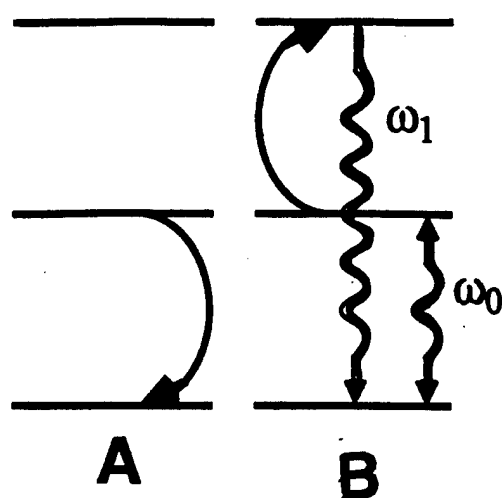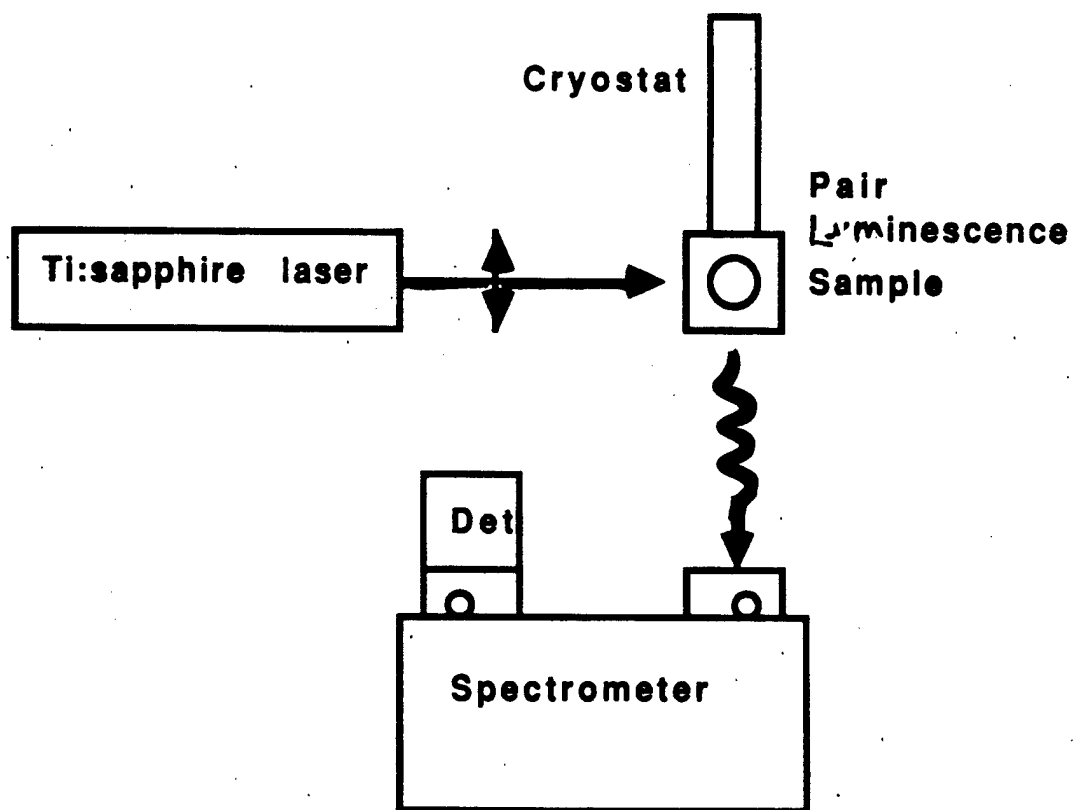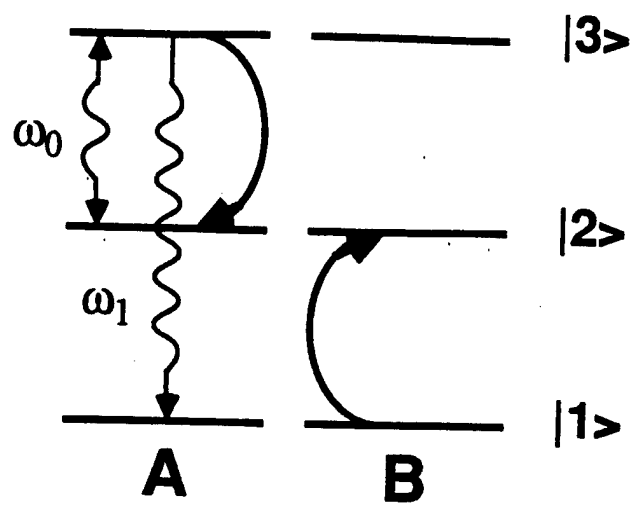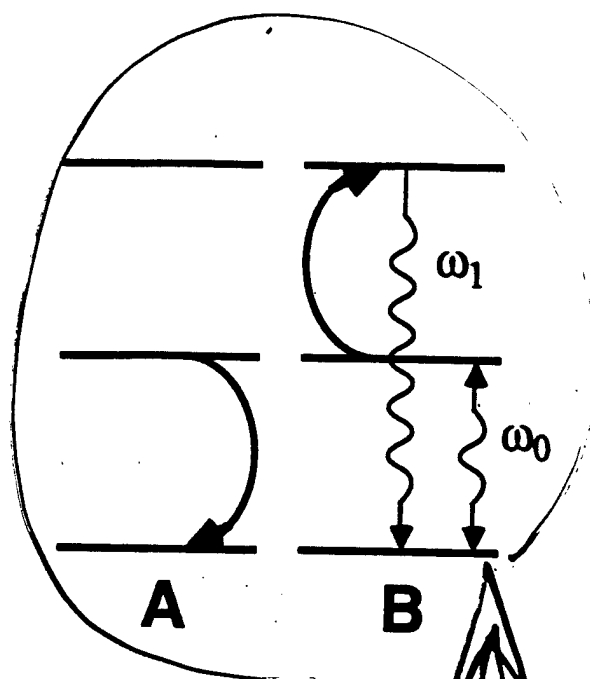
Yb   Yb
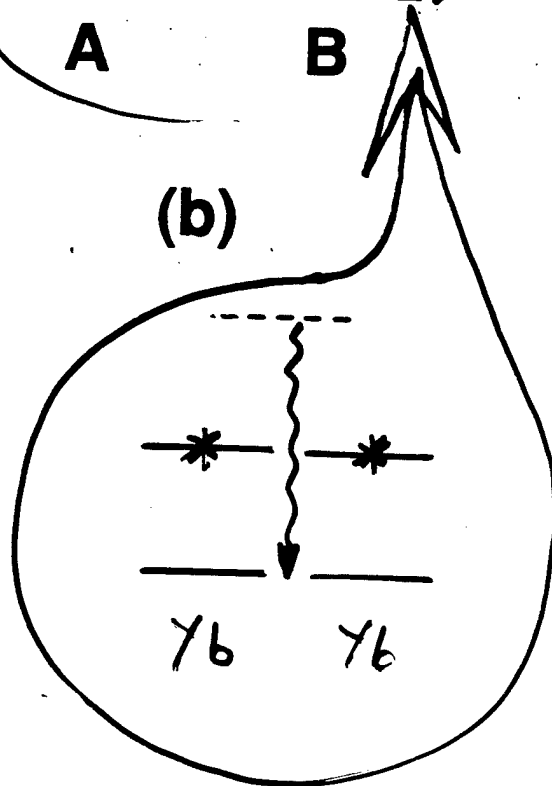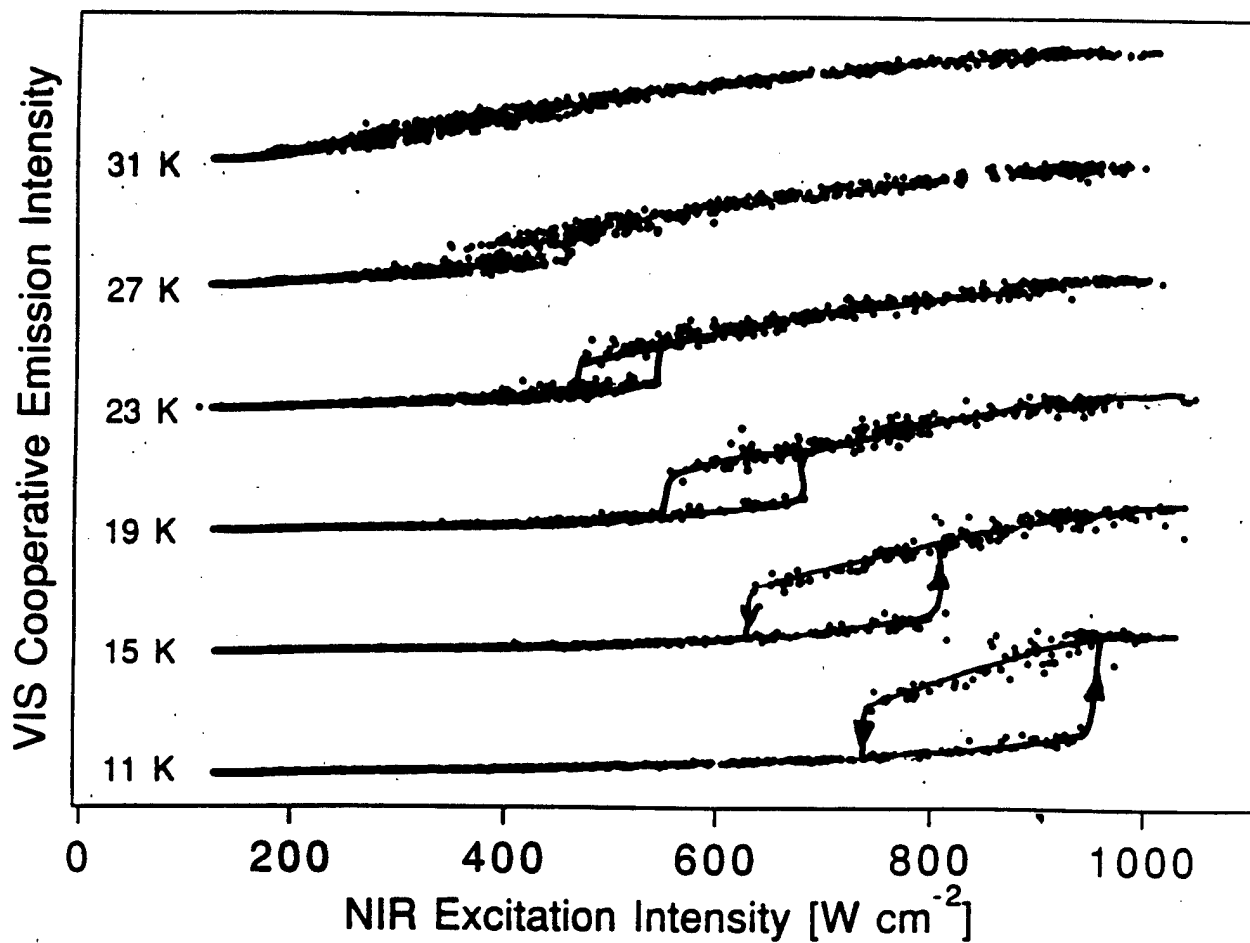
Ref: M. Hehlen et al., PRL 73, 1103 (1994)
    Earlier prediction: Bowden and Sung,
    PRA 19 2392 (1979)

Y-axis: VIS Cooperative Emission Intensity

X-axis: Temperature [K]

814 W cm^{-2}

640 W cm^{-2}

539 W cm^{-2}

415 W cm^{-2}

$^2F_{5/2}(0') \rightarrow {}^2F_{7/2}(3)$

$^2F_{5/2}(1') \rightarrow {}^2F_{7/2}(3)$

HOT

COLD

upper branch

lower branch

NIR Emission Intensity

Wave numbers [cm^{-1}]

9600   9800   10000   10200

(a) Plot of $(\sigma_3 - \sigma_3^{(0)})^2$ versus $|\Omega|^2$ for $\beta = 10$, 5, and 0.

(b) Plot of $(\sigma_3 - \sigma_3^{(0)})^2$ versus β for $|\Omega|^2 = 640$, 570, and 500.
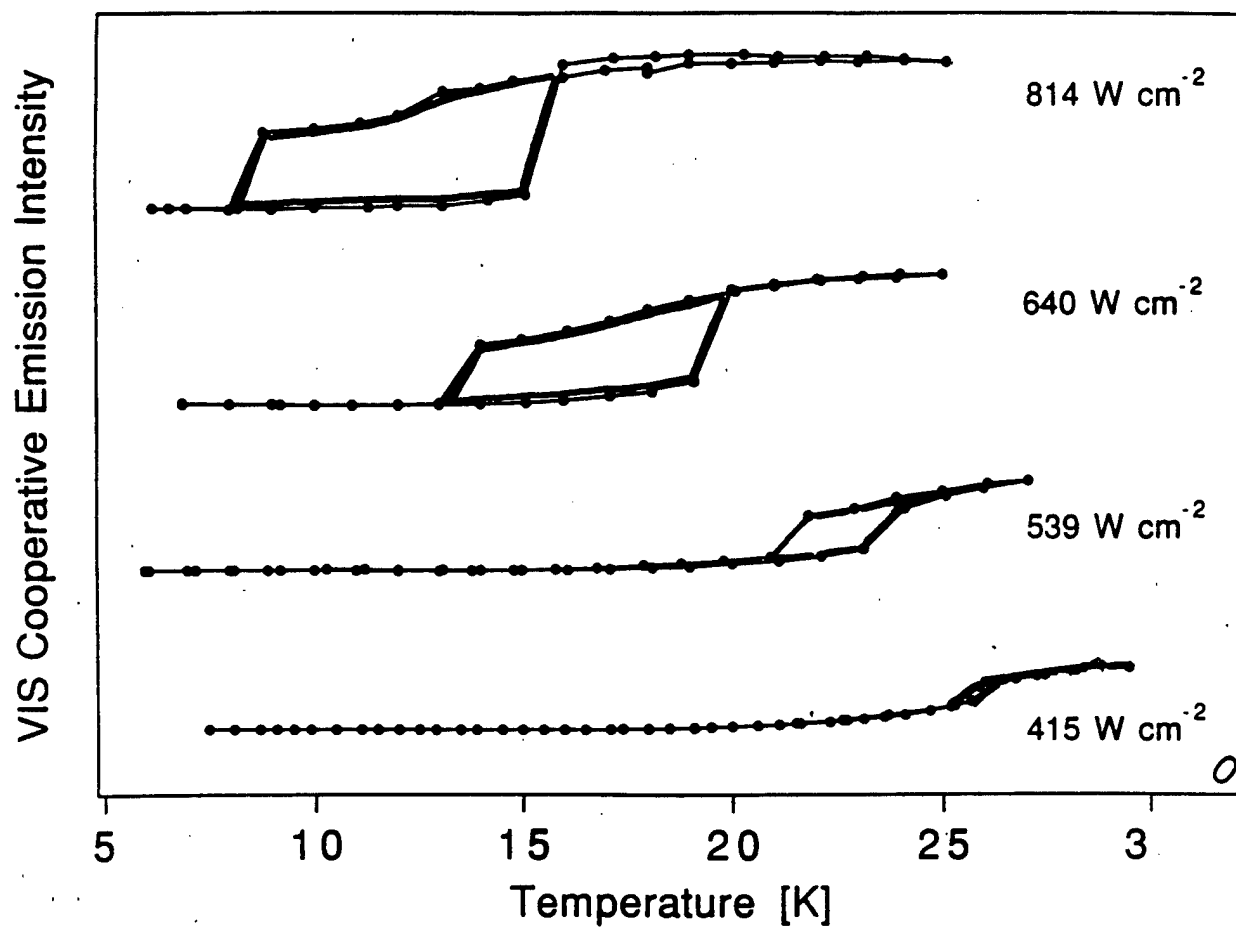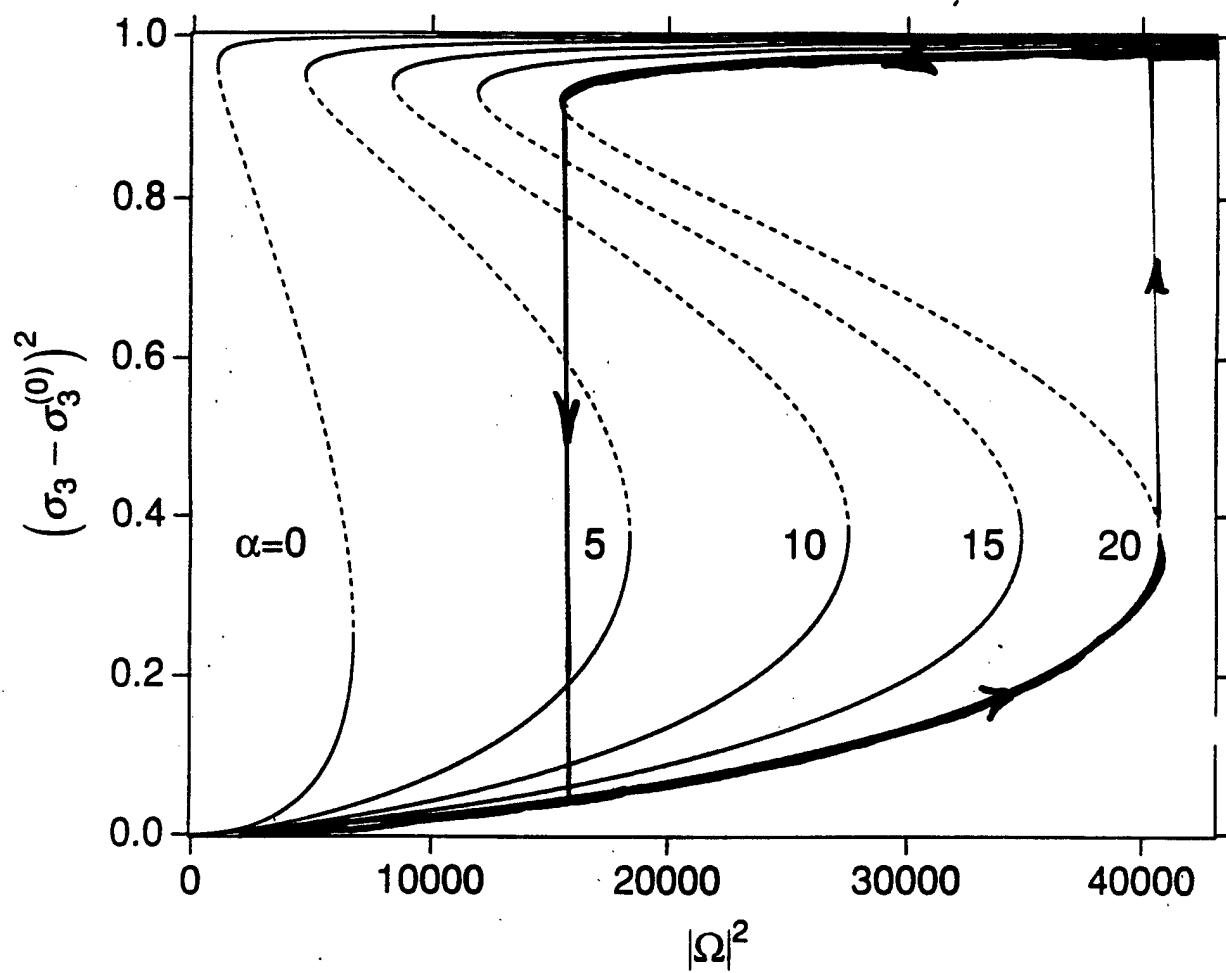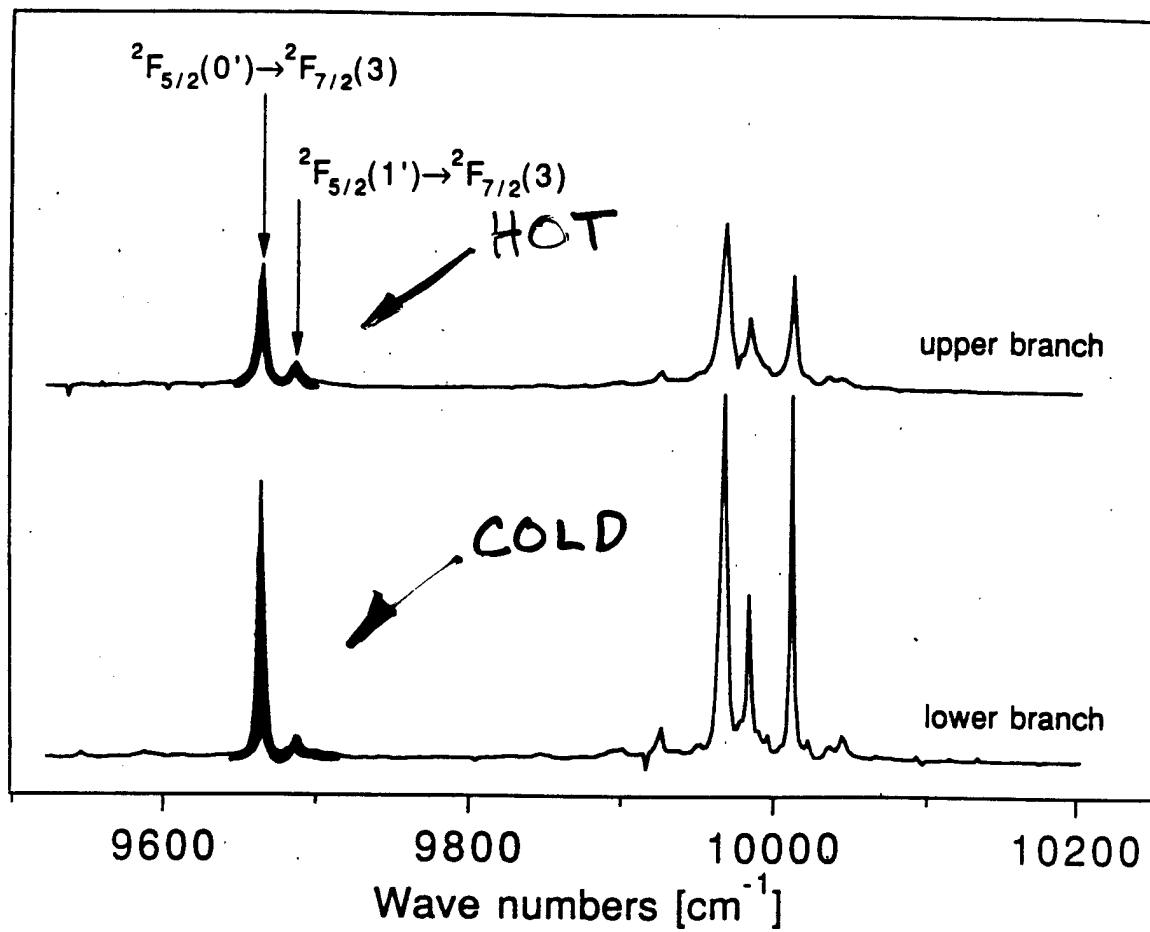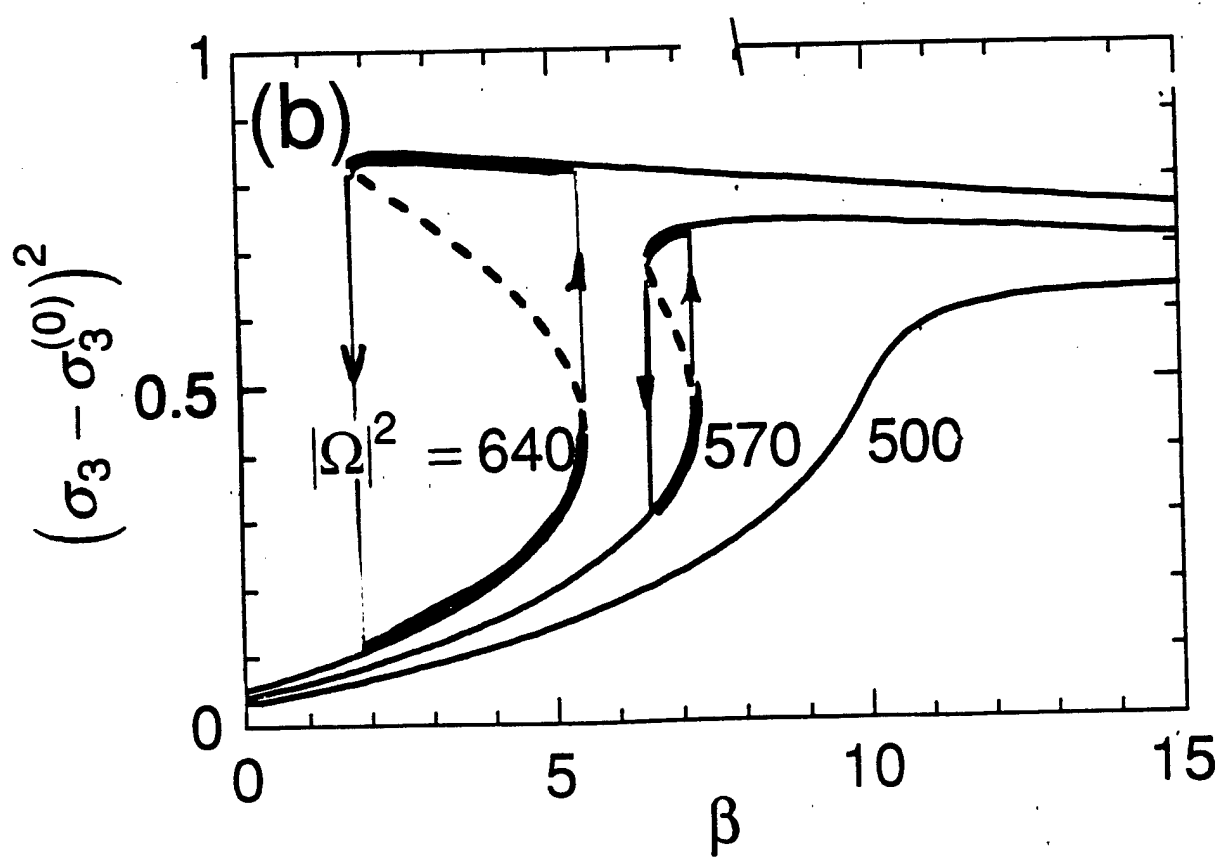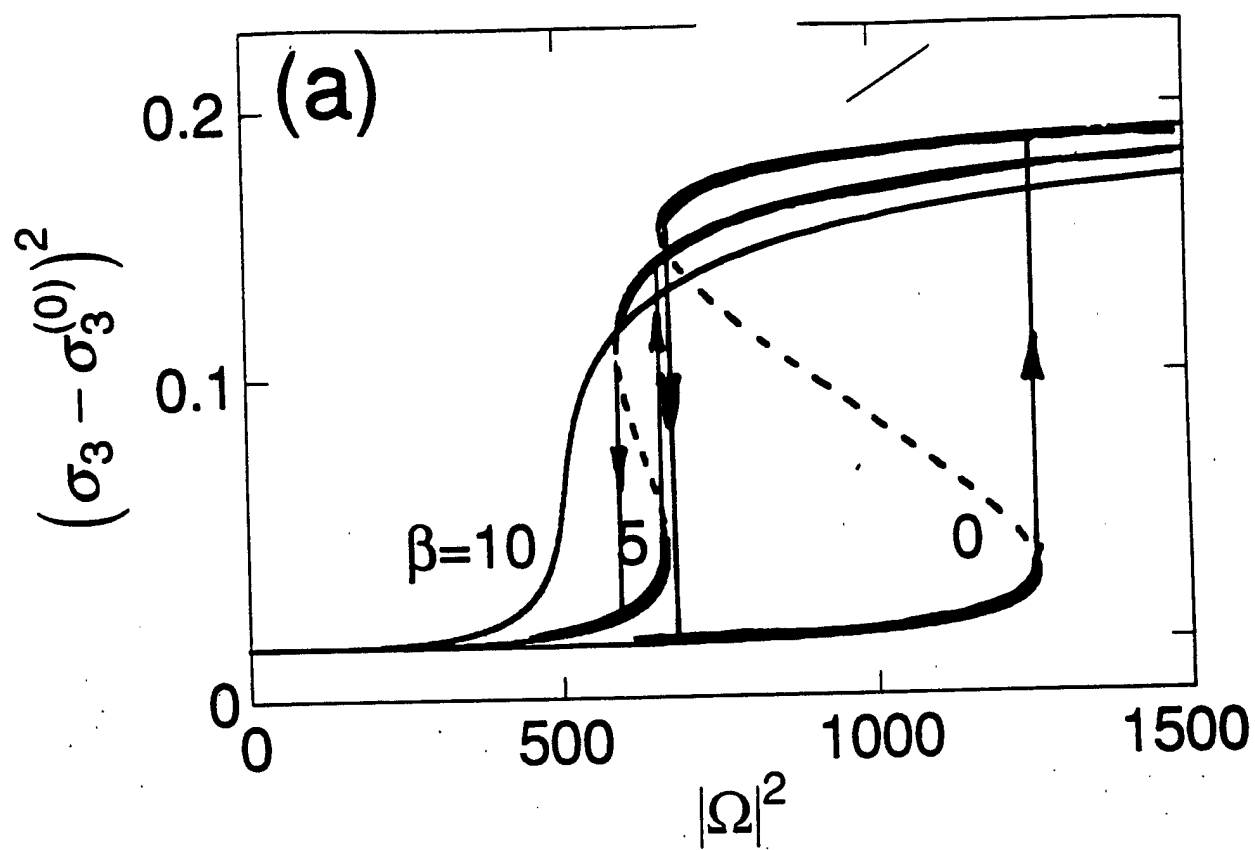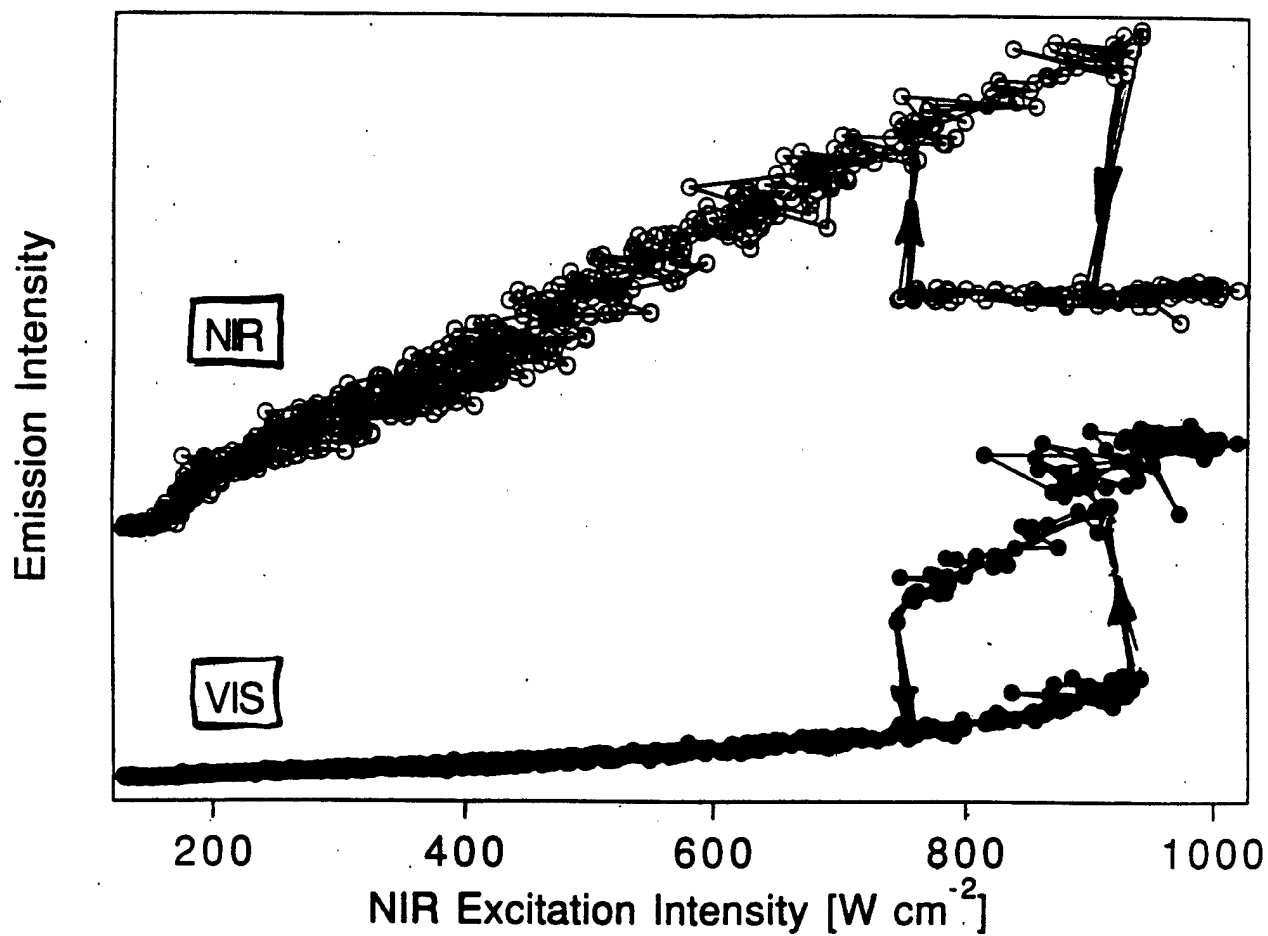
Ref: M. Hehlen et al., J. Chem. Phys. 104, 1232 (1996).
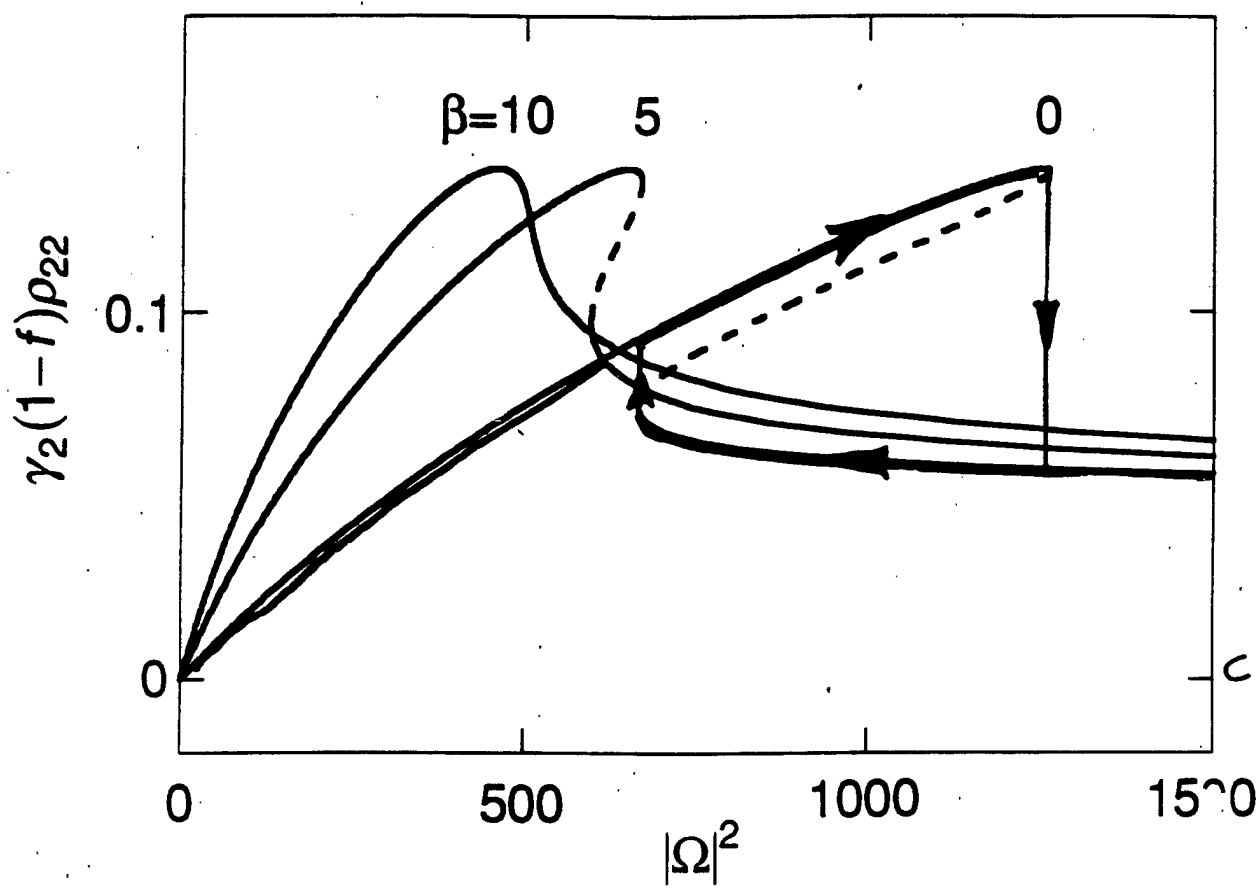
Critical Phase Diagram
for 10% Yb: Cs_3YBr_9

Critical Point

Temperature [K]

NIR Excitation Intensity [W cm^{-2}]

ω_0

ω_1

$|3\rangle$

$|2\rangle$

$|1\rangle$

A

B

(a)

ω_1

ω_0

A

B
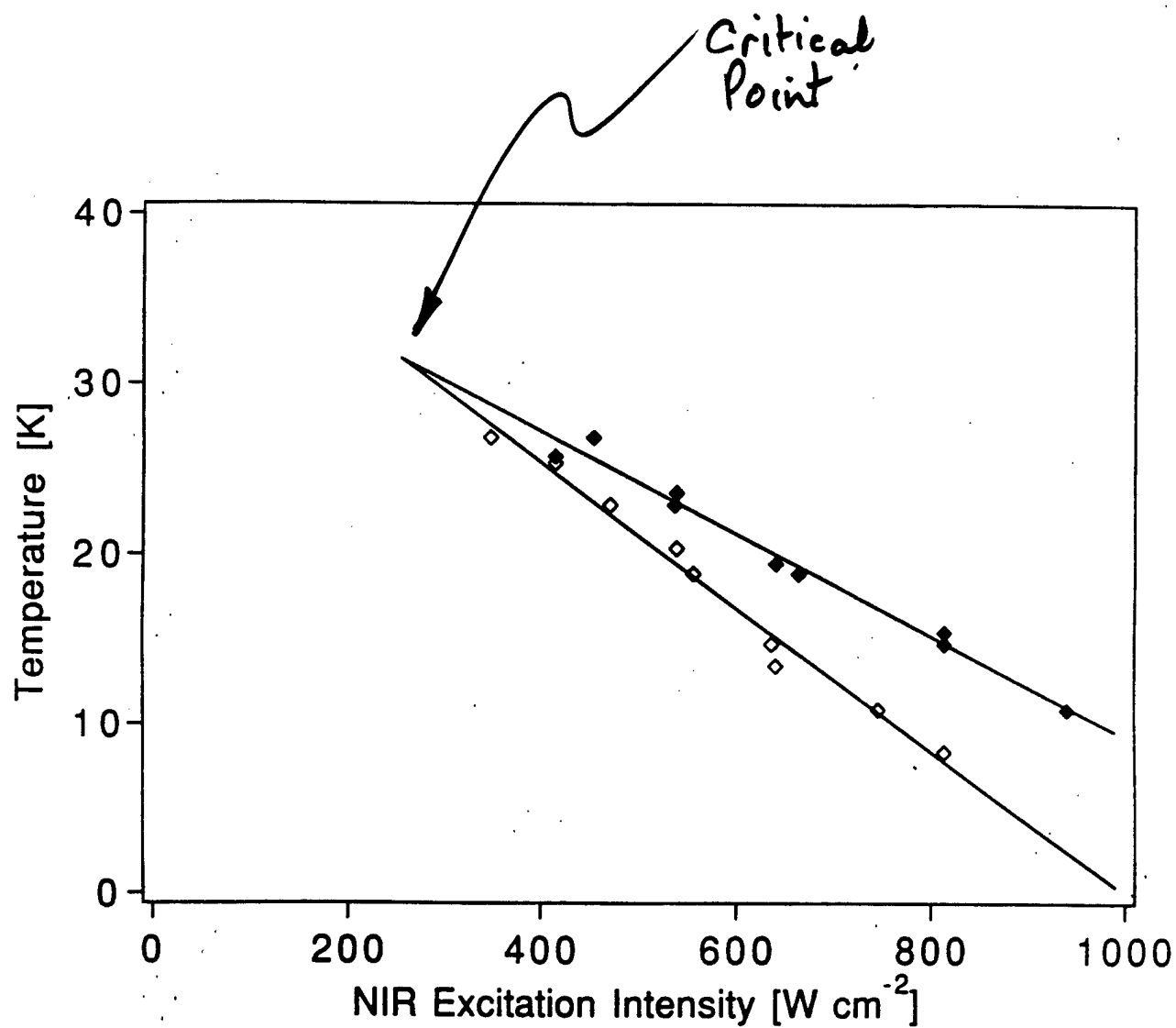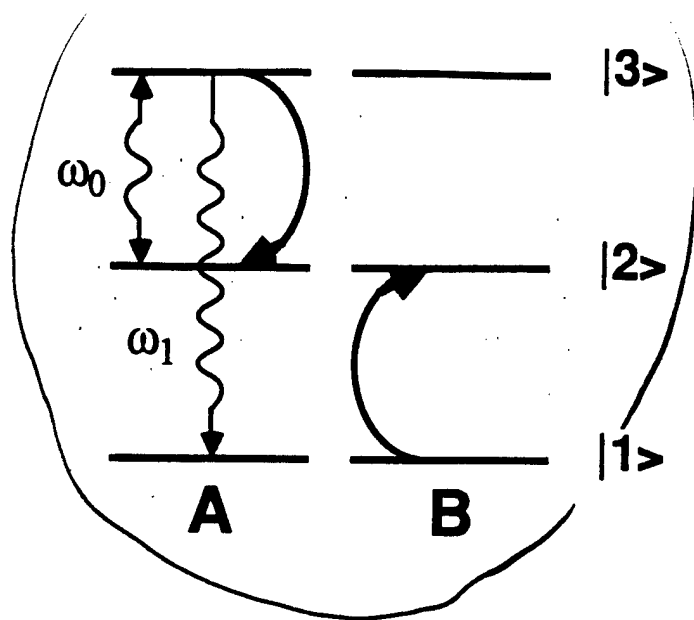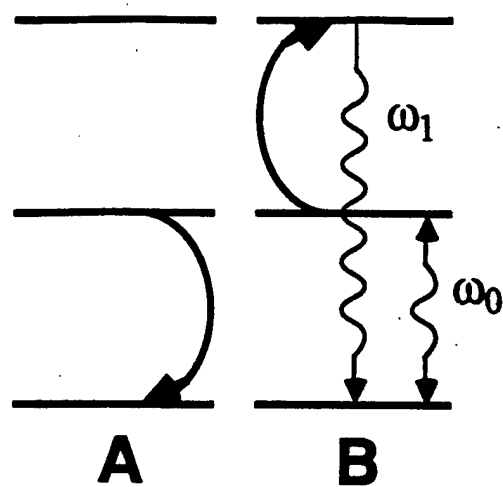
(b)

2-beam coupling measurements:
(Characterization of the nonlinear) (refractive index & check FWM)

6877.3 Å

6876.2 Å

6873.8 Å

6869.7 Å

6862.1 Å

6858.6 Å

6803.2 Å

6661.7 Å

6557.8 Å

6482.1 Å

-100   -50   0   50   100

$(\omega_{probe} - \omega_{pump})/2\pi$ (Hz)

avalanche induced dispersion

Ground State Absorption Dispersion
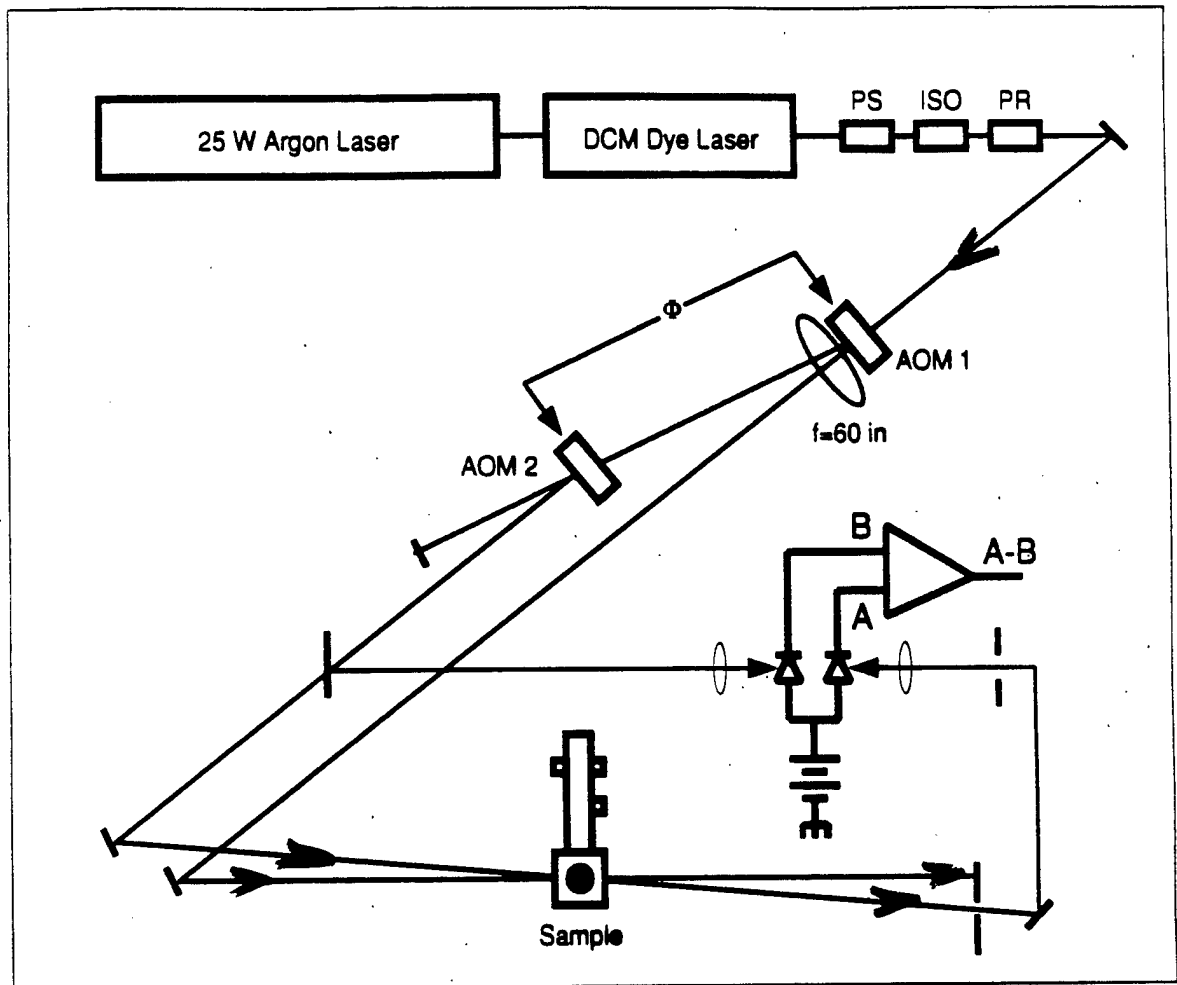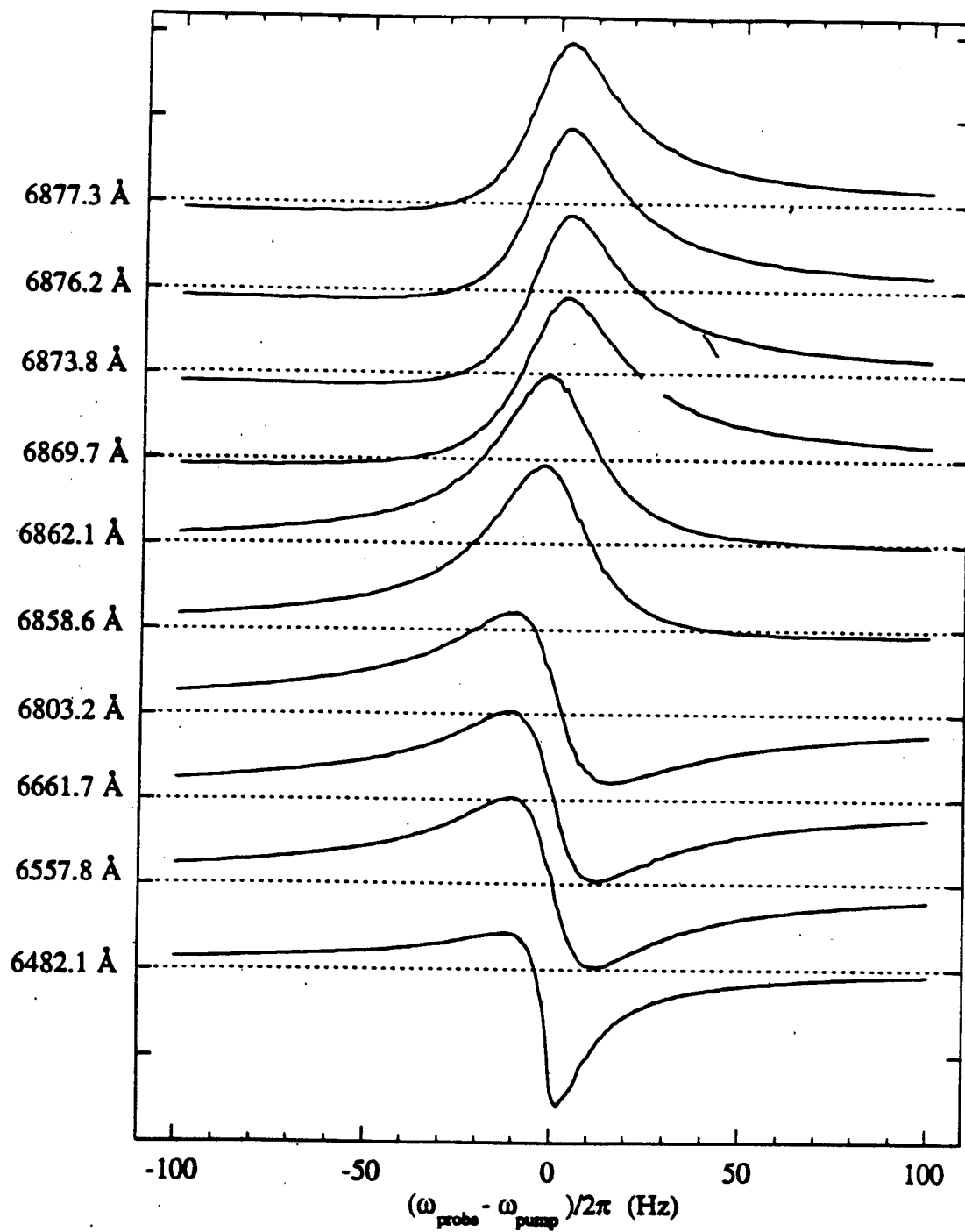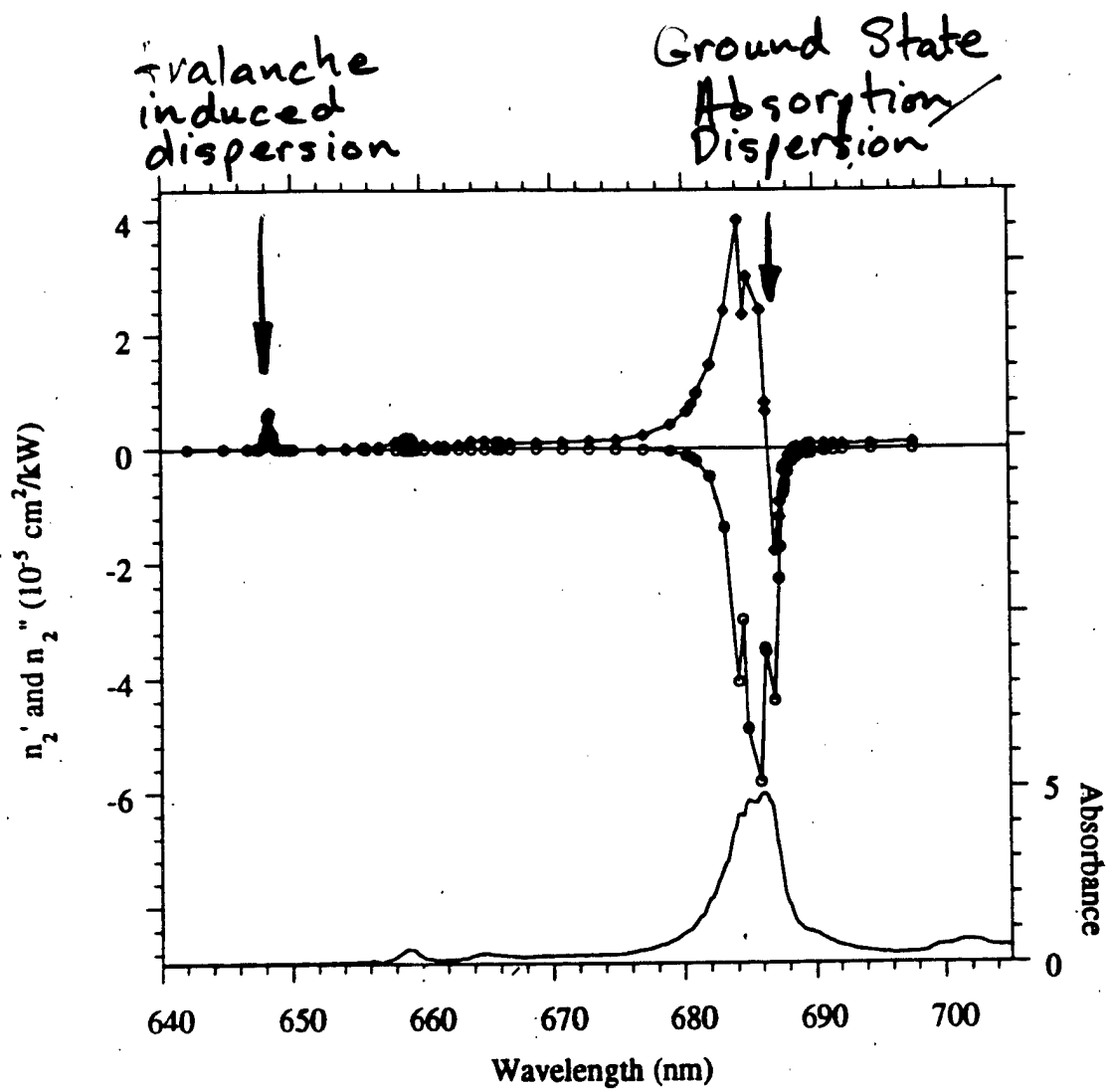
EXPERIMENT
2-Beam Coupling Results
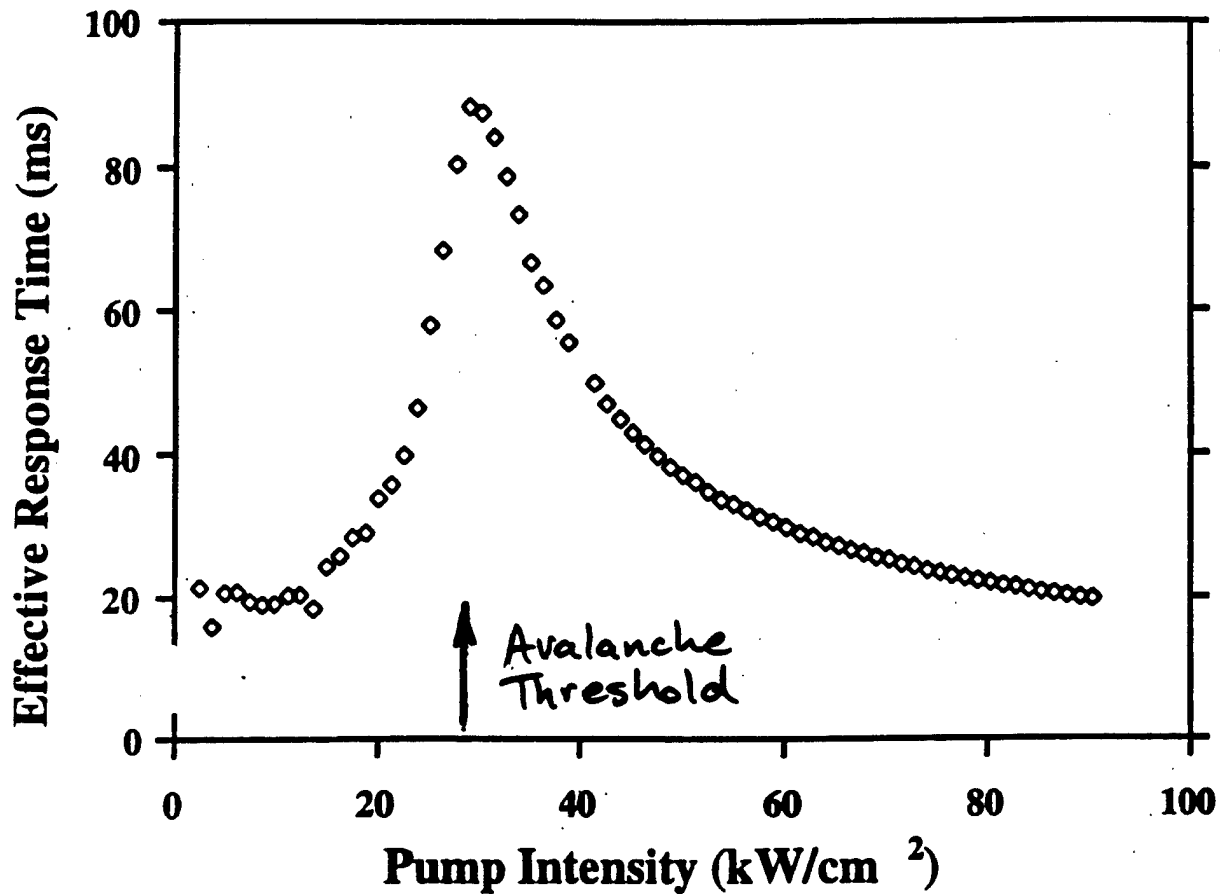
Ref: Q. Shu and S. Rand, Phys. Rev. B (to be published).

THEORY
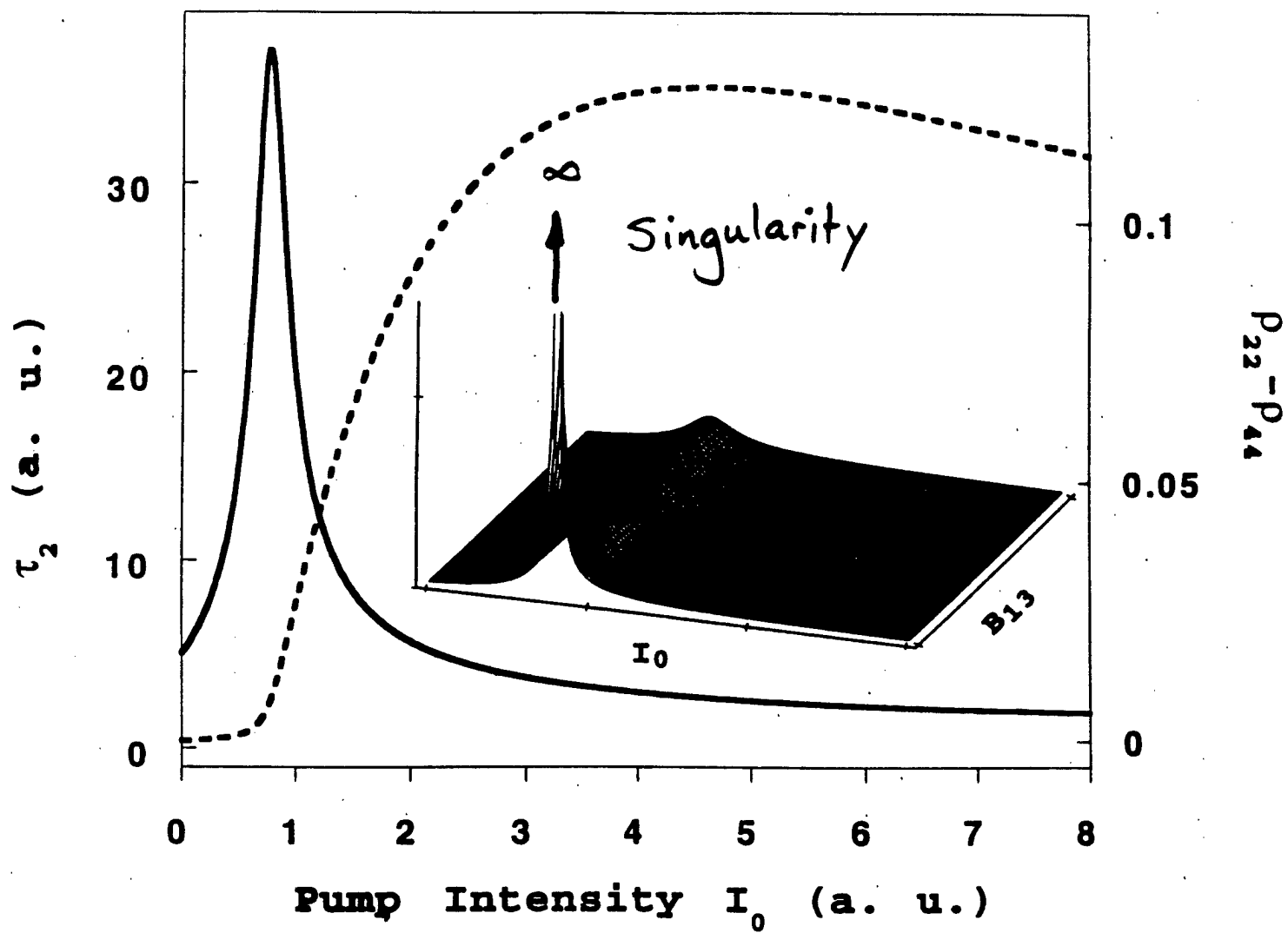
Summary

Cooperative Upconversion:
- intrinsic bistability occurs in 10%Yb:$Cs_3Y_2Br_9$ despite the weakness of Yb-Yb interactions - possible role of selectivity in excitation
- analysis indicates a balance of nonlinearity and dephasing
- unexpected role of coherence: rapid dephasing diminishes hysteresis
- critical phase diagram for Yb pair luminescence:
    -criticality of the local field correction-

Avalanche Upconversion:
- avalanche dynamics in 1.5%Tm:$LiYF_4$ -- critical slowing down of the effective Tm excited state lifetime
- no evidence so far of coherence between atoms. Data explainable with rate equations lacking extra degrees of freedom
    -criticality of the local field??- Role of other levels important?
    - do we have to drive one of the two transition dipoles involved in the cross relaxation to involve local field?

Origin of criticality:
- do these two closely related processes exhibit criticality for the same or different reasons?
- how can the experimentalist distinguish local field effect vs. bare nonlinear dynamics?
- **coherence vs. incoherence?**
    CAUSE OR EFFECT ?

Time-gated Harmonic Imaging through Scattering Media

A. Kuditcher, M. P. Hehlen, S.C. Rand, B. Hoover, and E. Leith

Dept. of Electrical Engineering

1311 Beal Avenue, University of Michigan

Ann Arbor, MI 48109-1112

Tel: 313-763-6810

Fax: 313-647-2718

E-mail:scr@eecs.umich.edu

Abstract

We demonstrate image reconstruction of an object obscured by a highly scattering medium using a simple time-gated second harmonic generation scheme.

1

Time-gated Harmonic Imaging through Scattering Media

A. Kuditcher, M. P. Hehlen, S.C. Rand, B. Hoover, and E. Leith

Dept. of Electrical Engineering

1311 Beal Avenue, University of Michigan

Ann Arbor, MI 48109-1112

Tel: 313-763-6810

Fax: 313-647-2718

A significant limitation to existing optical techniques for imaging through obscuring, highly scattering media is the contrast limitation due to non-image-bearing, scattered light at the frequency of incident beams. For example, in the holographic time-gated technique [1], such light contributes to the average background intensity, thereby decreasing contrast. In the present work we upconvert an image using time-gated, second harmonic generation of incident light from an ultrashort pulse laser to reduce the interference from non-image-bearing scattered light at the input frequency. We extend earlier results [2] by capturing an entire image without any scanning and consider implications of this technique for imaging through dynamic scatterering media.

The output of a Ti:sapphire laser emitting mode-locked pulses of about 30 fs duration was divided into two beams. One beam was magnified 5x and collimated with a Newtonian telescope to serve as the object beam. In this way, the object beam was assured of being smaller in the focal region than the reference, thereby improving spatial resolution for imaging applications while simultaneously making the beam large enough for the insertion of coarse-grain objects. A variable delay line was placed in the second beam for timing control. A 1 mm diameter wire was placed in the first beam at the object plane and two ground glass screens inserted at positions approximately 1 cm and 10 cm beyond it to obscure the object completely. The second beam was similarly collimated and aligned to be parallel to the first. Both beams were focused by a single 30 cm lens into an oriented crystal of $LiIO_3$ at an external crossing angle of approximately 4 degrees. The apparatus is shown in Fig.1.

When the crystal was rotated to the Type I phase matching angle for 800 nm, both fundamental input beams simultaneously showed efficient harmonic conversion irrespective of the reference delay. This was somewhat unexpected because the inter-arm angle exceeded the calculated angular acceptance at 800 nm for monochromatic beams, but did not interfere with signal detection since the spatial separation was more than adequate to isolate any desired beam. When the delay line was adjusted for zero inter-arm delay, an additional, cross-correlated signal beam emerged along the bisector of the other two. The

2

intensity of this signal depended critically on delay and bore upconverted, time-gated image information as the result of the intensity-intensity correlation process in the nonlinear crystal. An imaging system was used to relay images formed on a phosphorescent screen to a CCD camera for data acquisition.

The cross-correlation of the scattered object wave and the reference beam with both diffusers in place is given in Fig. 2(a). Its full width at half maximum was 53 fs. The cross correlation without the diffusers shown in Fig. 2(b) was only slightly wider (57 fs), suggesting that pulse stretching attributable to the scatterers is small. However, the wavevectors of severely delayed light lie outside the acceptance cone for cross correlation in our method, and fail to contribute to this signal. With the scatterers in place, the object could not be imaged from light in the object beam in any plane at the fundamental frequency. The time-gated harmonic signal however yielded the results shown in Fig. 3 *without any electronic image processing*. The results clearly show a coarse-grain image of the wire located behind two widely separated ground glass plates.

A simple phosphorescent screen fabricated by spraying a thin layer of red fluorescent paint on a glass slide sufficed as a transmissive screen which converted the image at 400 nm to the red spectral region. This resulted in a good match to the response curve of the CCD camera while retaining the signal-to-noise advantage of working at a wavelength different from that of the fundamental beams. Image field data were recorded at upconverted wavelengths for various delays. Highest fidelity was attained at the shortest delays. Rapid degradation of image quality occurred as the gate delay was increased from 0 to 50 fs.

In summary we have demonstrated that time-gated upconversion can be used in a non-scanning geometry for background-free imaging of stationary objects with millimeter resolution. Our results were obtained using a crossed beam configuration, but collinear (inline) geometries are feasible in Type II geometries. No image processing was necessary to obtain the results presented here. Images were obvious to the naked eye at short gate delays. This scheme is expected to be well-adapted to imaging problems involving moving scattering media because the nonlinear process utilized to reconstruct the image is an intensity correlation which should be insensitive to phase variations of scattered fields.

References:

1. H. Chen, Y. Chen, D. Dilworth, E. Leith, J. Lopez, and J. Valdmanis, Opt. Lett. 16, 487(1991).

2. K. M. Yoo, Q. Xing, and R. R. Alfano, Opt. Lett. 16, 1019(1991).

"Time-gated Harmonic Imaging...", by Kuditcher et al.

Figure Captions:

Figure 1. Apparatus for imaging through highly scattering media using time-gated, second harmonic generation. Double-headed arrows indicate lenses.

Figure 2. Cross-correlation of the object wave and the reference beam (a) without any diffusers in place to show the pulsewidth prior to "stretching", and (b) with two diffusers in place to obscure the object.

Figure 3. Upconverted image of the object plane (a) without the object present, and (b) with a 1 mm diameter wire in the object plane, obscured by two frosted glass screens and recorded in transmission with a CCD camera from a secondary image on a semi-transparent red phosphorescent screen sensitive to 400 nm.

Figure 1.

Fig. [illegible handwritten text]

FIG. 2. Autocorrelation

(b)

(a)
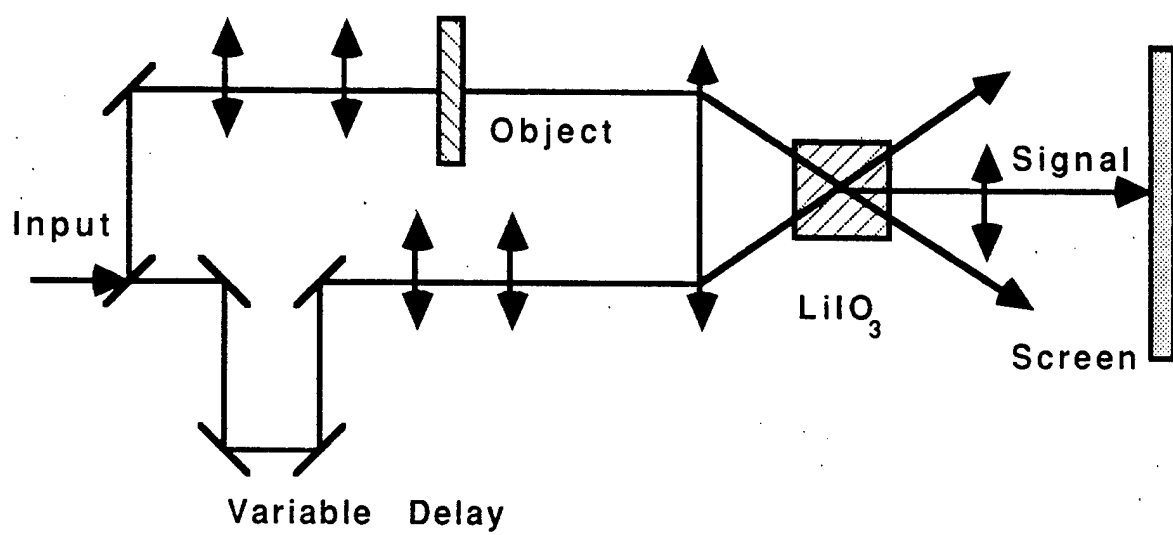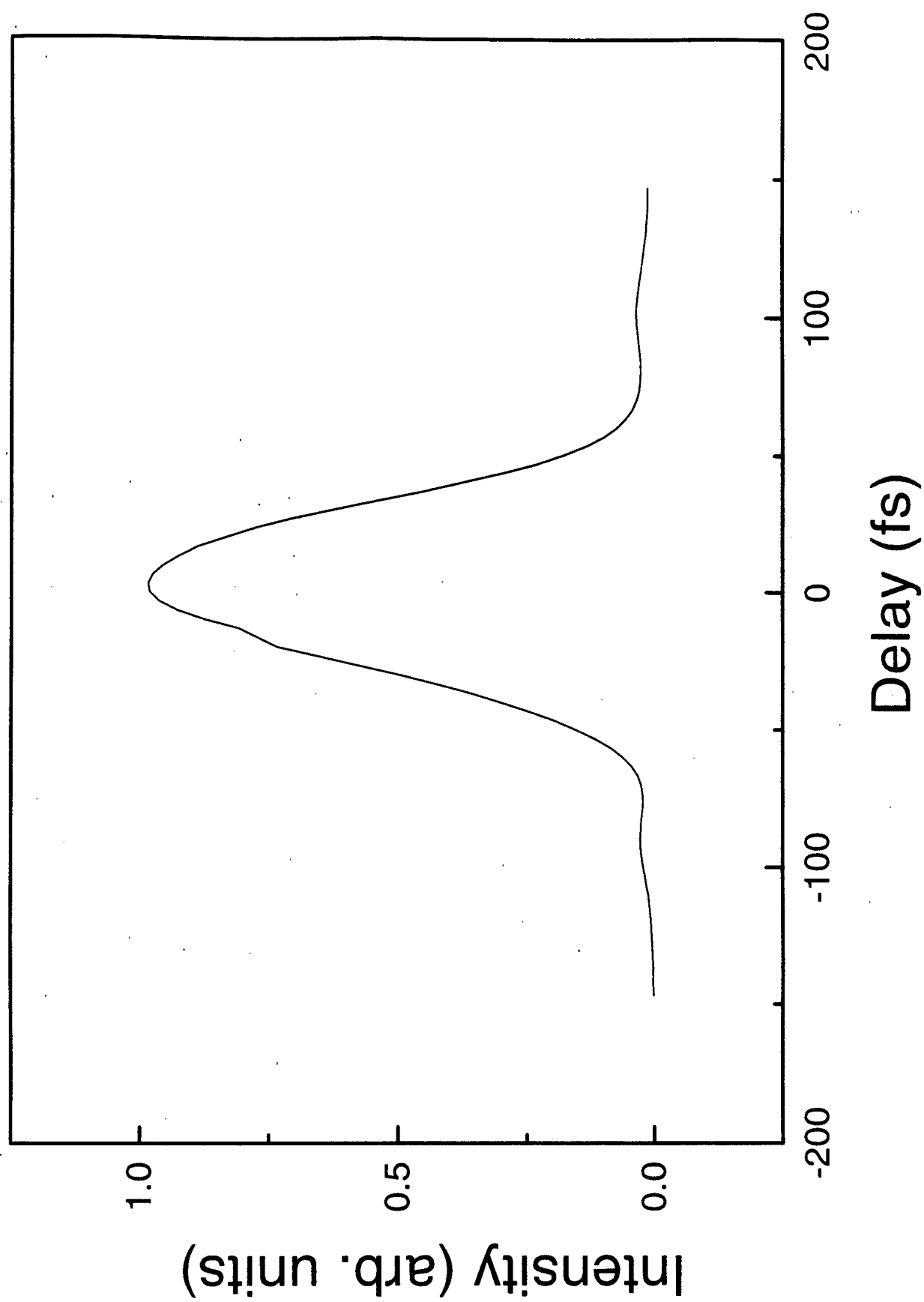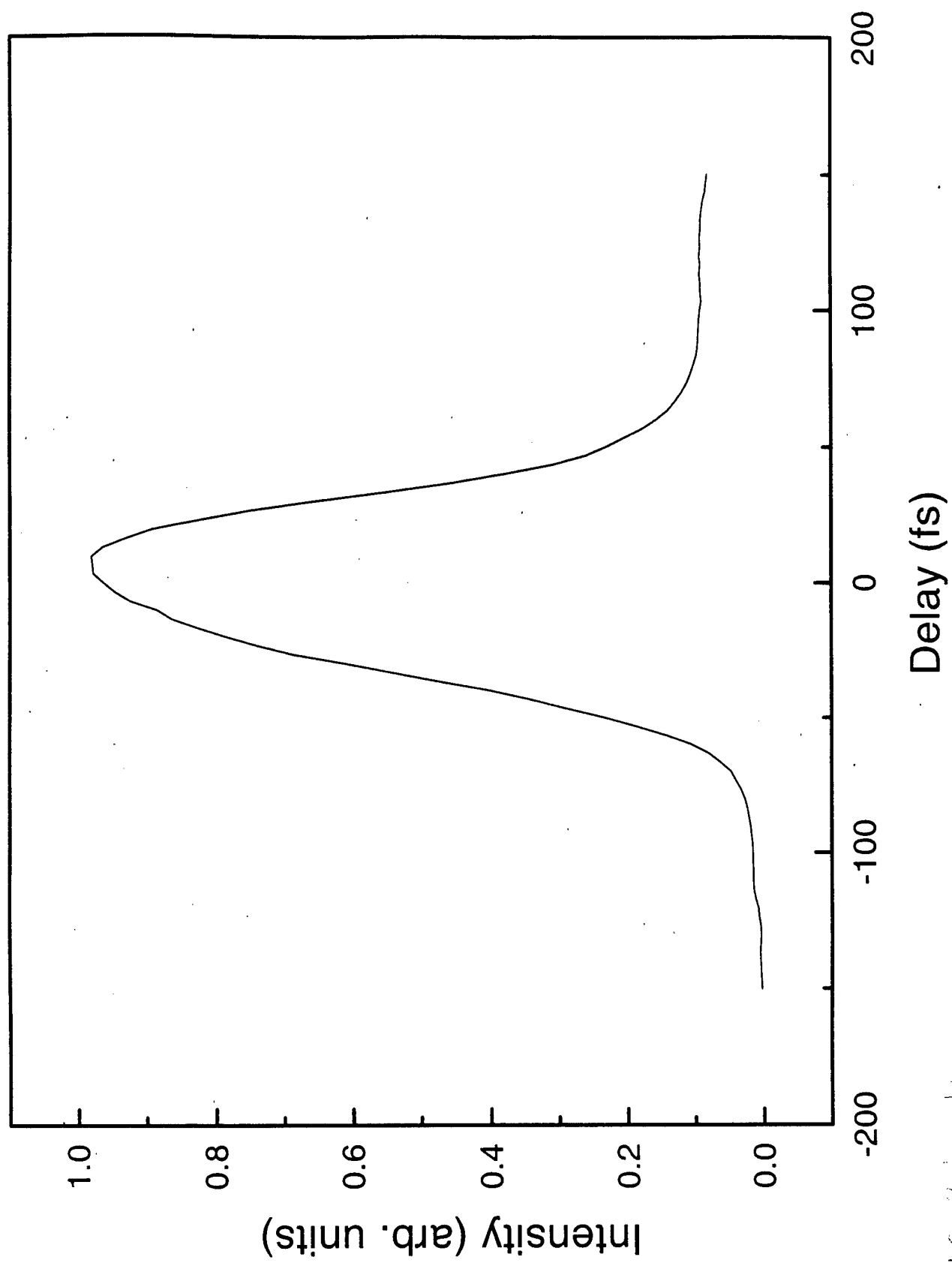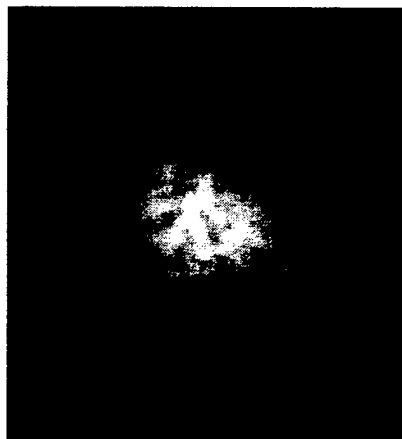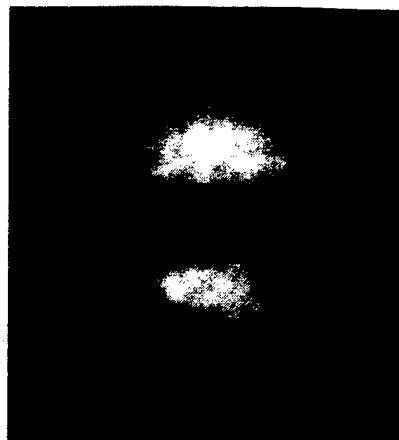
FIG. 3. Kuditcha, et al

Electron-phonon interactions in CsCdBr$_3$:Yb^{3+}

Markus P. Hehlen, Amos Kuditcher, Stephen C. Rand

Optical Sciences, The University of Michigan,

1301 Beal St., Ann Arbor, MI 48109-2122

and

Michael A. Tischler

The Harrison M. Randall Laboratory of Physics, The University of Michigan,

Ann Arbor, MI 48109-1120.

1

ABSTRACT

Pronounced electron-phonon coupling is observed for the $^2F_{7/2} \leftrightarrow\, ^2F_{5/2}$ $4f$ transitions of Yb^{3+} doped into $CsCdBr_3$. A comparison of the Raman spectrum and the luminescence excitation sideband accompanying the $^2F_{7/2}(0) \rightarrow\, ^2F_{5/2}(2')$ crystal-field transition reveals vibrational properties of the $[YbBr_6]$ coordination unit that differ markedly from those of the $CsCdBr_3$ host. In particular, the vibronic transition associated with the totally symmetric $[YbBr_6]$ stretching mode appears as a very weak feature at 191 cm^{-1} in the Raman spectrum, whereas the totally symmetric $[CdBr_6]$ stretching mode of the $CsCdBr_3$ bulk, which appears as a strong feature at 162.5 cm^{-1} in the Raman spectrum, is only weakly discernible in the sideband. This is direct evidence for a large contribution from $\{YbBr_6\}$ local modes and a small contribution from bulk modes to the vibronic intensity. The intensity of the local mode is enhanced by approximately a factor of two in Raman spectrum when the laser is tuned into resonance with the $^2F_{7/2}(0) \rightarrow\, ^2F_{5/2}(2')$ absorption of Yb^{3+}, providing direct confirmation of its assignment. The observation of the first and second members of a Franck-Condon progression for both the local and the bulk indicates that a Δ process, rather than a M process, induces the vibronic intensity. Huang-Rhys factors of $S_{local}=0.010\pm0.002$ and $S_{bulk}=0.15\pm0.03$ were determined from the data, and reflect quite different electron-phonon coupling strengths. These results suggest that multiphonon relaxation of excited electronic states proceeds by the excitation of local modes of $[YbBr_6]$ followed by energy transfer to bulk modes of the lattice, possibly through a nonlinear coupling mechanism which is discussed briefly.

I. INTRODUCTION

The optical spectra of non-centrosymmetric solids doped with trivalent rare-earth (RE^{3+}) ions typically are dominated by electric-dipole induced electronic transitions between the states of the $4f$ shell. These electronic transitions can be accompanied by vibronic sidebands which are a result of interactions of the $4f$ electronic system with the various vibrational modes of the surroundings of the RE^{3+} ion. With the exception of Pm^{3+}, vibronic sidebands have been observed for all the RE^{3+} ions in a variety of solids [1-4]. The integrated intensity of the vibronic sideband relative to its zero-phonon line is usually low, although vibronic transition probabilities approaching or even exceeding zero-phonon transition probabilities have been found for certain transitions in some compounds [5-8]. Recently, Gd^{3+} and Pr^{3+}-doped crystals received particular attention for, besides having advantageous energy levels, they represent the extrema of the unexplained minimum of the electron-phonon-coupling strength in the middle of the lanthanide series [9].

Vibronic sidebands, although usually weak and often ignored, are just one of the many manifestations of electron-phonon coupling in rare-earth-ion doped solids. Multiphonon relaxation of excited states and phonon-assistance in non-resonant energy transfer are other ubiquitous phenomena of key importance to excited-state dynamics and, ultimately, to the role rare-earth ions play in their many applications. Knowledge of the electron-phonon coupling strength as well as the spatial extension of the electron-phonon interaction is therefore a prerequisite to a detailed understanding of the energy flow in electronic dynamics involving the vibrational system. Direct information on the spatial extension of electron-phonon interactions in particular is difficult to obtain, since in most luminescent materials such as RE^{3+}-doped YAG, $YLiF_4$, $LaCl_3$, or $Cs_3Lu_2Br_9$, in which the RE^{3+} ion substitutes for a chemically similar ion, the vibrational properties of the nearest surroundings of the RE^{3+} ion are almost identical to those of the host lattice. One exception is the class of compounds containing well-defined molecular species. The ternary chloride $(NH_4)_2GdCl_5$ for example contains NH_4^+ molecular units in the second

3

coordination sphere of Gd^{3+}, and electron-phonon coupling beyond the first $[GdCl_6]$ coordination sphere to NH_4^+ vibrational modes was observed in the $^6P_{7/2} \rightarrow {}^8S$ luminescence sideband [10]. In $(NH_4)_3YCl_6:Eu^{3+}$, electron-phonon coupling to those high frequency NH_4^+ vibrational modes in the second coordination sphere was suggested to account for the unusually low Eu^{3+} luminescence quantum yield of this material [10]. Rare-earth-ion doped compounds such as CaF_2, CdF_2, $CsMgCl_3$, or $CsCdBr_3$, in which RE^{3+} ions substitute for divalent metal ions, constitute another class of materials for which electron-phonon coupling beyond the first coordination sphere may be directly observed. Various defect structures are formed in these materials as a result of charge compensation. These defects typically have different symmetry properties which, in addition to the different mass and charge of the RE^{3+} ion, may significantly alter the vibrational properties compared to the respective host lattice site. In this context, the vibrational system may be regarded as being composed of the local vibrational modes of the RE^{3+} defect embedded in the bulk modes of the host lattice.

In this paper we present a detailed study of vibronic coupling in Yb^{3+}-doped $CsCdBr_3$. The comparison of the Raman spectrum with the luminescence excitation spectrum of the sideband accompanying the $^2F_{7/2}(0) \rightarrow {}^2F_{5/2}(2')$ crystal-field transition of Yb^{3+} reveals strong coupling to the vibrational modes of the first Yb^{3+} coordination sphere and weak contributions from coupling to modes of the second coordination sphere and beyond. In particular, resonant Raman spectra are used to assign a weak feature in the Raman spectrum to the local mode associated with the highest-energy vibration of the first Yb^{3+} coordination sphere. The appearance of two-phonon replica of both the local and the bulk mode as well as of the respective combination mode in the vibronic sideband is direct evidence for a Franck-Condon-type process inducing the vibronic intensity. The results provide insight into the spatial extension of vibronic interactions and to the various steps required for the nonradiative relaxation of electronic excited states of rare-earth ions in solids.

4

II. EXPERIMENT

Optical quality crystals of Yb^{3+}-doped $CsCdBr_3$ were grown using the Bridgman technique from 99.5% cationic purity (c.p.) CsBr (dried in vacuum at 250 °C) and $CdBr_2$ (obtained from 99.998% c.p. CdO and HBr, and sublimed at 440 °C), and $YbBr_3$. The anhydrous $YbBr_3$ was obtained in a four-step process by formation of $(NH_4)_3YbBr_6$ from evaporating a 47% HBr solution of Yb_2O_3 (99.999% c.p.) and NH_4Br (99.8% c.p.), then drying of $(NH_4)_3YbBr_6$ in a nitrogen stream at 200 °C, decomposition of $(NH_4)_3YbBr_6$ to NH_4Br and $YbBr_3$ at 420 °C in vacuum [11], and final sublimation of $YbBr_3$ at 1040 °C in a boron-nitride ampoule. The $CsCdBr_3:Yb^{3+}$ sample was obtained from cutting a crystal along planes containing the crystallographic c axis and applying an optical polish to the surfaces. The total ytterbium concentration of the sample used for this study was 1.47±0.04 mol% as determined by inductively coupled plasma optical emission spectroscopy (ICP-OES). Since Yb^{3+} is easily reduced to Yb^{2+} and moreover, Yb substitutes for Cd^{2+} when doped into $CsCdBr_3$, typically both Yb^{3+} and Yb^{2+} will be present in a Yb-doped $CsCdBr_3$ crystal grown by the method described above. The yellow color of the crystal is indication for the presence of some Yb^{2+}, and therefore the Yb^{3+} concentration is likely to be smaller than the above value.

Polarized absorption spectra were recorded on a double-beam spectrophotometer with the sample cooled to 19 K by a closed-cycle helium refrigerator. An argon-ion laser pumped Ti:sapphire laser was used as excitation source for the near-infrared luminescence and luminescence excitation spectra. The sample luminescence was dispersed by a 1-m single monochromator and detected by a cooled InGaAs diode using a lock-in amplifier. The unpolarized Raman spectra were obtained using the polarization-scrambled 488.0 or 514.5-nm line of an argon-ion laser. The Raman spectrum was independent on the choice of either one of these wavelenghts. The scattered light was collected in a backscattering arrangement, dispersed by a 1-m double monochromator, and detected by a photomultiplier and a photon counter. Unpolarized resonant Raman experiments using an argon-ion-laser pumped Ti:sapphire laser as excitation source were

recorded in a similar geometry with the sample cooled to 12 K by a closed-cycle helium refrigerator. The scattered light was dispersed by a triple monochromator and detected by a liquid-nitrogen-cooled CCD detector.

Except for the absorption and the resonant Raman spectra, all experiments were carried out at either 78.5 or 15.5 K with the sample mounted in a cold-finger cryostat.

III. RESULTS AND DISCUSSION

A. *4f* Energy Levels of Yb^{3+} in $CsCdBr_3$

The diamagnetic salt $CsCdBr_3$ is a member of the inverse perovskite family with the hexagonal $CsNiCl_3$ structure [12]. It crystallizes in the D_{6h}^4 space group and consists of linear chains of face-sharing $[CdBr_6]^{4-}$ units with the chains being arranged along the crystallographic c-axis and the Cs^+ ions occupying high-symmetry sites between the chains. It was first shown by EPR measurements that trivalent rare-earth ions (RE^{3+}) preferentially are incorporated as charge compensated RE^{3+}-vacancy-RE^{3+} ion pairs [13,14] having an RE^{3+}-RE^{3+} intra ion-pair distance of approximately 6.0 Å [14]. Several other RE^{3+} minority sites have since been identified. The point symmetry for a RE^{3+} ion on a Cd^{2+} site is C_{3v} [15-19] thus, for odd *4f*-electron systems, the $^{2S+1}L_J$ multiplets are split into $(2J+1)/2$ Kramers doublets.

In its $[Xe]4f^{13}$ electron configuration, Yb^{3+} only has two multiplets, *i.e.* a $^2F_{7/2}$ ground state and a $^2F_{5/2}$ excited state which, in C_{3v} symmetry, are split into 4 and 3 crystal-field levels labeled (0), (1), (2), (3) and (0'), (1'), (2'), respectively. The three prominent lines observed at 10122, 10138, and 10599 cm^{-1} in the 19-K absorption spectrum (Figure 1) can consequently be assigned to the (0)→(0',1',2') zero-phonon transitions of Yb^{3+}, respectively. Each of the transitions is accompanied by a multi-peak

6

sideband which results from electron-phonon interactions discussed in Sections III. B and C. The $(0)\rightarrow(0',1',2')$ energies are very similar to those measured in $Cs_3Yb_2Br_9$ (10119, 10146, 10590 cm^{-1}, respectively [20]) in which Yb^{3+} has a 6-fold bromide coordination geometry closely resembling the one of Yb^{3+} in $CsCdBr_3:Yb^{3+}$. From the luminescence spectrum (Figure 2), the $(0')\rightarrow(0,1,2,3)$ transitions are found at 10122, 10007, 9955, and 9658 cm^{-1}, along with the $(1')\rightarrow(0,1,2,3)$ transitions which are observed as a result of thermal population of (1') at 15.5 K. These energies indicate a ground-state splitting of 0, 115, 167, and 464 cm^{-1} which again is quite similar to that found in $Cs_3Yb_2Br_9$ (0, 114, 140, 441 cm^{-1} [20]). Both the ground and excited-state splittings reflect the dominance of the octahedral over the trigonal component of the crystal field, since the (0)-(1,2)-(3) and the (0',1')-(2') splittings are much larger than the (1)-(2) and (0')-(1') splittings. The $^2F_{7/2}$ and $^2F_{5/2}$ crystal-field energies determined here agree with those reported in an earlier study [21] except for (2) and (2'). A small, unexplained shift of the $(0)\rightarrow(2')$ transition to higher frequency with increasing temperature was observed. Therefore, the slight discrepancy in these energies between the two studies most likely result from the different temperatures (10 K vs. 15.5 K) at which the spectra were recorded.

B. Bulk and Local Modes in $CsCdBr_3:Yb^{3+}$

The Raman-active first-order normal modes (corresponding to phonons near $k=0$ around the Brillouin zone center) of the $CsCdBr_3$ host can be derived from a nuclear site group analysis of the unit cell [22,23]. In the D_{6h}^4 space group of $CsCdBr_3$ with two formula units in the primitive unit cell, the Cs, Cd, and Br atoms occupy sites of D_{3h}^1, D_{3d}, and C_{2v}^1 symmetry, respectively [24]. These three sites give rise to the modes $A_{2u}+B_{1g}+E_{1u}+E_{2g}$, $A_{2u}+B_{2u}+E_{1u}+E_{2u}$, and $A_{1g}+A_{2g}+A_{2u}+B_{1g}+B_{1u}+B_{2u}+E_{1g}+2E_{1u}+2E_{2g}+E_{2u}$, respectively, with the modes $A_{2g}+2B_{1g}+B_{1u}+2B_{2u}+2E_{2u}$ being silent and $A_{2u}+E_{1u}$ being the acoustic modes [23]. From the remaining active optical modes

7

$2A_{2u}+3E_{1u}+A_{1g}+E_{1g}+3E_{2g}$, which we refer to as bulk modes, $A_{1g}+E_{1g}+3E_{2g}$ are Raman active. All these modes are observed in the unpolarized Raman spectrum shown in Figure 3. Both the energies and relative intensities of the Raman transitions are in agreement with previously reported Raman spectra of undoped $CsCdBr_3$ [25, 26].

Pronounced vibronic sidebands are observed in both the absorption spectrum (Figure 1) and the luminescence spectrum (Figure 2). In the discussion below, we focus on the $(0)\rightarrow(2')$ zero-phonon line and its vibronic sideband since it is well separated in frequency from all the other transitions. The luminescence excitation spectrum of the vibronic sideband accompanying this $(0)\rightarrow(2')$ zero-phonon line (Figure 3) reveals quite a complex structure, with many more lines spanning a wider frequency range than in the Raman spectrum. Such a pronounced qualitative difference between the Raman spectrum and the vibronic sideband is typically not observed for rare-earth-ion doped solids in which the RE^{3+} ions substitute for chemically alike ions. We do not attempt to analyze all the features of the sideband shown in Figure 3. Rather we focus on the highest-energy transitions which are distinct and well isolated. In the isostructural compounds $CsCoCl_3$ and $CsMgCl_3$, the A_{1g} bulk mode was found to have the highest frequency of all the Raman and IR-active optical modes [27]. Also, no modes with frequency higher than the A_{1g} bulk mode were found in an analysis of vibronic sidebands in $CsCdBr_3:Co^{2+}$ [25]. We therefore assume that the A_{1g} Raman transition at 162.5 cm^{-1} represents the highest-energy, first-order bulk mode in $CsCdBr_3$. The highest-energy, first-order feature in the vibronic sideband on the other hand is observed at 191 cm^{-1}, a frequency close to the value (190 cm^{-1}) which was observed for the highest-energy mode in both $Cs_3Yb_2Br_9$ and $Cs_3Er_2Br_9$ crystals with six-fold bromide coordination [20,28]. As shown in the inset of Figure 3, the 191 cm^{-1} mode in the vibronic sideband is also discernible as a very weak feature in the Raman spectrum. Since there are no second-order Raman transitions which could give rise to a transition at this frequency, we assign this weak Raman transition to the A_{1g} local mode associated with the $[YbBr_6]$ coordination unit. This assignment is directly confirmed by resonant Raman experiments. Figure 4 shows the Raman intensity of the 191-cm^{-1} local mode (I_L) relative to that of the 162.5-cm^{-1} bulk mode (I_B) as a

function of excitation frequency and compares I_L/I_B with the unpolarized $(0)\rightarrow(2')$ absorption spectrum. The increase of I_L/I_B by approximately a factor of two on the $(0)\rightarrow(2')$ resonance is direct evidence that the 191-cm^{-1} mode in the Raman spectra is due to a local mode associated with Yb^{3+}.

The relative frequencies of the A_{1g} local and the A_{1g} bulk modes can be explained on the basis of a simple model. These modes represent totally-symmetric stretching vibrations of the M-Br bond (M=Cd,Yb), with frequencies proportional in a first approximation to $\sqrt{k/\mu}$, where k is the force constant and μ is the reduced mass. Their relative frequencies should therefore be given by

$$\frac{E_{YbBr}}{E_{CdBr}} = \sqrt{\frac{k_{YbBr}\mu_{CdBr}}{k_{CdBr}\mu_{YbBr}}} \quad . \tag{1}$$

Assuming the six M-Br bonds to be equivalent, each of the Br$^-$ ions shares $\frac{1}{6}$ of the charge of the metal ion in the [MBr$_6$] coordination unit, i.e. $\frac{1}{2}$ and $\frac{1}{3}$ of an elementary charge for [YbBr$_6$] and [CdBr$_6$], respectively. Further assuming the force constant to be a linear function of the ionic bond strength, a ratio of $E_{YbBr}/E_{CdBr} = 1.132$ is predicted from Eq.(1). This value is within 4% of the experimental ratio $191/162.5 = 1.175$, providing further support for the mode assignments.

The fact that the A_{1g} local-mode frequency is so similar to the respective frequency in Cs$_3$Yb$_2$Br$_9$ but significantly different from the A_{1g} bulk-mode frequency indicates a high degree of flexibility in the $\left[CdBr_3^-\right]_n$ linear chains of CsCdBr$_3$. Obviously, forces exerted by the host lattice do not constrain the [YbBr$_6$] normal-mode frequencies to be the same as CsCdBr$_3$ bulk-mode frequencies. The Yb^{3+} defect site is apparently able to accommodate local forces by bending of adjacent metal-halogen-metal bond angles. This flexibility of the $\left[CdBr_3^-\right]_n$ linear chains is reflected not only in the large angular distribution of the crystallographic c-axis of $11\pm2°$ measured in CsCdBr$_3$:Pr^{3+} using hole-burning Stark spectroscopy [29] but also in the fact that metal

ions over a wide range of charge, size, and chemical characteristics can be doped in significant amounts into crystals of the $CsCdBr_3$ family [24].

In Figure 3, a weak transition in the excitation sideband at 164 cm^{-1} coincides with the strong A_{1g} bulk mode observed at 162.5 cm^{-1} in the Raman spectrum. This weak transition may be either of a vibronic or an electronic nature. Cooperative electronic transitions on the Yb^{3+} ion pairs in this material are likely and, for example, two excited Yb^{3+} ions cooperatively relaxing from their $^2F_{5/2}$ excited state in a radiative $[^2F_{5/2}(i'),^2F_{5/2}(j')] \rightarrow [^2F_{7/2}(m),^2F_{7/2}(n)]$ transition can give rise to intense green cooperative luminescence in $CsCdBr_3:Yb^{3+}$ [21]. In analogy, cooperative electronic transitions of the type $[^2F_{7/2}(i),^2F_{7/2}(j)] \rightarrow [^2F_{5/2}(m'),^2F_{7/2}(n)]$ can occur in the near infrared spectral region [20]. From the energy levels calculated in Section III.A, the transition $[^2F_{7/2}(0),^2F_{7/2}(0)] \rightarrow [^2F_{5/2}(2'),^2F_{7/2}(2)]$ is expected at 10766 cm^{-1}, *i.e.* at a frequency 167 cm^{-1} above the $(0) \rightarrow (2')$ zero-phonon line. We do not have enough experimental information to assess the contribution of this electronic process to the transition intensity around 164 cm^{-1}. However, it is likely to be small, since the observation of a progression in a vibrational mode of approximately 164 cm^{-1} (see Section III.C) indicates significant vibronic character of the 164 cm^{-1} transition. Moreover, a transition at 162 cm^{-1} was also observed in $CsCdBr_3:Pr^{3+}$, which has a different ground-state splitting [30]. Therefore, this transition arises mainly from coupling of the $(0) \rightarrow (2')$ electronic transition either to the A_{1g} bulk mode in the second coordination sphere or to an odd-parity local mode of the $[YbBr_6]$ coordination unit with a frequency similar to the A_{1g} bulk mode.

In the vibronic sideband accompanying the $^3H_4(0) \rightarrow ^3P_0(0)$ zero-phonon line in $CsCdBr_3:Pr^{3+}$, the A_{1g} local mode of the $[PrBr_6]$ coordination unit appears at 194 cm^{-1}, and another, fairly broad vibronic transition appears at 162 cm^{-1} [30]. The slight increase of the A_{1g} local mode frequency from 191 cm^{-1} in $CsCdBr_3:Yb^{3+}$ to 194 cm^{-1} in $CsCdBr_3:Pr^{3+}$ is expected, due to the smaller mass of Pr^{3+} relative to Yb^{3+}. However the fact that the 164 cm^{-1} mode frequency in $CsCdBr_3:Yb^{3+}$ does not increase by going to $CsCdBr_3:Pr^{3+}$ is indication for this transition not being a result of vibronic coupling to a

local mode but arising from vibronic coupling of the (0)→(2') electronic transition beyond the first [YbBr$_6$] coordination sphere to the A$_{1g}$ bulk mode.

These results clearly show that vibronic coupling occurs almost exclusively to the local modes of the first coordination sphere with minor contributions from the second or higher coordination spheres, *i.e.* a maximum vibronic interaction radius of ≈3 Å. In terms of electron-phonon interactions enabling non-radiative relaxation processes such as multiphonon relaxation or phonon-assisted energy transfer, this conclusion implies that most of the energy released by these processes is first transferred to the local modes of the first coordination sphere. The subsequent distribution of this vibrational energy among the various bulk modes requires resonances of those bulk modes with the local modes, a condition which may not be well satisfied for defect materials such as RE^{3+}-doped CaF$_2$, CdF$_2$, CsMgCl$_3$, or CsCdBr$_3$. Time-resolved Raman studies, such as those carried out for Cr^{4+}-doped forsterite [31], could provide further insight into the details of the non-radiative relaxation dynamics in these materials. They might also answer the question as to whether or not the lack of any strong resonances between local and bulk modes contributes, together with the overall low frequencies of phonons in CsCdBr$_3$, to suppression of non-radiative relaxation of RE^{3+} excited states in this material.

C. Electron-Phonon Interaction

Two mechanisms, usually referred to as M and Δ process [32], can mediate the interaction of the electronic and the vibrational system. The M process induces vibronic intensity through admixture of even-parity wavefunctions (*e.g.* from the $4f^{N-1}5d$ configuration) to the odd-parity $4f^N$ wavefunctions by coupling to an odd-parity (IR-active) vibration [3, 33-35]. Such vibrationally-induced, forced electric-dipole transitions lead, for example, to vibronic transitions with a frequency differing by exactly one vibrational quantum from the zero-phonon line. The Δ or Franck-Condon process on the

other hand induces vibronic intensity through slightly different equilibrium structures of electronic ground and excited states [36]. In contrast to the M process, the shift of the excited-state relative to the ground-state potential surface along one of the configurational coordinates, measured in terms of the Huang-Rhys factor S, gives rise to phonon replica in the respective mode. In the harmonic approximation, the probability of a vibronic transition from an electronic state a and vibrational state n to an electronic state b and vibrational state m is given by

$$P_{a_n \to b_m} = P_{ab} \left| \left\langle \chi_b(m) | \chi_a(n) \right\rangle \right|^2 \tag{2}$$

where P_{ab} is the purely electronic transition probability, which is identical for all the vibrational states m and n, and $\left| \left\langle \chi_b(m) | \chi_a(n) \right\rangle \right|^2$ is the vibrational overlap integral or Franck-Condon factor, which is a measure of the electron-phonon coupling strength [36]. At zero Kelvin, the relative transition probability for the ith phonon replica, given by $P_{a_0 \to b_i} = P_{ab} \left| \left\langle \chi_b(i) | \chi_a(0) \right\rangle \right|^2$, is [37]

$$\frac{P_{a_0 \to b_i}}{P_{ab}} = \frac{S^i e^{-S}}{i!} \tag{3}$$

Numerous studies in recent years have found that earlier assumptions that the Huang-Rhys factor is zero, implying that the M process dominates the RE^{3+}-ion vibronic intensities, were often not justified. The observation of vibronic transitions in the two-photon spectra of $SrMoO_4:Pr^{3+}$ [38] and of two-phonon replica in $Na_5La(MO_4)_4:Pr^{3+}$ (M=Mo,W) [39] provides direct evidence for the important role that the Δ process can play.

As shown in Figure 5, the bulk and local modes ν_B and ν_L observed at 164 and 191 cm^{-1} in the vibronic sideband of the luminescence excitation spectrum appear as very weak two-phonon replicas at 323 and 383 cm^{-1}, respectively. That is, they appear at approximately twice thier respective fundamental frequencies. This is direct evidence for

12

a Δ process inducing the vibronic intensity. This result is consistent with selection rule considerations since both the modes ν_B and ν_L were assigned to A_{1g} modes, which as even-parity modes cannot enable M processes. The two-phonon frequencies are at ≈ 1.96 and ≈ 2.01 times the one-phonon frequencies for the modes ν_B and ν_L, respectively, indicating the highly harmonic nature of the excited-state potential surface. Note that the combination mode $\nu_B + \nu_L$ is also observed.

By using Eq.(3) it is possible, in principle, to calculate the Huang-Rhys factors S from the ratios of transition probabilities $P_{a_0 \rightarrow b_1} / P_{ab}$ and $P_{a_0 \rightarrow b_2} / P_{ab}$ derived from experimental transition intensities I in the luminescence excitation spectrum (Figure 5). Under the experimental conditions used for measuring the luminescence excitation spectra, however, it is likely that the strongly absorbing zero-phonon line is partially saturated, *i.e.* its intensity is not proportional to P_{ab}. Consequently, the above two ratios would be overestimated, a complication in numerous past studies [4].

Instead, we assume that the weakly absorbing vibronic transitions are unaffected by saturation (*i.e.* $I \propto P$), and we only calculate the ratio $I_{a_0 \rightarrow b_2} / I_{a_0 \rightarrow b_1} = \frac{1}{2} S$ using Eq.(3) and the spectra of Figure 5. For the modes ν_B and ν_L we then obtain $S_{Bulk} = 0.15 \pm 0.03$ and $S_{Local} = 0.010 \pm 0.002$, respectively. Note that $S_{Bulk} > S_{Local}$. This result reflects the fact that the relative intensity of the modes ν_B and ν_L in the one-phonon and two-phonon replica (Figure 5) is reversed. Although both Huang-Rhys factors found here are within the typical range of values reported for other RE^{3+}-doped solids [7,39], they indicate quite different electron-phonon coupling strengths of the two modes.

Whereas the configurational coordinate for the A_{1g} local mode is most likely the (average) Yb-Br bond length, the configurational coordinate describing the coupling to the bulk mode in the second coordination sphere or beyond is not directly obvious. The relatively large value of S_{Bulk} indicates the occurrence of local structural changes upon excitation of the respective vibronic transitions and, on the basis of both the one-dimensional nature of $CsCdBr_3$ and the structure of the dominant Yb^{3+} pair center in $CsCdBr_3$, we can speculate on the nature of this structural rearrangement. From our results on the spatial extension of electron-phonon interactions (Section III.B) we

13

conclude that vibronic coupling is not only confined to within the linear chains in $CsCdBr_3$ but more specifically does not extend beyond the vibrational modes of the nearest-neighbor coordination units in the chain. With the dominant Yb^{3+} pair center being a Yb^{3+}-vacancy-Yb^{3+} arrangement, the Yb^{3+} ion therefore typically has a $[CdBr_6]$ coordination unit on one side and a $[Vacancy-Br_6]$ coordination unit on the other side along the linear chain. Since the vacancy is likely to be easily compressed, the vibronic excitation of the A_{1g} bulk mode, which involves stretching of the Cd-Br bonds, may push the Yb^{3+} ion towards the vacancy and thus induce changes in bond lengths and angles of the bromide ions linking the Yb^{3+} and the Cd^{2+} ion. The overall result of this vibronic excitation would be the introduction of coupling between local and bulk modes and a reduction of the Yb^{3+}-Yb^{3+} distance. While there is currently no experimental evidence supporting this picture, we wish to point out that EPR measurements on a sample strongly excited into the bulk-mode vibronic transition at 162.5 cm^{-1} could provide direct information on the magnitude of this structural rearrangement [14].

IV. CONCLUSIONS

The incorporation of Yb^{3+} into $CsCdBr_3$ leads to the formation of $[YbBr_6]$ coordination units, the vibrational properties of which differ markedly from those of the host lattice. From a comparison of Raman spectra which probe host vibrations, and Yb^{3+} luminescence excitation spectra which provide a probe of local vibrations, we have shown that vibronic coupling occurs predominantly to modes of the first coordination sphere, and that vibronic contributions from the second or higher coordination sphere are weak. The spatial extent of electron-phonon interactions is estimated to be approximately 3 Å. These results all have important consequences for phonon-assisted energy transfer and multiphonon relaxation of RE^{3+} excited states. The present research has shown that vibrational energy release during relaxation of the electronic excited state of Yb^{3+} occurs through excitation first of local modes, and subsequently via energy transfer through resonances with bulk modes which complete the nonradiative relaxation process. For materials such as RE^{3+}-doped $CsCdBr_3$, where local and bulk mode frequencies differ markedly, the significant detuning of many such potential resonances undoubtedly suppresses some relaxation pathways.

REFERENCES

[1] K.H. Hellwege, Ann. Phys. **40**, 529 (1941).

[2] W.F. Krupke, Phys. Rev. **145**, 325 (1966).

[3] G. Blasse, Int. Rev. Phys. Chem. **11**, 71 (1992).

[4] G. Blasse, A. Meijerink, and C. de Mello Donegá, J. Alloys Comp. **225**, 24 (1995).

[5] L.-S. Lee, S.C. Rand, and A.L. Schawlow, Phys. Rev. B **29**, 6901 (1984).

[6] C. de Mello Donegá and G. Blasse, Chem. Phys. Lett. **183**, 367 (1991)

[7] C. de Mello Donegá, A. Meijerink, and G. Blasse, J. Phys.: Condens. Matter **4**, 8889 (1992).

[8] A. Meijerink, C. de Mello Donegá, A. Ellens, J. Sytsma, and G. Blasse, J. Lumin. **58**, 26 (1994).

[9] A. Meijerink, G. Blasse, J. Sytsma, C. de Mello Donegá, and A. Ellens, Acta Phys. Pol. A **90**, 109 (1996).

[10] G. Blasse and G.J. Dirksen, J. Solid State Chem. **96**, 258 (1992).

[11] G. Meyer, Inorg. Synth. **25**, 146 (1989).

[12] D. Visser, G.C. Verschoor, and D.J.W. Ijdo, Acta cryst. **B36**, 28 (1980).

[13] G.L. McPherson and L.M. Henling, Phys. Rev. B **16**, 1889 (1977).

[14] L.M. Henling and G.L. McPherson, Phys. Rev. B **16**, 4756 (1977).

[15] R.B. Barthem, R. Buisson, and R.L. Cone, J. Chem. Phys. **91**, 627 (1989).

[16] N.J. Cockroft, G.D. Jones, and R.W.G. Syme, J. Lumin. **43**, 275 (1989).

[17] J.P. Chaminade, R.M. Macfarlane, F. Ramaz, and J.C. Vial, J. Lumin. **48&49**, 531 (1991).

[18] N.J. Cockroft, G.D. Jones, and D.C. Nguyen, Phys. Rev. B **45**, 5187 (1992).

[19] F. Ramaz, R.M. Macfarlane, J.C. Vial, J.P. Chaminade, and F. Madéore, J. Lumin. **55**, 173 (1993).

[20] M.P. Hehlen and H.U. Güdel, J. Chem. Phys. **98**, 1768 (1993).

[21] Ph. Goldner, F. Pellé, D. Meichenin, and F. Auzel, J. Lumin. **71**, 137 (1997).

[22]   J.P. Mathieu, *Spectres de vibration et symmetrie*, Herman et Cie, Paris (1945).

[23]   D.L. Rousseau, R.P. Bauman, and S.P.S. Porto, J. Raman Spectr. **10**, 253 (1981).

[24]   G.L. McPherson and A.M. McPherson, J. Phys. Chem. Solids, **41**, 495 (1980).

[25]   C.W. Tomblin, G.D. Jones, and R.W.G. Syme, J. Phys. C **17**, 4345 (1984).

[26]   O. Pilla, E. Cazzanelli, B. Blanzat, C. Andraud, and F. Pellé, Phys. Stat. Sol. (b) **144**, 845 (1987).

[27]   G.L. McPherson and Jin Rong Chang, Inorg. Chem. **12**, 1196 (1973).

[28]   M.P. Hehlen, K. Krämer, H.U. Güdel, R.A. McFarlane, and R.N. Schwartz, Phys. Rev. B **49**, 12475 (1994).

[29]   F. Ramaz, J.C. Vial, and R.M. Macfarlane, Europhys. Lett. **22**, 217 (1993).

[30]   J. Neukum, N. Bodenschatz, and J. Heber, Phys. Rev. B **50**, 3536 (1994).

[31]   S.G. Demos, D.M. Calistru, and R.R. Alfano, Appl. Phys. Lett. **68**, 1195 (1996).

[32]   T. Miyakawa, in *Luminescence of Crystals, Molecules, and Solutions*, ed. F. Williams, Plenum, New York 1973.

[33]   T.R. Faulkner and F.S. Richardson, Mol. Phys. **35**, 1141 (1978).

[34]   B.R. Judd, Physica Scripta **21**, 543 (1980).

[35]   J. Dexpert-Ghys and F. Auzel, J. Chem. Phys. **80**, 4003 (1984).

[36]   B. Henderson and G.F. Imbusch, *Optical Spectroscopy of Inorganic Solids*, Clarendon Press, Oxford 1989.

[37]   T. Keil, Phys. Rev. **140**, A601 (1965).

[38]   C. de Mello Donegá and A. Meijerink, J. Lumin. **55**, 315 (1993)

[39]   C. de Mello Donegá, S. Schenker, H.F. Folkerts, A. Meijerink, and G. Blasse, J. Phys.: Condens. Matter **6**, 6043 (1994).
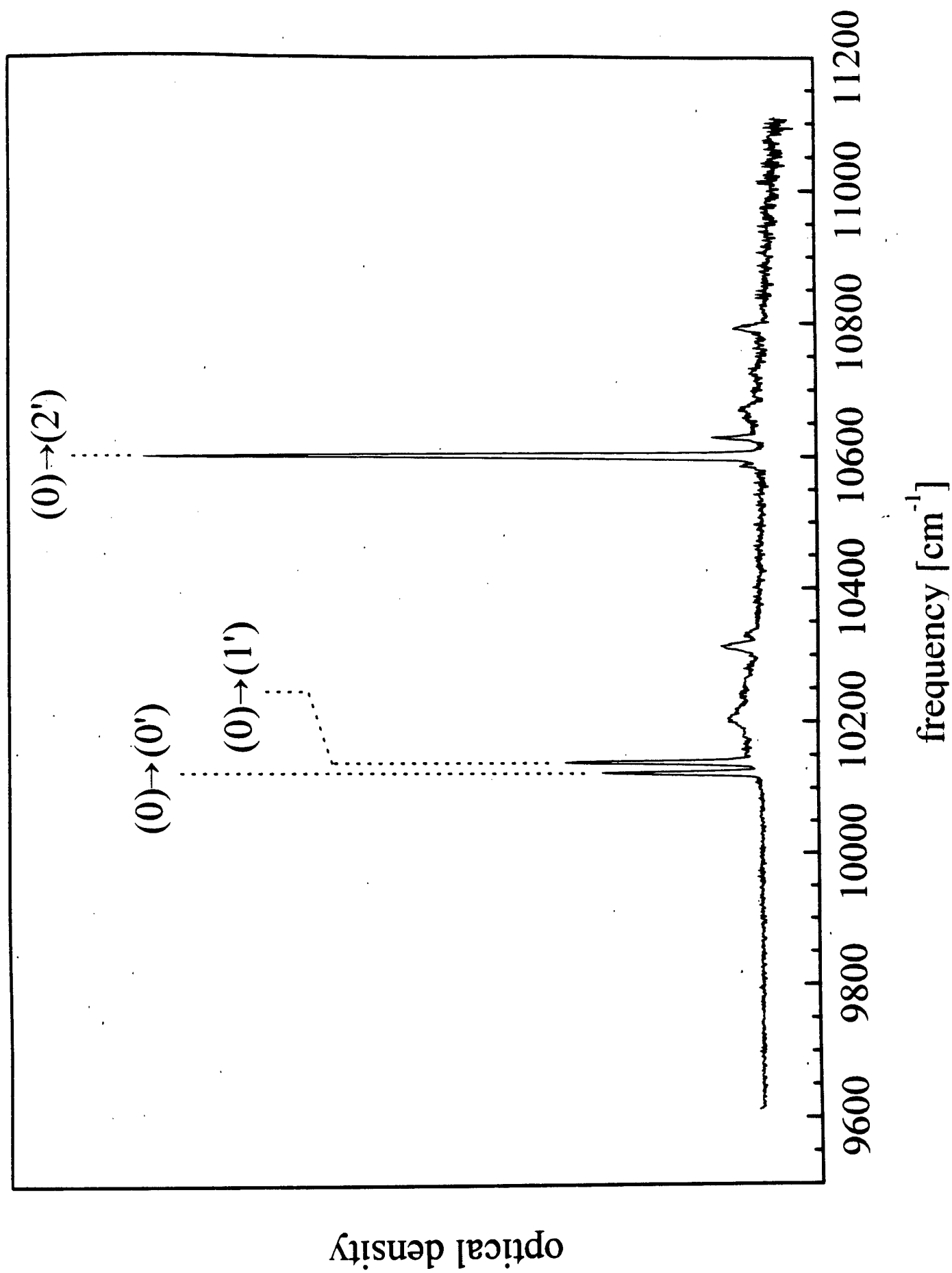
FIGURE CAPTIONS

Figure 1: Unpolarized $^2F_{7/2} \rightarrow {}^2F_{5/2}$ absorption spectrum of $CsCdBr_3:Yb^{3+}$ at 19 K. The labels (0) and (0',1',2') refer to the crystal-field levels of the $^2F_{7/2}$ ground state and $^2F_{5/2}$ excited-state multiplet, respectively.

Figure 2: Unpolarized $^2F_{5/2} \rightarrow {}^2F_{7/2}$ luminescence spectrum of $CsCdBr_3:Yb^{3+}$ at 15.5 K. The labels (0,1,2,3) and (0',1') refer to the crystal-field levels of the $^2F_{7/2}$ ground state and $^2F_{5/2}$ excited-state multiplet, respectively.
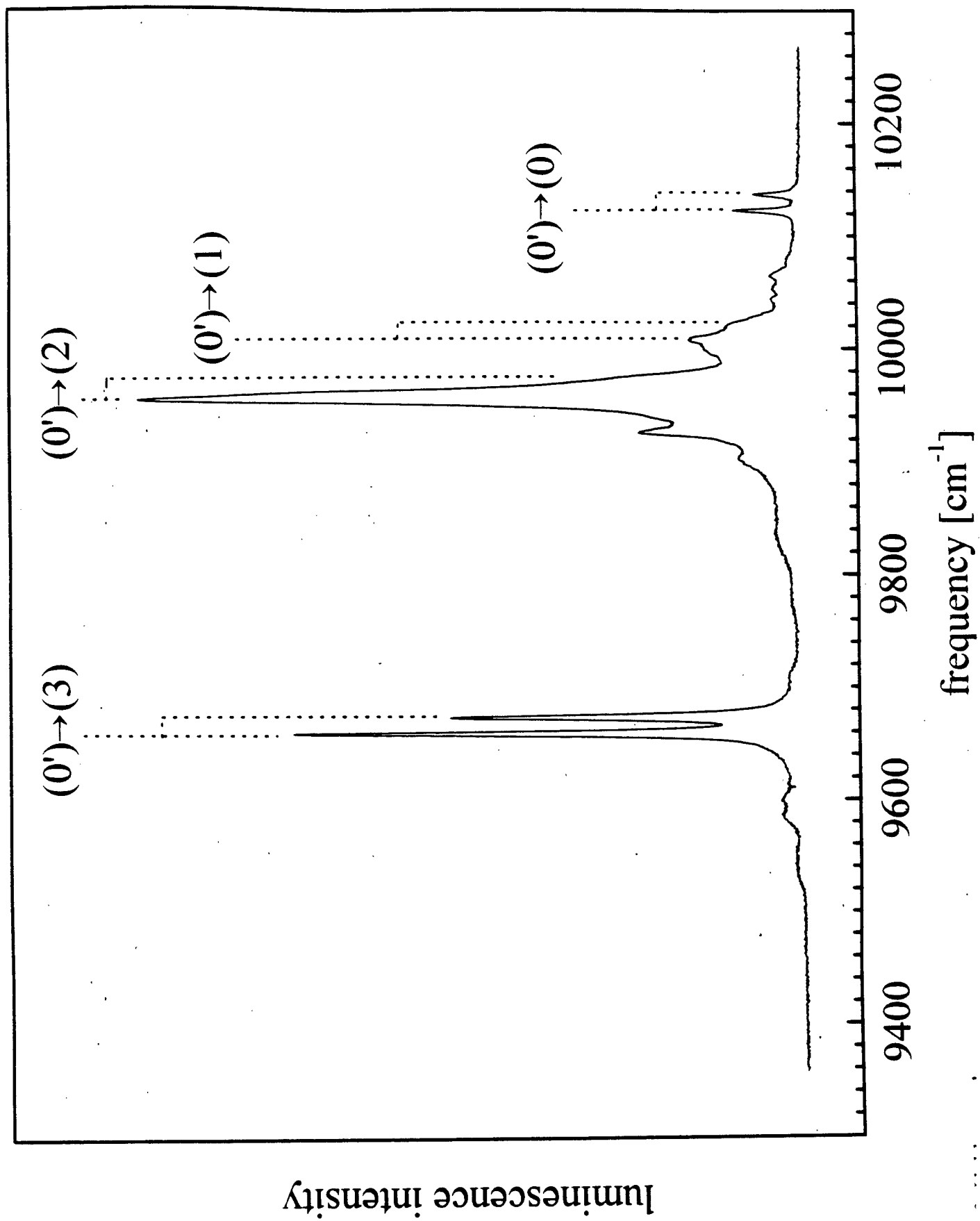
Figure 3: Unpolarized Raman spectrum of $CsCdBr_3:Yb^{3+}$ with the incident laser wavelength at 514.5 nm (top trace) and unpolarized luminescence excitation spectra obtained by monitoring the (0')→(2) transition (Figure 2) at 1004.5 nm (bottom traces). For the Raman and excitation spectra the frequency is normalized to the incident laser and the (0)→(2') zero-phonon line (Figure 1), respectively. The assignments of the Raman transitions are taken from Ref. [25, 26]. The inset shows an enlargement of the Raman spectrum in the 180-200 cm^{-1} range.

Figure 4: Relative unpolarized Raman intensity of the bulk mode at 162.5 cm^{-1} (I_B) and the local mode at 191 cm^{-1} (I_L) as a function of the incident laser frequency in $CsCdBr_3:Yb^{3+}$ at 12 K. The enhancement of the ratio I_L/I_B on the (0)→(2') resonance is approximately a factor of two. Part of the unpolarized absorption spectrum (from Figure 1) is shown for comparison.

Figure 5: Unpolarized luminescence excitation spectra of $CsCdBr_3:Yb^{3+}$. ν_B and ν_L denote the bulk-mode and local-mode frequency respectively, and the left and right insets show the one-phonon and two-phonon replica of both these modes, respectively.

optical density

$(0)\rightarrow(2')$

$(0)\rightarrow(0')$

$(0)\rightarrow(1')$

frequency [cm^{-1}]

9600 9800 10000 10200 10400 10600 10800 11000 11200

Figure 3. Hehlen et al

one-phonon replica

two-phonon replica

ZPL
$(0) \rightarrow (2')$

ν_L
191
0

ν_B
164

78.5 K

$2\nu_B$
323

$2\nu_L$
383

78.5 K

$\nu_B + \nu_L$
355

15.5 K

10750   10800   10850

10900   10950   11000   11050

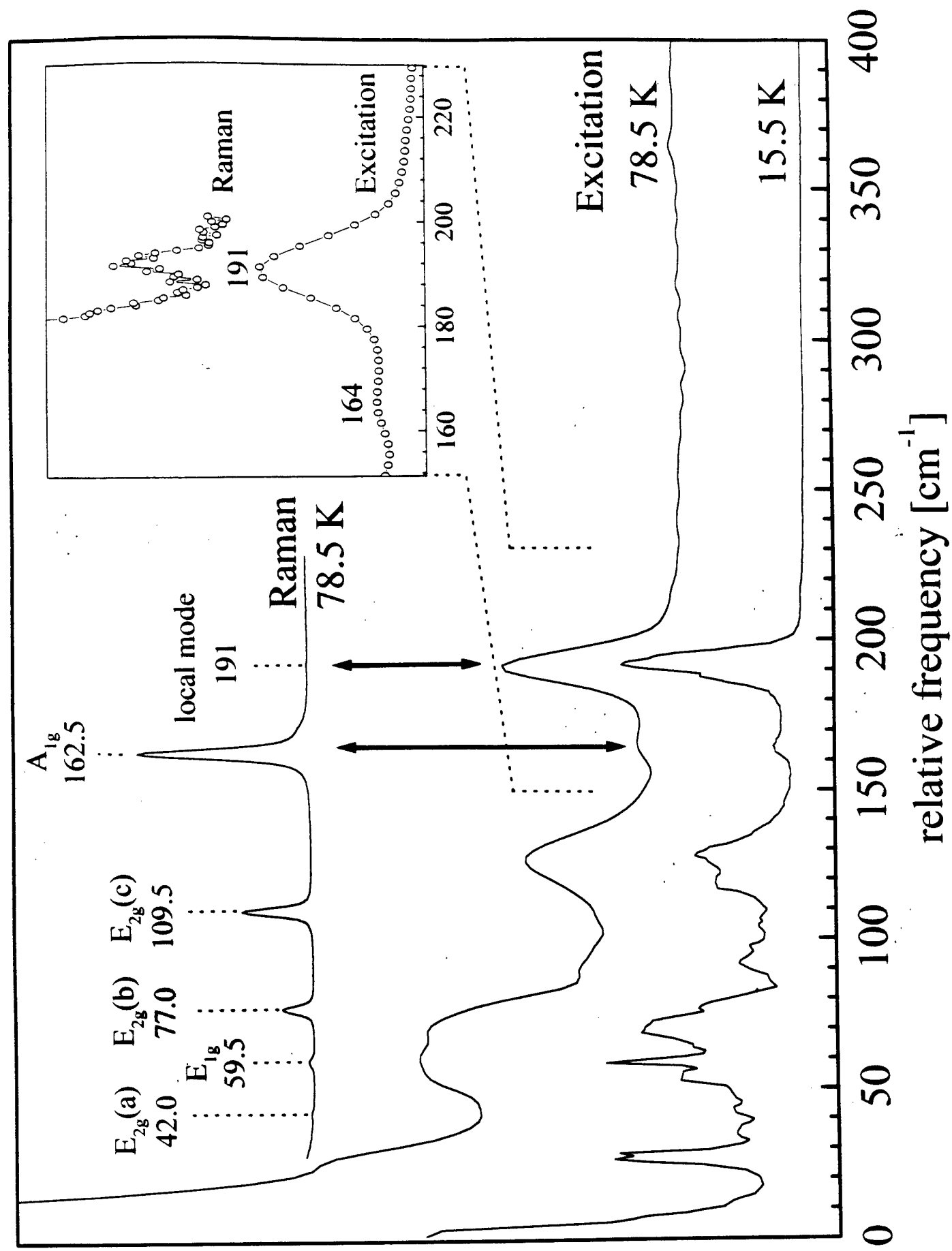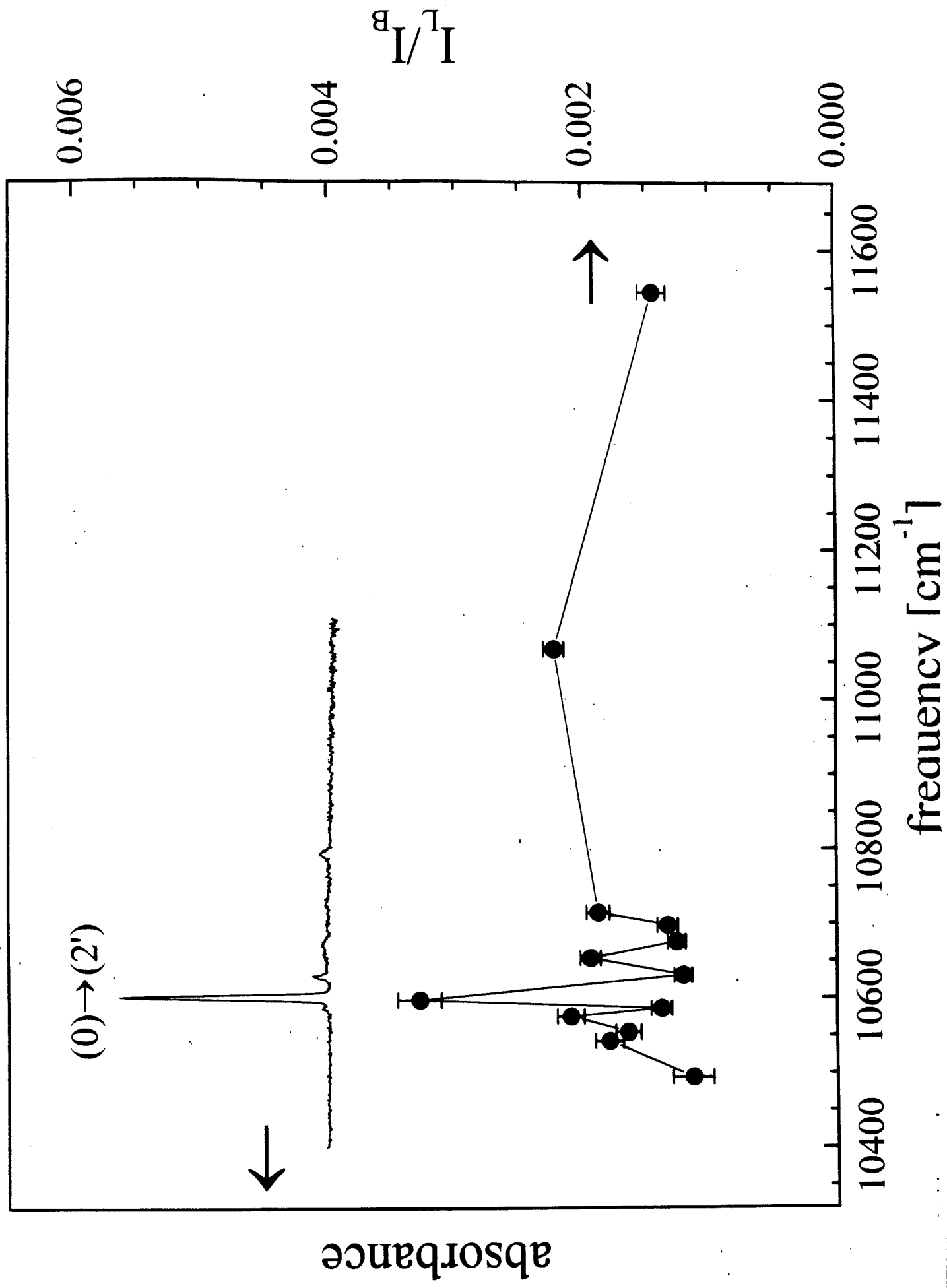10600   10700   10800   10900   11000   11100

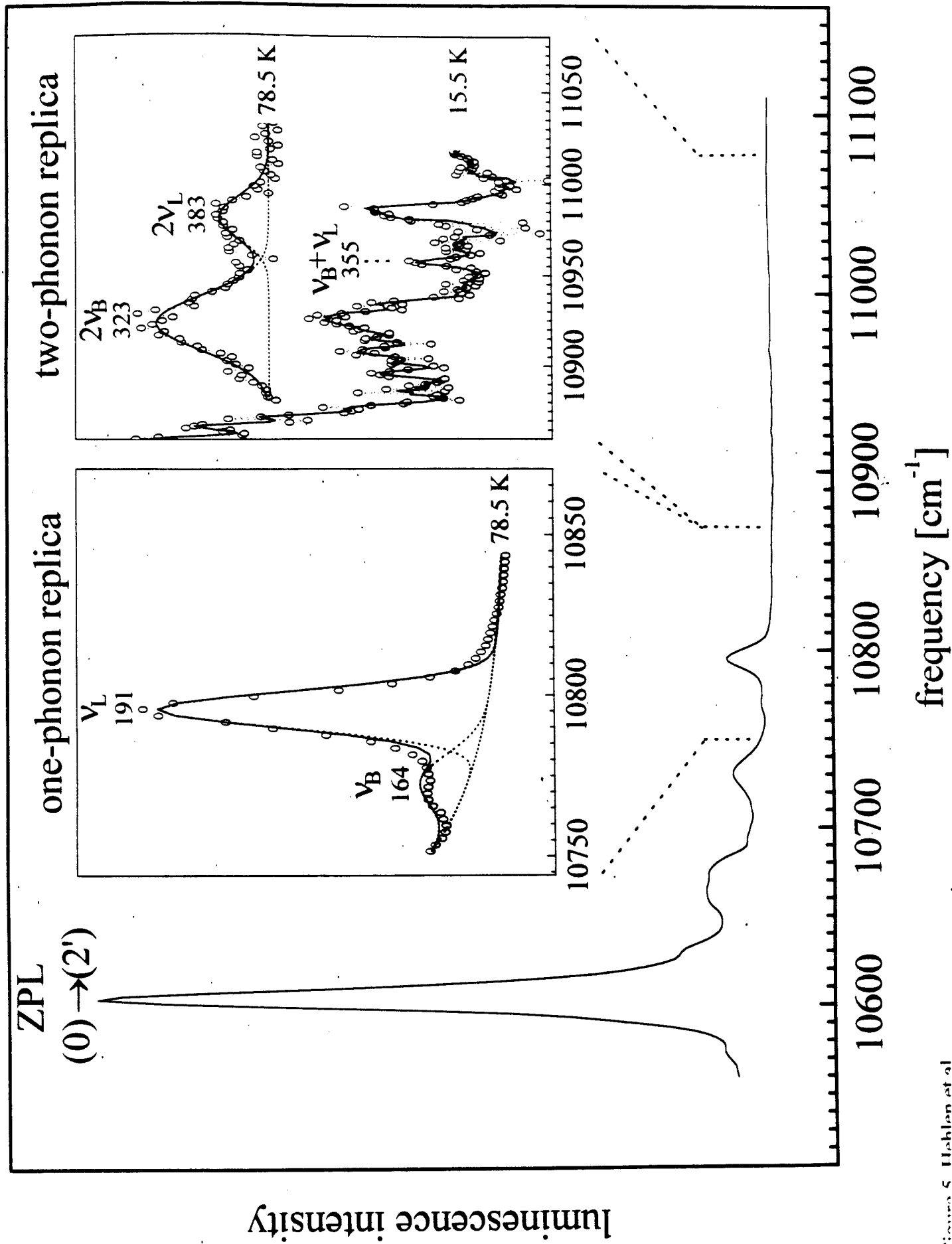frequency [cm^{-1}]

luminescence intensity

Figure 5. Hahlen et al

Nonlinear dispersion of avalanche upconversion

Q. Shu, H. Ni, and S. C. Rand

Division of Applied Physics, 1049 Randall Laboratory, University of Michigan, Ann Arbor, Michigan 48109-1120

Two-beam coupling measurements of an avalanche upconversion transition in concentrated Tm·LiYF$_4$ confirm that, despite the resonant nature of the excited-state optical interaction, the induced response is strongly dispersive. This surprising characteristic is shown to be a general feature of avalanche polarization, with an off-resonant process dominating the resonant response. © 1997 Optical Society of America

In recent years simple implementations of two-beam coupling interactions[1] have been introduced for precision characterization of nonlinear coefficients[2] and for studying slow radiative and nonradiative decay processes within luminescent centers in solids.[3] Here we report results of nondegenerate two-beam coupling (TBC) mediated by delocalized, cooperative dynamics of impurity atoms on avalanche upconversion transitions[4] and use them to investigate an earlier indication from research by Ni[5] that avalanche nonlinearities are primarily dispersive, in apparent disagreement with existing models of resonant nonlinear response.[6] We confirm this general feature of avalanche nonlinearities that nonresonant contributions dominate the nonlinear polarization of this type of resonant interaction and point out several important applications.

Basic features of avalanche absorption were modeled by Kueny *et al.*[7] and others.[8] Those authors pictured the cross relaxation of one excited- and one ground-state ion, which resulted in two excited-intermediate-state ions, as a key step in the underlying nonlinear process leading to a chain reaction of excitation driven by excited-state absorption. Ni[9] subsequently pointed out the essential role of migration in the process, and numerous examples of avalanche absorption have since been reported.[10] Significant applications have emerged in the areas of avalanche upconversion lasers,[11] amplifiers,[12] and signal processing.[13] However, there have been few fundamental studies of the nonlinear-optical response associated with the avalanche itself. Here we provide direct evidence that the real part of the nonlinear index is much larger than the imaginary part, exactly in resonance with the avalanche transition.

In conventional theories of nonlinear optics a single strong input field in resonance with an allowed transition generates a purely absorptive change in the response. On the other hand, at large detunings the response is predicted to be dispersive. In avalanche upconversion an interesting situation is encountered in which two transitions are involved, one exactly on resonance and one far off resonance, as indicated at the left in Fig. 1(a). Intuitively, in the absence of coupling between the atoms one expects the resonant interaction to dominate. Hence the nonlinear response should be absorptive in character.

For coupled atoms, though, the situation is greatly modified. Above avalanche threshold, cross relaxation provides a mechanism for heavily populating excited states even when the initial optical interaction involving the ground state is far off resonance. The populations in excited states and the value of the predicted threshold intensity show little or no dependence on the weak ground-state absorption.[3,14] However, models that omit the ground-state transition altogether predict only nonlinear properties associated with the excited-state transition, which is purely absorptive on resonance. Because the excited state involved in the off-resonant ground-state transition can nevertheless be significantly populated because of avalanche processes, the polarization associated with the ground-state optical interaction is unexpectedly strong even when the ground-state absorption is negligible.

(a)

(b)
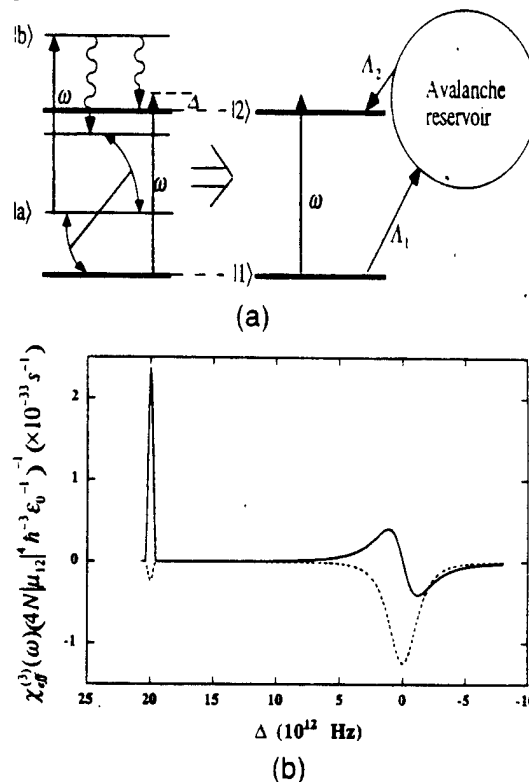
Fig. 1. (a) Reduction of a multilevel avalanche system to a two-level nonlinear system. Cross relaxation (curved arrows) and decay (wiggly arrows) account for incoherent pumping of excited states at large detunings from the ground-state transition. (b) Calculation of the susceptibility from Eq. (4). Solid dashed curves correspond to real and imaginary induced indices, respectively. The parameters used are $\Gamma_{21} = 2 \times 10^{12}$ s^{-1} and $\gamma_{21} = 2 \times 10^8$ s^{-1}.

To model this situation we replaced all but one excited state with an avalanche reservoir whose occupation is large but bears no particular phase relationship to the polarization developed on the off-resonant transition between the ground state and level $|2\rangle$. This quasi-two-level model is shown at the right in Fig. 1(a). Incoherent pumping and depletion of the reservoir are justified in the limit of large Δ by the spontaneous nature of the cross relaxation that populates state $|2\rangle$ and by spontaneous decay processes among excited levels. In steady state the equations of motion for the components of the density matrix are

$$\dot{\rho}_{11} = \gamma_{21}\rho_{22} - \Omega v - \Lambda_1 = 0, \tag{1}$$

$$\dot{\rho}_{22} = -\gamma_{21}\rho_{22} + \Omega v + \Lambda_2 = 0, \tag{2}$$

$$\dot{\tilde{\rho}}_{21} = -(\Gamma_{21} - i\Delta)\tilde{\rho}_{21} + \tfrac{1}{2}i\Omega(\rho_{22} - \rho_{11}) = 0. \tag{3}$$

Here γ_{21} and Γ_{21} are the population decay and the optical dephasing rates, respectively. $\Delta = \omega - \omega_{21}$ is the detuning of the incident frequency ω from transition frequency ω_{21} between levels $|1\rangle$ and $|2\rangle$, $\Omega = -2\mu_{32}\tilde{E}/\hbar$ for fields of the form $E = \tilde{E}\exp(-i\omega t) +$ c.c., $\tilde{\rho}_{21}$ is the slowly varying amplitude of the off-diagonal element ρ_{21} defined by $\rho_{21} = \tilde{\rho}_{21}\exp(-i\omega t)$, and v is the imaginary part of $\tilde{\rho}_{12} = \tilde{\rho}_{21}^* = u + iv$. Closure requires that $\rho_{11} + \rho_{22} + \rho_r = 1$, where reservoir population ρ_r gives the total population density circulating among excited states other than $|2\rangle$. In steady state $\Lambda_1 = \Lambda_2$, and we assume that this rate is proportional to occupation of the reservoir ($\Lambda_2 = f\rho_r$, where f is the rate at which reservoir atoms decay to level $|2\rangle$).

The steady-state polarization $P(t) = N\,\mathrm{Tr}(\rho\mu) = \tilde{P}(\omega)\exp(-i\omega t) + $ c.c. can be determined from Eqs. (1)–(3) and used to calculate an effective susceptibility χ_{eff} according to $\tilde{P}(\omega) = \epsilon_0\chi_{\mathrm{eff}}(\omega)\tilde{E}$. χ_{eff} consists of the usual linear susceptibility $\chi^{(1)}(\omega)$ and a nonlinear, intensity-dependent part $\chi^{(3)}_{\mathrm{eff}}(\omega)$. The nonlinear part is[14]

$$\chi^{(3)}_{\mathrm{eff}}(\omega) = \left[\frac{4N|\mu_{12}|^4\hbar^{-3}\epsilon_0^{-1}(\Delta - i\Gamma_{21})\Gamma_{21}/\gamma_{21}}{(\Delta^2 + \Gamma_{21}^2)(\Delta^2 + \Gamma_{21}^2 + |\Omega|^2\Gamma_{21}/\gamma_{21})} \right.$$
$$\left. + \frac{4N|\mu_{12}|^4\hbar^{-3}\epsilon_0^{-1}(\Delta - i\Gamma_{21})(1 + 2f/\gamma_{21})}{\Delta^2 + \Gamma_{21}^2 + |\Omega|^2\Gamma_{21}/\gamma_{21}}(\rho_r/|\Omega|^2) \right].$$
$$\tag{4}$$

The first term in Eq. (4) corresponds to saturation of a conventional two-level system, whereas the second term arises from the incoherent pumping channel. The relative contributions of the two terms for various detunings $\Delta' = \omega - \omega_{ba}$ of the light wave from the excited-state transition frequency vary considerably. For small detunings [$\Delta' = \Delta - (\omega_{ba} - \omega_{21}) \approx 0$] the first term may be much smaller than the second, because detuning from the ground-state transition under this condition ($\Delta = \omega_{ba} - \omega_{21}$) is necessarily large for avalanche processes. In this case the nonlinear susceptibility is dominated by a real contribution that peaks at the excited-state resonance, as shown in Fig. 1(b) ($\Delta' = 0 \to \Delta = 20$). On the other hand, when $\Delta = 0$ the first term can dominate, because ρ_r

tends to zero abruptly ($\Delta = 0$) and the avalanche is extinguished. This situation generates broad features in the vicinity of the ground-state resonance [$\Delta = 0$ in Fig. 1(b)], where the real nonlinear index passes through zero.

The total susceptibility is the sum of the off-resonant ground-state polarization from Eq. (4) and the resonant excited-state polarization that one obtains by ignoring the ground-state transition. The analytical results in Fig. 1(b) for optical susceptibility $\chi^{(3)}_{\mathrm{eff}}(\omega)$ based on microscopic avalanche dynamics can be compared directly with measurable index changes observed by two-beam coupling. In the weak probe limit, experimental values for the Debye decay time τ that characterize the saturation process, as well as real and imaginary parts n_2' and n_2'' of the nonlinear refractive index n_2 [directly proportional to $\chi^{(3)}_{\mathrm{eff}}(\omega)$], can be determined from the analysis of TBC spectra.

Experiments were performed with a pump–probe technique that we described previously, which makes use of a stabilized dye laser.[3] Only one improvement over our earlier approach was implemented here. The output was split into two beams propagating with polarizations parallel to the optic axis and a third beam, which did not pass through the sample but provided an intensity reference for a differencing signal amplifier
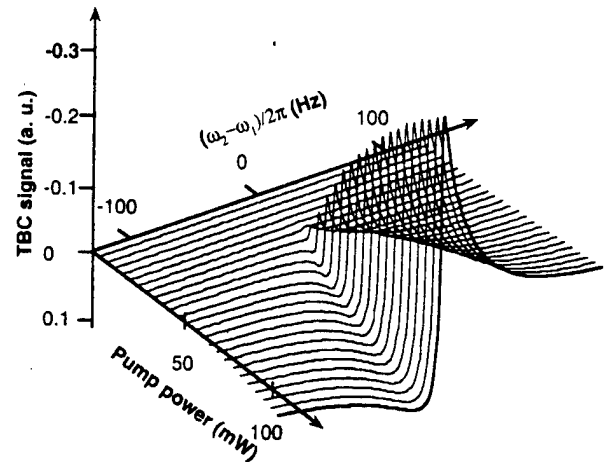

Fig. 2. Experimental two-beam coupling signals in Tm:LiYF$_4$ versus both pump–probe detuning and pump intensity.
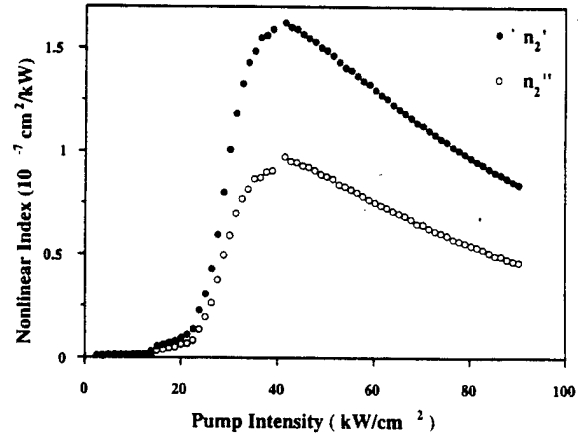

Fig. 3. Real (n_2') and imaginary (n_2'') nonlinear indices versus input intensity from data of Fig. 2.
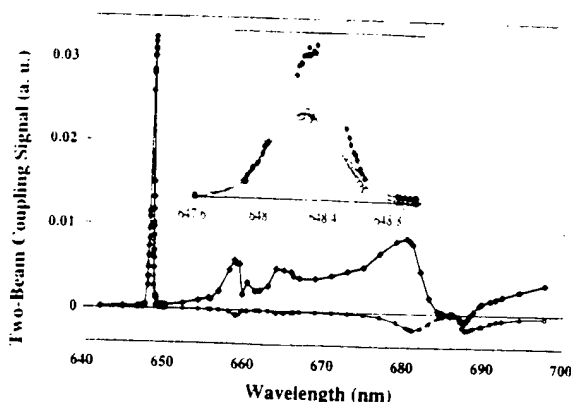
Fig. 4. Plot of the dispersive (filled diamonds) and absorptive (open circles) amplitudes of the TBC signals in 5% Tm:LiYF$_4$ versus wavelength over a broad spectral region containing both ground- and excited-state transitions. Inset: Enlargement of the avalanche resonance region at 648 nm. The slight skewing of the dispersive component line shape with respect to the absorptive component is due to the summation of ground- and excited-state polarization contributions. Data are uncorrected for sample absorption.

to reduce common mode intensity noise by 40 dB. The samples were single crystals of Tm:LiYF$_4$ with concentrations of 1–12%. The strongest avalanche response free of thermal grating contributions was obtained in a 1.5% sample 5 mm in length, which we used to measure the intensity dependence reported here. A 5% sample 3 mm in length was used for all the wide-spectral-range measurements. Typical spectra recorded at various intensities are shown in Fig. 2. A striking feature of these data is the rapid rise in nonlinear response above a well-defined threshold intensity near 20 kW/cm^2. The shapes of individual spectral traces are well described by the superposition of absorptive and dispersive components for a single nonlinear resonance.[3]

The values of n_2' and n_2'' determined from TBC analysis are shown in Fig. 3. An abrupt rise in nonlinear response occurs just above the avalanche threshold at 20 kW/cm^2. Then, in the range 40–100 kW/cm^2, both the real and the imaginary parts diminish slowly because of saturation.[14] The most interesting aspect of these data is that the real part n_2' of the induced index is much larger than the imaginary part n_2''. This behavior is contrary to predictions of resonant response in a two-level system.

These characteristics are nevertheless exactly these predicted by Eq. (4) when processes such as cross relaxation exist that permit incoherent pumping of an excited state in the presence of off-resonant excitation of ground-state centers. Figure 1(a) clearly shows the change in nonlinear response predicted by our model when incident light is tuned to a ground-state absorption resonance ($\Delta = 0$) or to an excited-state resonance ($\Delta' = 0 \leftrightarrow \Delta = 20$). These results are in excellent agreement with measurements (Fig. 4) that show that n_2' is zero at the 686.5 nm ground-state resonance but nonzero and dominant at the 648.2-nm excited-state (avalanche) resonance.

Our results show that the avalanche nonlinearity observed in Tm:LiYF$_4$ at 648.2 nm gives rise to beam coupling with a sharp threshold and a dispersive character at room temperature. The real and the imaginary parts of the induced nonlinear index have large magnitudes, of the order of 10^{-14} m^2/W. The real index goes to zero as expected at ground-state resonant wavelengths but is large and dominant over the imaginary index at the excited-state (avalanche) resonance. This behavior is consistent with a simple density-matrix model, which reveals that the dispersive character of the nonlinear susceptibility is a general feature of any system that experiences significant pumping of an excited state at large detunings from any ground-state resonance. This dispersive nonlinearity could provide a new passive self-mode-locking mechanism for avalanche upconversion lasers and presents an intrinsic limitation to gain in avalanche upconversion fiber amplifiers.

References

1. M. A. Kramer, W. R. Tompkin, and R. W. Boyd, Phys. Rev. A **34**, 2026 (1986); I. McMichael, P. Yeh, and P. Beckwith, Opt. Lett. **13**, 500 (1988).
2. S. A. Boothroyd, J. Chrostowski, and M. S. O'Sullivan, J. Opt. Soc. Am. B **6**, 766 (1989).
3. D. Redman, Q. Shu, A. Lenef, and S. C. Rand, Opt. Lett. **17**, 175 (1992).
4. J. Chivian, W. Case, and D. Eden, Appl. Phys. Lett. **35**, 124 (1979).
5. H. Ni, "Avalanche upconversion in Tm:LiYF$_4$, TmYAlO$_3$ and Tm:YAG," Ph.D. dissertation (University of Michigan, Ann Arbor, Mich., 1994).
6. See, for example, Y. R. Shen, *The Principles of Nonlinear Optics* (Wiley, New York, 1984).
7. A. Kueny, W. E. Case, and M. E. Koch, J. Opt. Soc. Am. B **6**, 639 (1989).
8. W. E. Case, M. E. Koch, and A. W. Kueny, J. Lumin. **45**, 351 (1990); U. Oetliker, M. J. Riley, P. S. May, and H. U. Gudel, Coord. Chem. Rev. **111**, 125 (1991); M. F. Joubert, S. Guy, and B. Jacquier, Phys. Rev. B **48**, 10031 (1993).
9. H. Ni and S. C. Rand, Opt. Lett. **16**, 1424 (1991).
10. T. Hebert, R. Wannemacher, R. M. Macfarlane, and W. Lenth, Appl. Phys. Lett. **60**, 2592 (1992); Y. H. Chen and F. Auzel, Electron. Lett. **30**, 1602 (1994); M. Pollnau, W. Luthy, and H. P. Weber, J. Appl. Phys. **77**, 6128 (1995); R. Scheps, IEEE J. Quantum Electron. **31**, 309 (1995).
11. T. Sandrock, E. Heumann, and G. Huber, in *International Quantum Electronics Conference* (Optical Society of America, Washington, D.C., 1996).
12. L. M. Yang, T. Sonsnowski, M. L. Stock, T. B. Norris, J. Squier, G. Mourou, M. L. Dennis, and I. Duling, Opt. Lett. **20**, 1044 (1995).
13. H. Ni and S. C. Rand, Opt. Lett. **17**, 1222 (1992).
14. Q. Shu, "Cooperative optical nonlinearities," Ph.D. dissertation (University of Michigan, Ann Arbor, Mich., 1996).
15. ρ_r can be calculated by use of the standard four-level model,[8] as we have done, or it can be treated as a free parameter.

Critical slowing down and dispersion of avalanche upconversion dynamics

Q. Shu and S. C. Rand

Division of Applied Physics, 1049 Randall Laboratory, University of Michigan, Ann Arbor, Michigan 48109-1120

(Received 23 September 1996)

The temporal response time on an avalanche upconversion transition is shown to undergo critical slowing down near the avalanche threshold. Also, the nonlinear refractive index is predominantly real, despite the resonant nature of the avalanche phenomenon. These findings are in excellent agreement with density-matrix analyses showing that cross relaxation dramatically alters the effective excited-state lifetime and that off-resonance absorption curiously dominates the wavelength dependence of the nonlinear refractive index. [S0163-1829(97)04214-8]

I. INTRODUCTION

Since its discovery,[1] avalanche upconversion has been of interest for solid-state lasers[2] because of the strong absorption it generates in spectral regions normally devoid of ground-state optical transitions in concentrated rare-earth and transition-metal crystals. Materials displaying the avalanche phenomenon universally exhibit cross-relaxation dynamics in connection with an excited-state optical resonance. By tuning light into coincidence with an excited-state absorption resonance and providing sufficient power density to exceed the avalanche threshold, intense luminescence can be generated at wavelengths shorter than the incident one.

Most earlier investigations focused on population inversion conditions in avalanche systems. Only a few studies have examined the nonlinear response[3,4] associated with avalanche dynamics. In an earlier publication,[5] we reported measurements of nonlinear refractive indices as a function of incident intensity, using a two-beam coupling approach. Here we describe experimental observations of a previously unreported characteristic[6] of avalanche nonlinearities, namely critical slowing down of the effective response time. We furnish the theoretical basis necessary to understand this result, together with a detailed explanation of the frequency dependence of the nonlinear refractive index. Avalanche upconversion is shown to be an example of surprising, but quite general, dynamics in which the refractive index changes associated with polarization on an excited-state resonance are primarily real, controlled by the off-resonant contributions from weak ground-state absorption.

II. THEORY

A. Steady-state dynamics

To formulate time-dependent analysis of dynamics in an avalanche system, it is first necessary to establish a steady-state description of the occupation of energy levels. To this end we begin by considering the atomistic model of the avalanche process illustrated in Fig. 1. The basic dynamics consist of excitation on an excited-state transition, followed by internal relaxation to a level which participates in cross relaxation with a second atom in its ground state. The Hamiltonian for such a system can be written as $H = H_0 + H_{int}$ where H_0 is the unperturbed Hamiltonian and H_{int} describes

its interaction with the field ($H_{atom\text{-}field} = -\mu \cdot E$) and with other atoms ($H_{atom\text{-}atom}$). Treating relaxation processes other than cross relaxation phenomenologically, the equation of motion for the density matrix is

$$i\hbar\dot{\rho} = [H,\rho] + \text{relaxation terms.} \quad (1)$$

Hence equations for the temporal evolution of individual elements of the density matrix are

$$\dot{\rho}_{11} = \gamma_2\rho_{22} + \gamma_{31}\rho_{33} + \gamma_{41}\rho_{44} - \alpha\rho_{11}\rho_{33}$$
$$+ \beta\rho_{22}^2 - BI(\rho_{11} - \rho_{33}), \quad (2)$$

$$\dot{\rho}_{22} = -\gamma_2\rho_{22} + \gamma_{32}\rho_{33} + \gamma_{42}\rho_{44} + 2\alpha\rho_{11}\rho_{33}$$
$$- 2\beta\rho_{22}^2 - iV_{24}\rho_{42} + iV_{42}\rho_{24}, \quad (3)$$

$$\dot{\rho}_{33} = -\gamma_3\rho_{33} + \gamma_{43}\rho_{44} - \alpha\rho_{11}\rho_{33} + \beta\rho_{22}^2 + BI(\rho_{11} - \rho_{33}), \quad (4)$$

$$\dot{\rho}_{44} = -\gamma_4\rho_{44} + iV_{42}\rho_{24} - iV_{24}\rho_{42}, \quad (5)$$

$$\dot{\rho}_{24} = (i\omega_{42} - \Gamma_{42})\rho_{24} - iV_{24}(\rho_{44} - \rho_{22}), \quad (6)$$
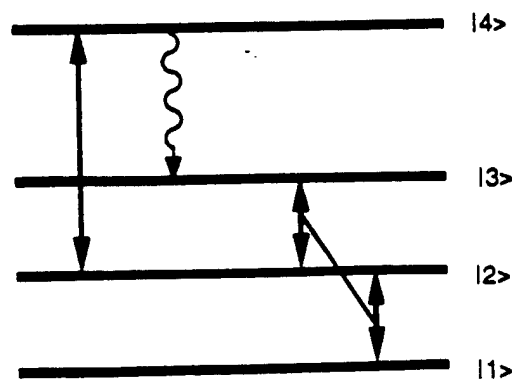

FIG. 1. Schematic illustration of the basic dynamics in the avalanche model. Absorption of light on the transition between states |2) and |4) is followed by internal relaxation to state |3) from which cross relaxation with a ground-state neighbor can occur.

$$\rho_{42} = \rho_{24}^{*}. \tag{7}$$

In these equations, ω_{42} is the optical transition frequency between state $|2\rangle$ and $|4\rangle$, the γ_i is the population decay rate of level i ($i=2,3,4$), Γ_{42} is the dephasing rate of the optical transition (including dephasing caused by energy migration), α is the cross-relaxation coefficient, and β is the coefficient for the reverse reaction. B is the Einstein coefficient of stimulated absorption and emission, and I is the input intensity.

Taking the input field to be of the form $E = \widetilde{E} e^{-i\omega t} + \text{c.c.}$, the matrix element of the atom-field interaction in the rotating wave approximation can be written as

$$V_{24} = V_{42}^{*} = \langle 2|H_{\text{atom-field}}|4\rangle = \tfrac{1}{2}\,\Omega_{24} e^{i\omega t}. \tag{8}$$

The quantity $\Omega_{24} = -2\mu_{24}\widetilde{E}^{*}/\hbar$ is related to the intensity according to

$$I = \frac{1}{2}\,\varepsilon c|2\widetilde{E}|^2 = \frac{\varepsilon c\hbar^2}{2\mu_{24}^2}|\Omega_{24}|^2, \tag{9}$$

where $\mu_{24} = \langle 2|-e\mathbf{r}|4\rangle$ is the transition dipole moment, ε is the dielectric constant of the medium, c is the speed of light in vacuum, and $\hbar$ is Planck's constant.

In a closed system we can easily solve for steady-state behavior. The results are

$$\rho_{44} = f\rho_{22}, \tag{10}$$

$$\rho_{33} = k\rho_{22} + \tfrac{1}{2}g, \tag{11}$$

$$\rho_{22} = \frac{-a_1 - \sqrt{a_1^2 - 4a_2 a_0}}{2a_2}. \tag{12}$$

The ground-state occupation is determined by the closure relation $\rho_{11} + \rho_{22} + \rho_{33} + \rho_{44} = 1$. For convenience in simplifying these expressions, several parameters have been introduced:

$$f = \frac{1/2|\Omega_{24}|^2\Gamma_{42}/\gamma_4}{\Delta^2 + \Gamma_{42}^2 + 1/2|\Omega_{24}|^2\Gamma_{42}/\gamma_4}, \tag{13}$$

$$g = \frac{4B'|\Omega_{24}|^2}{\gamma_3 + \gamma_{31} + 4B'|\Omega_{24}|^2}, \tag{14}$$

$$k = -g\,\frac{1+f}{2} + \frac{(\gamma_{43}-\gamma_{41})f - \gamma_2}{\gamma_3 + \gamma_{31}}(1-g), \tag{15}$$

$$a_0 = g[\alpha(1 - \tfrac{1}{2}g) + \tfrac{1}{2}\gamma_{32}], \tag{16}$$

$$a_1 = -\gamma_2 - (\gamma_{41} + \gamma_{43})f + [\gamma_{32} + 2\alpha(1-g)]k - \alpha g(1+f), \tag{17}$$

$$a_2 = -2\alpha(1 + f + k)k - 2\beta. \tag{18}$$

The quantity B' in Eq. (14) is a scaled Einstein coefficient given by $B' = BI/|\Omega_{24}|^2$.

Notice that the quantity g is related to the off-resonance absorption rate. As g approaches zero, the appearance of avalanche emission above a certain intensity becomes more and more abrupt, although the value of the threshold intensity changes very little. In the limit $g=0$, the occupation of the excited state can be written as

$$\rho_{22} = \frac{-a_1 - |a_1|}{2a_2}. \tag{19}$$

Clearly, for $a_1 < 0$ one obtains $\rho_{22} = 0$, whereas for $a_1 > 0$ one finds the nonzero value $\rho_{22} = -a_1/a_2$, and the excited state becomes occupied. In this limit the boundary of the dynamical phase transition which occurs at avalanche threshold is well defined and given simply by the condition $a_1 = 0$. The threshold does not depend sensitively on detuning from the ground-state transition under these conditions, but does depend strongly on detuning from the excited-state resonance. When dephasing and detuning are included, the threshold condition for avalanche occurrence can be given in terms of a threshold value for f which is

$$f_{\text{th}} = \frac{\gamma_2(\alpha + \gamma_3)}{(\alpha - \gamma_{31})(\gamma_{43} - \gamma_{41}) - (\gamma_3 + \gamma_{31})\gamma_{41}}. \tag{20}$$

To complete these results we add the solution for the off-diagonal element ρ_{24}, which is of the form $\rho_{24} = \widetilde{\rho}_{24} e^{i\omega t}$, $\widetilde{\rho}_{24}$ being its slowly varying amplitude. Writing out this amplitude explicitly in terms of real and imaginary parts according to $\widetilde{\rho}_{24} = u + iv$, the expectation value of the atomic polarization can then be determined from the relation

$$p(t) = \text{Tr}(\rho\mu) = \mu_{24}(u - iv)e^{-i\omega t} + \text{c.c.}, \tag{21}$$

for wavelengths in the vicinity of the avalanche transition. The solutions for u and v are given by

$$u = \frac{\Delta\gamma_4}{\Omega_{24}\Gamma_{42}}f\rho_{22}, \tag{22}$$

$$v = \frac{\gamma_4}{\Omega_{24}}f\rho_{22}. \tag{23}$$

The macroscopic nonlinear polarization density $P(t) = Np(t)$ has a slowly varying amplitude given by $\widetilde{P}(\omega) = N\mu_{24}(u - iv)$ from which the effective nonlinear susceptibility can be determined. This is accomplished by first identifying the full nonlinear susceptibility $\chi^{(\text{NL})}$ according to the relation $\widetilde{P}^{(\text{NL})}(\omega) = \chi^{(\text{NL})}(\omega)\widetilde{E}(\omega)$, and then picking out the effective susceptibility $\chi_{\text{eff}}^{(3)}(\omega)$ using the correspondence $\chi^{(\text{NL})}(\omega)\widetilde{E}(\omega) = \chi_{\text{eff}}^{(3)}|\widetilde{E}(\omega)|^2 E(\omega)$. The resulting expression for the effective third-order susceptibility is

$$\chi_{\text{eff}}^{(3)}(\omega) = -N\frac{\hbar\gamma_4 f\rho_{22}}{2\Gamma_{24}|\widetilde{E}|^4}(\Delta - i\Gamma_{24}). \tag{24}$$

Notice that the real part of this expression is zero exactly on resonance ($\Delta = 0$). This is the usual expectation for optical response in two-level systems.[7]

B. Time-dependent dynamics

For an avalanche system which is not in a steady state, the nonlinear nature of the dynamical equations suggests that numerical techniques must be used to solve for system evo-
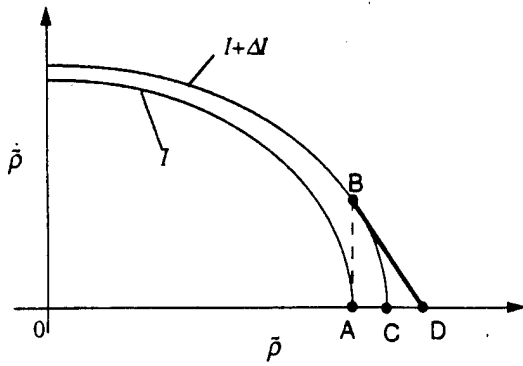
FIG. 2. Phase diagram of temporal evolution in a nonlinear dynamic system, illustrating the idea of linearization of the equation of motion for the density matrix ρ. Initially the system resides in state A, but is perturbed by an intensity change which causes to become nonzero. The system subsequently evolves to state C, for which point D is an adequate approximation for small ΔI.

lution. However when changes are slow or small, an analytic approach is still possible, based on linearization of the dynamical equations.[8]

The basis for the linearization method is illustrated in Fig. 2. This diagram shows a $(\dot{\rho},\bar{\rho})$ phase space of solutions to the equations of motion of the density matrix for two input intensities I and $I+\Delta$. Initially, the system resides in steady state A. When a small intensity step ΔI is applied to the system at $t=0$, its state is displaced to B and subsequently follows a nonlinear trajectory to reach a new steady state C, as time progresses. If ΔI is small enough, we can approximate this evolution using the tangent at B. Then, the line BD replaces the nonlinear trajectory, permitting us to find a linear approximation for the new steady state of the system. Final results were obtained by successive approximations in the limit of $\Delta I \to 0$.

In the rate equation limit, the earlier dynamical equations become

$$\dot{\rho}_{22} = -\gamma_2\rho_{22} + \gamma_{32}\rho_{33} + \gamma_{42}\rho_{44} + 2\alpha\rho_{11}\rho_{33} - 2\beta\rho_{22}^2$$
$$- B_{24}I(\rho_{22} - \rho_{44}), \qquad (25)$$

$$\dot{\rho}_{33} = -\gamma_3\rho_{33} + \gamma_{43}\rho_{44} - \alpha\rho_{11}\rho_{33} + \beta\rho_{22}^2 + B_{13}I(\rho_{11} - \rho_{33}), \qquad (26)$$

$$\dot{\rho}_{44} = -\gamma_4\rho_{44} + B_{24}I(\rho_{22} - \rho_{44}), \qquad (27)$$

B_{24} and B_{13} are the effective pumping rates on transitions $|2\rangle \to |4\rangle$ and $|1\rangle \to |3\rangle$, respectively.

Locally linearized versions of these equations[9] are obtained with the following substitutions:

$$\dot{\rho}_{ii} \to [\dot{\rho}_{ii} + \dot{\rho}_{ii}(0)]/2, \qquad (28)$$

$$\rho_{ii}\rho_{jj} \to [\rho_{ii}\rho_{jj}(0) + \rho_{ii}(0)\rho_{jj}]/2, \qquad (29)$$

$$\rho_{ii} \to [\rho_{ii} + \rho_{ii}(0)]/2 \qquad (30)$$

Indices i,j can both take on the values 2, 3, or 4. After substitution, the equations become

$$\dot{\rho}_{22} = a_{22}\rho_{22} + a_{23}\rho_{33} + a_{24}\rho_{44} + c_2, \qquad (31)$$

$$\dot{\rho}_{33} = a_{32}\rho_{22} + a_{33}\rho_{33} + a_{34}\rho_{44} + c_3, \qquad (32)$$

$$\dot{\rho}_{44} = a_{42}\rho_{22} + a_{43}\rho_{33} + a_{44}\rho_{44} + c_4. \qquad (33)$$

The coefficients are defined as follows:

$$a_{22} = -[\gamma_2 + B_{24}I + 4\beta\rho_{22}(0) + 2\alpha\rho_{33}(0)], \qquad (34)$$

$$a_{23} = \gamma_{32} + 2\alpha - 2\alpha\rho_{22}(0) - 4\alpha\rho_{33}(0) - 2\alpha\rho_{44}(0), \qquad (35)$$

$$a_{24} = \gamma_{42} + B_{24}I - 2\alpha\rho_{33}(0), \qquad (36)$$

$$c_2 = -(\gamma_2 + B_{24}I)\rho_{22}(0) + (\gamma_{32} + 2\alpha)\rho_{33}(0)$$
$$+ (\gamma_{42} + B_{24}I)\rho_{44}(0) - \dot{\rho}_{22}(0), \qquad (37)$$

$$a_{32} = -[B_{13}I - 2\beta\rho_{22}(0) - \alpha\rho_{33}(0)], \qquad (38)$$

$$a_{33} = -[\gamma_3 + 2B_{13}I + \alpha - \alpha\rho_{22}(0) - 2\alpha\rho_{33}(0) - \alpha\rho_{44}(0)], \qquad (39)$$

$$a_{34} = \gamma_{43} - B_{13}I + \alpha\rho_{33}(0), \qquad (40)$$

$$c_3 = 2B_{13}I - B_{13}I\rho_{22}(0) - (\gamma_3 + 2B_{13}I + \alpha)\rho_{33}(0)$$
$$+ (\gamma_{43} - B_{13}I)\rho_{44}(0) - \dot{\rho}_{33}(0), \qquad (41)$$

$$a_{42} = B_{24}I, \qquad (42)$$

$$a_{43} = 0, \qquad (43)$$

$$a_{44} = -\gamma_4 - B_{24}I, \qquad (44)$$

$$c_4 = B_{24}I\rho_{22}(0) - (\gamma_4 + B_{24}I)\rho_{44}(0) - \dot{\rho}_{44}(0). \qquad (45)$$

Initial population densities required for the coefficients in Eqs. (31)–(33) are determined by steady-state values acquired prior to $t=0$ as determined in Sec. II A, for a specified intensity level. Initial time derivatives are calculated by substituting these initial populations directly into Eqs. (25)–(27).

The equations of motion can now be written in a convenient matrix form:

$$\dot{\rho} = A\rho + \mathbf{c}. \qquad (46)$$

Here

$$\rho = \begin{pmatrix} \rho_{22} \\ \rho_{33} \\ \rho_{44} \end{pmatrix}, \quad A = \begin{pmatrix} a_{22} & a_{23} & a_{24} \\ a_{32} & a_{33} & a_{34} \\ a_{42} & a_{43} & a_{44} \end{pmatrix}, \quad \mathbf{c} = \begin{pmatrix} c_2 \\ c_3 \\ c_4 \end{pmatrix}.$$

Applying the method of Laplace transforms, and representing the transform of ρ by $\mathbf{R}(s)$, the equation of motion yields

$$s\mathbf{R}(s) - \rho(0) = A\mathbf{R}(s) + \frac{1}{s}\mathbf{c}. \qquad (47)$$

The Laplace transform of the solution is therefore

$$\mathbf{R}(s) = (S - A)^{-1}\left[\rho(0) + \frac{1}{s}\mathbf{c}\right], \qquad (48)$$

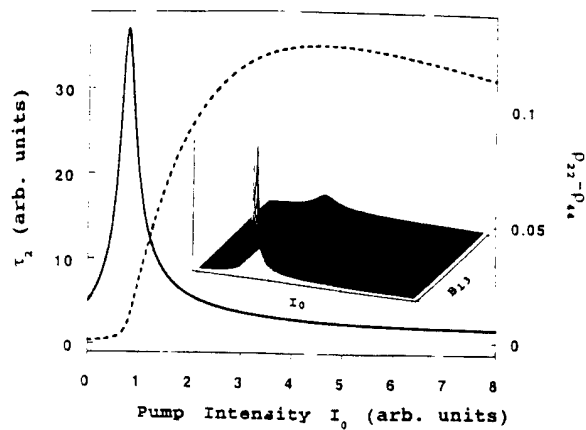where S is s times the unit matrix and $\rho(0)$ is the initial value of ρ.

FIG. 3. The effective relaxation time of state $|2\rangle$ versus input intensity. The population difference $(\rho_{22}-\rho_{44})$ is graphed for direct comparison of the peak in the time constant with the threshold of avalanche absorption. Inset: Divergence of the response time τ_2 as the ground-state absorption rate B_{13} approaches zero, calculated numerically.

$\mathbf{R}(s)$ may be assumed to consist of a transient part and a steady-state part. That is, $\mathbf{R}(s)=\mathbf{R}^{tr}(s)+\mathbf{R}^{ss}(s)$. The steady-state part is readily identified as $\mathbf{R}^{ss}(s)=-(1/s)A^{-1}\mathbf{c}$ since $\rho(\infty)=\lim_{s\to 0}[s\mathbf{R}(s)]=-A^{-1}\mathbf{c}$. The remainder of the solution transform must be the transient response. Consequently, the ith element of this transient part of the vector $R^{tr}(s)$ is

$$R_i^{tr}(s)=\frac{m_i s^2+n_i s+l_i}{s^3+Ms^2+Ns+L}. \tag{49}$$

where m_i, n_i, l_i, M, N, and L are all functions of elements of A, defined in the Appendix.

In the long-time limit $(s\to 0)$, $R^{tr}(s)$ can be analyzed by partial fractions, or by the expansion of Eq. (49) to first order in s. Comparing the result

$$R_i^{tr}(s)=\frac{1}{L/l_i(N/L-n_i/l_i)}\frac{1}{s+\dfrac{1}{N/L-n_i/l_i}} \tag{50}$$

with the general form of a transformed exponential, namely $\mathcal{L}\{ce^{at}\}(s)=c(s-a)^{-1}$, where c and a are constants, we find an effective time constant of

$$\tau_i=\frac{N}{L}-\frac{n_i}{l_i} \tag{51}$$

for level i. Calculations of the effective time constant τ_2 (for level 2) versus intensity in Fig. 3 reveal a dramatic "slowing down" at the avalanche threshold. The inset of Fig. 3 shows that τ_2 in fact diverges at a critical intensity as the ground-state absorption rate B_{13} approaches zero. This is a key result of the present research.

C. Wavelength dependence

A significant limitation of conventional analyses of the avalanche effect is that off-resonant excitation from the ground state which provides the seed population in the absorptive excited state is ignored. This omission is justified when steady-state populations are the only quantities of in-
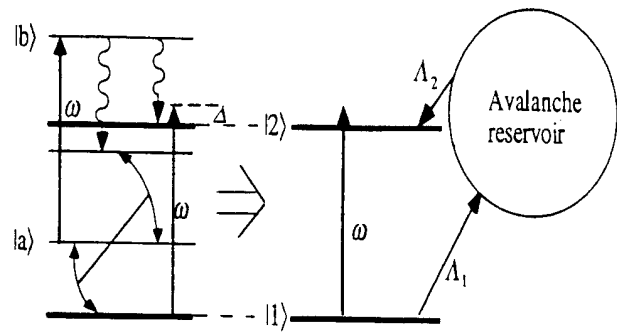

FIG. 4. A simplified model for the description of complex nonlinear susceptibility in avalanche systems. On the left is a multilevel sketch reflecting details of avalanche dynamics. On the right is a quasi-two-level model which retains aspects essential for understanding the nonlinear dispersion of avalanche nonlinearities.

terest, for they depend negligibly on initial conditions (such as excited-state occupation). However to understand the wavelength dependence of the nonlinear refractive indices, the nonlinear dispersion, it is necessary to account for the initial (ground-state) absorption step in the avalanche process because of a surprising enhancement of the off-resonant ground-state polarization by the large excited-state populations generated through avalanche cross relaxation.

In this section, the important role of the off-resonant absorption from the ground state which initiates the avalanche in determining polarization properties of the system is examined. Rather than calculating populations and polarizations from a five-level model which incorporates two optical transitions explicitly, it is very helpful to solve for the nonlinear dispersion in an equivalent two-step fashion using a quasi-three-level model which renders the basic physics much more obvious. To highlight the unexpectedly important role of the ground-state transition in determining nonlinear dispersion, we reduce the basic avalanche model to that shown on the right side of Fig. 4, in which all excited states but one are replaced by an incoherently pumped reservoir. The incoherent pumping rate Λ_1 is due exclusively to the nonradiative process of cross relaxation, whereas Λ_2 contains contributions from both cross relaxation and natural decay between levels. Both are functions of intensity. We show that detuning from the ground-state transition determines whether the nonlinear response is absorptive or dispersive.

After simplifying Eqs. (2)–(7) to reflect the model in Fig. 4, the equations of motion yield

$$\dot\rho_{11}=\gamma_{21}\rho_{22}-\Omega v-\Lambda_1=0, \tag{52}$$

$$\dot\rho_{22}=-\gamma_{21}\rho_{22}+\Omega v+\Lambda_2=0, \tag{53}$$

$$\dot{\tilde\rho}_{21}=-(\Gamma_{21}-i\Delta)\tilde\rho_{21}+\tfrac{1}{2}i\Omega(\rho_{22}-\rho_{11})=0. \tag{54}$$

$\Delta=\omega-\omega_{21}$ is the detuning of incident light at frequency ω from the transition frequency ω_{21} between levels. The closure relation $\rho_{11}+\rho_{22}+\rho_r=1$ accounts for the population density ρ_r circulating in the avalanche reservoir. The reservoir population ρ_r can serve as a free parameter or may be

determined explicitly from a multilevel model which takes the second photon interaction and cross relaxation into account. That is

$$\rho_r = \sum_i \rho_{ii}.$$

where i runs over the indices of levels other than $|1\rangle$ and $|2\rangle$ in the full, microscopic model.

Using R to denote the rate per atom of decay to level $|2\rangle$ from the reservoir, we can apply the steady-state relation $\Lambda_1 = \Lambda_2 = R\rho_r$ to solve Eqs. (52)–(54) for ρ_{11}, ρ_{22}, and ρ_{21}:

$$\rho_{11} = \frac{\Delta^2 + \Gamma_{21}^2 + 1/2|\Omega|^2\Gamma_{21}/\gamma_{21}}{\Delta^2 + \Gamma_{21}^2 + |\Omega|^2\Gamma_{21}/\gamma_{21}}$$

$$- \frac{(1 + R/\gamma_{21})(\Delta^2 + \Gamma_{21}^2) + 1/2|\Omega|^2\Gamma_{21}/\gamma_{21}}{\Delta^2 + \Gamma_{21}^2 + |\Omega|^2\Gamma_{21}/\gamma_{21}}\rho_r, \quad (55)$$

$$\rho_{22} = \frac{1/2|\Omega|^2\Gamma_{21}/\gamma_{21}}{\Delta^2 + \Gamma_{21}^2 + |\Omega|^2\Gamma_{21}/\gamma_{21}}$$

$$+ \frac{(\Delta^2 + \Gamma_{21}^2)R/\gamma_{21} - 1/2|\Omega|^2\Gamma_{21}/\gamma_{21}}{\Delta^2 + \Gamma_{21}^2 + |\Omega|^2\Gamma_{21}/\gamma_{21}}\rho_r, \quad (56)$$

$$\tilde{\rho}_{21} = \frac{(1/2)\Omega(\Delta - i\Gamma_{21})}{\Delta^2 + \Gamma_{21}^2 + |\Omega|^2\Gamma_{21}/\gamma_{21}} - \frac{(1/2)Q(\Delta - i\Gamma_{21})}{\Delta^2 + \Gamma_{21}^2 + |\Omega|^2\Gamma_{21}/\gamma_{21}}$$

$$\times \left(1 + \frac{2R}{\gamma_{21}}\right)\rho_r. \quad (57)$$

The effective susceptibility may be determined from $\tilde{P}(\omega) = \varepsilon_0\chi_{\text{eff}}(\omega)\tilde{E}$. By decomposing the expression for $\chi_{\text{eff}}(\omega)$ into linear and nonlinear parts using $\chi_{\text{eff}}(\omega) = \chi^{(1)}(\omega) + \chi_{\text{eff}}^{(3)}(\omega)|\tilde{E}|^2$, where the linear portion is given by the usual expression

$$\chi^{(1)}(\omega) = -\frac{N|\mu_{12}|^2\hbar^{-1}\varepsilon_0^{-1}(\Delta - i\Gamma_{21})}{\Delta^2 + \Gamma_{21}^2}.$$

the effective nonlinear susceptibility is found to be

$$\chi_{\text{eff}}^{(3)}(\omega) = \left[\frac{4N|\mu_{12}|^4\hbar^{-3}\varepsilon_0^{-1}(\Delta - i\Gamma_{21})\Gamma_{21}/\gamma_{21}}{(\Delta^2 + \Gamma_{21}^2)(\Delta^2 + \Gamma_{21}^2 + |\Omega|^2\Gamma_{21}/\gamma_{21})}\right.$$

$$+ \frac{4N|\mu_{12}|^4\hbar^{-3}\varepsilon_0^{-1}(\Delta - i\Gamma_{21})(1 + 2R/\gamma_{21})}{\Delta^2 + \Gamma_{21}^2 + |\Omega|^2\Gamma_{21}/\gamma_{21}}$$

$$\left. \times (\rho_r/|\Omega|^2)\right]. \quad (58)$$

Notice that this result is quite different from the effective susceptibility in Eq. (24), which overlooked the ground-state transition. At the avalanche resonance, the excited-state detuning Δ' is zero. This means $\Delta' = \omega - \omega_{ba} = \Delta - (\omega_{ba} - \omega_{21}) = 0$, with the result that $\Delta = \omega_{ba} - \omega_{21}$. Under these conditions, the reservoir population is maximized and the real component of the nonlinear susceptibility is large *on resonance*. In fact, whenever $\Delta = \omega_{ba} - \omega_{21} > \Gamma_{21}$, the real part exceeds the imaginary part exactly on resonance.
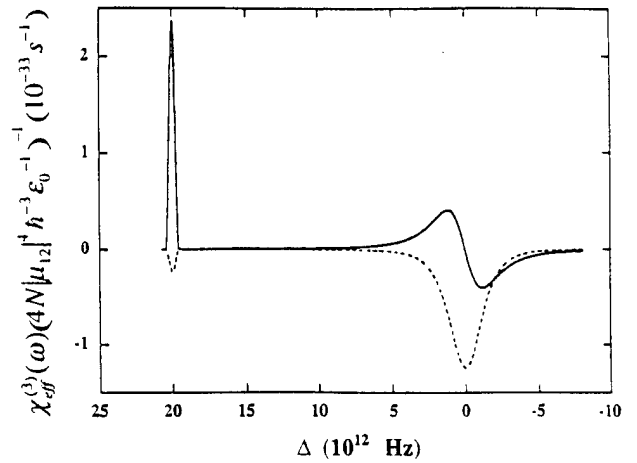

FIG. 5. Calculation of the real and imaginary components of an avalanche-induced nonlinear susceptibility. Parameters used in the calculation were $\Gamma_{21} = 2 \times 10^{12}$ s^{-1} and $\gamma_{21} = 2 \times 10^8$ s^{-1} (roughly appropriate for the $^3H_6 - ^3F_3$ transition), and $\omega_{ba} - \omega_{21} = 2 \times 10^{13}$ s^{-1}, $|\Omega|^2 = 3 \times 10^{18}$.

A direct comparison of the predicted behavior of nonlinear susceptibility components at a ground-state resonance $(\Delta = 0)$ and at an avalanche transition $(\Delta' = 0)$ is made in Fig. 5. For this plot, the reservoir population ρ_r was taken to have the steady-state value determined from the five-level model in the left side of Fig. 4. Notice that the real component passes through zero for $\Delta = 0$ (ground-state transition) whereas it exhibits a maximum for $\Delta' = 0$ (excited-state resonance). This is a second key result of the present research.

III. EXPERIMENT AND RESULTS

Avalanche upconversion can readily be observed in 1.5% Tm:LiYF$_4$ crystals at room temperature using dye laser excitation at 648 nm.[10] In this work we measured the nonlinear indices and characteristic response time of the avalanche nonlinearity in this material by a two-beam coupling technique. Details of the experimental method, analysis, and values of the induced indices have been described elsewhere.[11] Here we report on the temporal response and nonlinear dispersion over a wide wavelength range. Both these aspects of avalanche dynamics show unique features which provide an important basis for comparison with theory.

Figure 6 is a plot of the experimental response time measured in 1.5% Tm:LiYF$_4$ as a function of incident intensity. The avalanche threshold occurs at 1 W/cm^2. The important thing to notice is that both above and below the threshold intensity, the medium response is considerably faster than it is at the critical point. This indicates a dramatic slowing down of the effective lifetime of the absorptive excited state, right at the avalanche threshold.

By performing ultrahigh resolution scans of the beam-coupling spectrum at many different wavelengths in the red spectral region, additional results shown in Figs. 7 and 8 were obtained. The traces shown in Fig. 7 cover the region from the ground-state resonance near 688 nm to the excited-state resonance near 648 nm. It is immediately evident from the trend in their shapes, that the refractive index changes
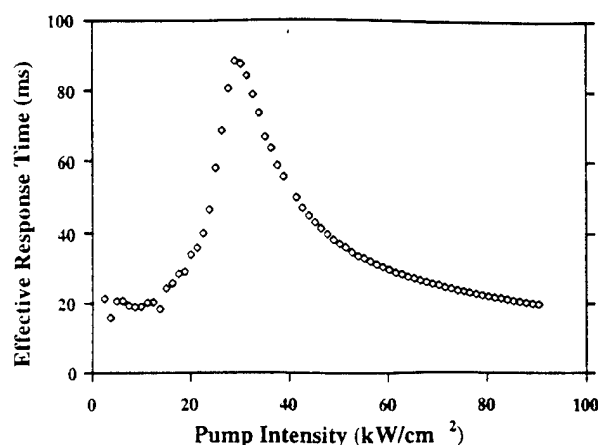
FIG. 6. Experimental response time of the avalanche medium versus intensity, obtained by two-beam coupling.

induced by incident light vary from primarily absorptive at 688 nm to primarily dispersive at 648 nm.

Quantitative analysis of the real and imaginary components[11] of these and other two-beam coupling spectra in the range 640–700 nm yielded the results shown in Fig. 8. In this figure it is somewhat easier to see that the real index goes through zero at the ground-state absorption resonance near 688 nm. By contrast, when the wavelength is tuned to the avalanche transition at 648 nm, the real index acquires a large value, exceeding the imaginary index by a factor of 2.
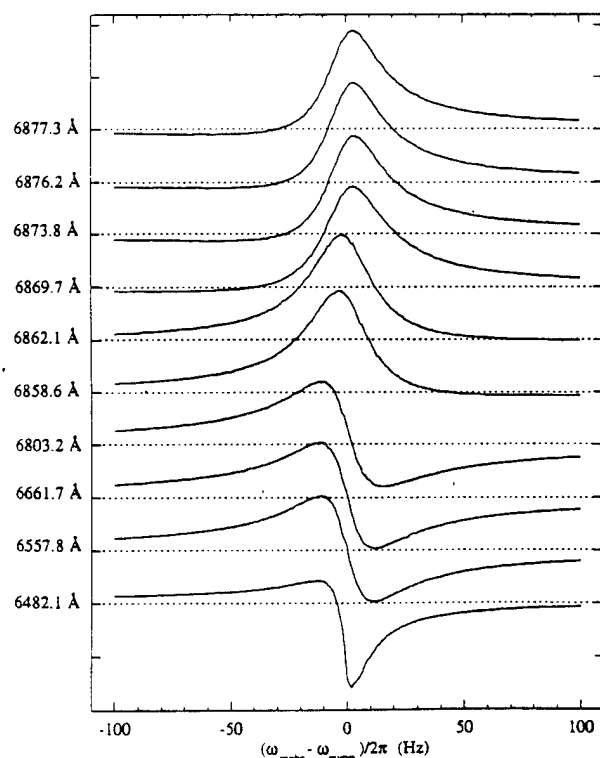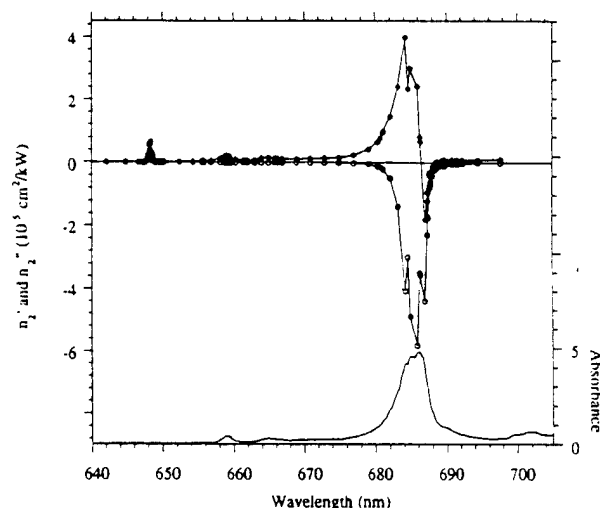

FIG. 8. Decomposition of the nonlinear susceptibilities determined by two beam coupling into real (diamonds) and imaginary parts (open circles). The spectral range includes an avalanche resonance at 648 nm and ground-state absorption at 688 nm. The lower trace gives the polarized absorption spectrum ($E \| C$) taken at room temperature which was used to correct the two-beam coupling signal in obtaining the nonlinear indices.

FIG. 7. Beam coupling spectra at different wavelengths between the ground-state absorption at 688 nm and the avalanche resonance at 648 nm.
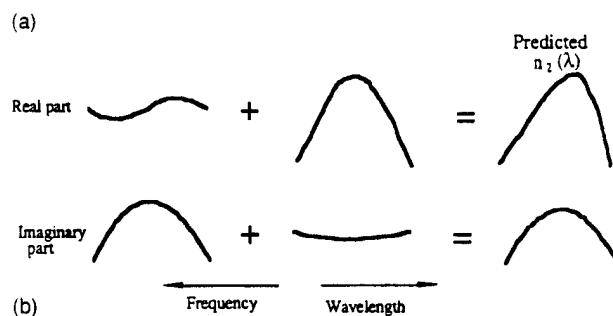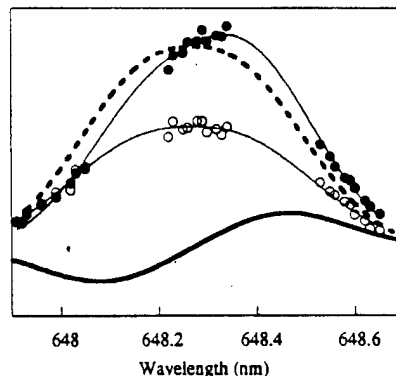

(a)

(b)

FIG. 9. (a) Decomposition of the real nonlinear index (filled circles) into symmetric and antisymmetric parts. The imaginary index is also shown (open circles), but is well described by a single Gaussian. Note the small relative shift between the experimental peaks of the two indices. (b) Schematic diagram showing the qualitative result of combining the nonlinear response associated with both optical transitions giving rise to avalanche absorption.

IV. DISCUSSION

The significant increase that is observed in optical response time at avalanche threshold typifies behavior of systems undergoing magnetic[12] or structural[13] phase transitions. It is well known, for example, that the characteristic time of spin correlations in interacting spin systems undergoes critical slowing down[14] at order-disorder transitions. The phase transition in our system consists of the sudden appearance of an excited-state population above a critical intensity and occurs at the threshold intensity determined by Eq. (20). The temporal response time does indeed diverge ($\tau \to \infty$) as the ground-state absorption rate approaches zero. Hence we refer to this as critical slowing down. A spin analogy may be particularly apt, since optical cross relaxation, in which a first atom undergoes nonradiative deexcitation while a second, coupled atom conserves energy by making a dipole transition to an excited state, is formally equivalent to secular spin-spin interactions. The critical role of temperature in a spin-ordering transition is replaced here by a critical dependence on optical intensity. Certainly it would be interesting to explore adaptations of the continuous-spin Ising model to avalanche dynamics. Also, additional experiments of the type we have reported here should be very fruitful for more detailed studies of avalanche critical exponents and phenomena.

Figure 9(a) shows the result of a decomposition of the measured indices into polarization contributions arising from the two optical transitions in the problem. Figure 9(b) shows schematically how the two contributions add to give a slightly asymmetric real component and an imaginary component which is diminished by an excited-state contribution of opposite sign. Notice that the decomposition accounts satisfactorily for the slight asymmetry observed in the real index peak. The real index peak is shifted with respect to the imaginary index curve due to a small dispersively shaped contribution from the resonant excited-state transition.

These findings are in excellent agreement with the quasi-two-level theory of Sec. II C. Because details of the cross-relaxation dynamics are omitted in this model of nonlinear dispersion, it can be concluded that the predominantly real nonlinear susceptibility encountered in our experiments at the excited-state absorption resonance is not limited to avalanche systems. Rather, it is a property of all systems in which excitation greatly detuned from any ground-state transition nevertheless generates large excited-state populations. Avalanche systems provide merely one example where this occurs, with the cross-relaxation dynamics constituting the mechanism whereby excited states develop large populations nonradiatively.

ACKNOWLEDGMENT

APPENDIX

Explicit expressions for the quantities in Eq. (49) are

$$m_2 = x^{-1}[-a_{33}a_{44}c_2 + a_{23}a_{44}c_3 + (a_{24}a_{33} - a_{23}a_{34})c_4] + \rho_{22}(0),\tag{A1}$$

$$m_3 = x^{-1}[(a_{32}a_{44} - a_{42}a_{34})c_2 + (a_{42}a_{24} - a_{22}a_{44})c_3 + (a_{34}a_{22} - a_{24}a_{32})c_4] + \rho_{33}(0),\tag{A2}$$

$$m_4 = x^{-1}[a_{42}a_{33}c_2 - a_{23}a_{42}c_3 + (a_{32}a_{23} - a_{22}a_{33})c_4] + \rho_{44}(0),\tag{A3}$$

$$n_2 = x^{-1}[(a_{33}^2 a_{44} + a_{33}a_{44}^2 + a_{32}a_{23}a_{44} - a_{42}a_{23}a_{34} + a_{42}a_{24}a_{33})c_2 - a_{23}a_{44}(a_{22} + a_{33} + a_{44})c_3$$
$$+ (a_{23}a_{34} - a_{24}a_{33})(a_{22} + a_{33} + a_{44})c_4 - (a_{33} + a_{44})x\rho_{22}(0)] + a_{23}\rho_{33}(0) + a_{24}\rho_{44}(0),\tag{A4}$$

$$n_3 = x^{-1}[(a_{42}a_{34} - a_{32}a_{44})(a_{22} + a_{33} + a_{44})c_2 + (a_{32}a_{23}a_{44} - a_{42}a_{23}a_{34} - a_{24}a_{42}a_{22} - a_{44}a_{42}a_{24} + a_{22}^2 a_{44} + a_{44}^2 a_{22})c_3$$
$$+ (a_{24}a_{32} - a_{34}a_{22})(a_{22} + a_{33} + a_{44})c_4] + a_{32}\rho_{22}(0) - (a_{22} + a_{44})\rho_{33}(0) + a_{34}\rho_{44}(0),\tag{A5}$$

$$n_4 = x^{-1}[-a_{42}a_{33}(a_{22} + a_{33} + a_{44})c_2 + a_{23}a_{42}(a_{22} + a_{33} + a_{44})c_3 + (a_{22}^2 a_{33} + a_{42}a_{24}a_{33} + a_{22}a_{33}^2 - a_{32}a_{23}a_{22} - a_{33}a_{32}a_{23}$$
$$- a_{42}a_{23}a_{34})c_4] + a_{42}\rho_{22}(0) - (a_{22} + a_{33})\rho_{44}(0),\tag{A6}$$

$$l_2 = x^{-1}[(-a_{33}^2 a_{44}^2 + a_{44}a_{42}a_{23}a_{34} + a_{33}a_{42}a_{23}a_{34} - a_{33}^2 a_{42}a_{24} - a_{44}^2 a_{32}a_{23})c_2 + a_{23}(-a_{42}a_{23}a_{34} - a_{44}a_{42}a_{24} + a_{42}a_{24}a_{33} + a_{44}^2 a_{22}$$
$$+ a_{33}a_{44}^2)c_3 + (a_{24}a_{33}^2 a_{22} + a_{23}^2 a_{34}a_{32} + a_{24}a_{32}a_{23}a_{44} - a_{23}a_{34}a_{22}a_{33} - a_{23}a_{34}a_{22}a_{44} - a_{23}a_{34}a_{33}a_{44} + a_{24}a_{33}^2 a_{44}$$
$$- a_{24}a_{33}a_{32}a_{23})c_4] + a_{33}a_{44}\rho_{22}(0) - a_{23}a_{44}\rho_{33}(0) + (a_{23}a_{34} - a_{24}a_{33})\rho_{44}(0),\tag{A7}$$

$$l_3 = x^{-1}[(a_{32}a_{44}^2a_{22} + a_{32}a_{44}^2a_{33} - a_{32}a_{44}a_{42}a_{24} + a_{32}a_{42}a_{24}a_{33} - a_{34}a_{42}a_{22}a_{33} - a_{34}a_{42}a_{22}a_{44} - a_{34}a_{42}a_{33}a_{44} + a_{34}a_{42}^2a_{24})c_2$$

$$+ (-a_{24}a_{42}a_{32}a_{23} - a_{34}^2a_{42}^2 - a_{22}^2a_{44}^2 + a_{22}a_{42}a_{23}a_{34} - a_{44}^2a_{32}a_{23} + a_{44}a_{42}a_{23}a_{34} + 2a_{24}a_{42}a_{22}a_{44})c_3 + (a_{34}a_{32}a_{23}a_{44}$$

$$- a_{34}^2a_{42}a_{23} + a_{34}a_{42}a_{24}a_{33} + a_{34}a_{22}^2a_{33} + a_{34}a_{22}^2a_{44} - a_{34}a_{22}a_{32}a_{23} - a_{34}a_{22}a_{42}a_{24} - a_{24}a_{32}a_{22}a_{33} - a_{24}a_{32}a_{22}a_{44}$$

$$- a_{24}a_{33}a_{32}a_{44} + a_{24}a_{32}^2a_{23} + a_{24}^2a_{32}a_{42})c_4] + (a_{42}a_{34} - a_{32}a_{44})\rho_{22}(0) + (a_{22}a_{44} - a_{42}a_{24})\rho_{33}(0) + (a_{24}a_{32} - a_{34}a_{22})\rho_{44}(0),$$

$$\text{(A8)}$$

$$l_4 = x^{-1}[a_{42}(-a_{42}a_{23}a_{34} - a_{33}a_{32}a_{23} + a_{22}a_{33}^2 + a_{33}^2a_{44} + a_{32}a_{23}a_{44})c_2 - a_{42}a_{23}(a_{22}a_{33} - a_{32}a_{23} + a_{22}a_{44} + a_{33}a_{44} - a_{42}a_{24})c_3$$

$$+ (-a_{33}^2a_{42}a_{24} + a_{22}a_{42}a_{23}a_{34} + a_{33}a_{42}a_{23}a_{34} - a_{24}a_{42}a_{32}a_{23} - a_{22}^2a_{33}^2 + 2a_{22}a_{33}a_{32}a_{23} - a_{32}^2a_{23}^2)c_4] - a_{42}a_{33}\rho_{22}(0)$$

$$+ a_{42}a_{23}\rho_{33}(0) + (a_{22}a_{33} - a_{32}a_{23})\rho_{44}(0).$$

$$\text{(A9)}$$

$$M = -(a_{22} + a_{33} + a_{44}), \tag{A10}$$

$$N = a_{22}a_{33} - a_{32}a_{23} + a_{22}a_{44} + a_{33}a_{44} - a_{24}a_{42}, \tag{A11}$$

$$L = x, \tag{A12}$$

where

$$x = a_{32}a_{23}a_{44} + a_{42}a_{24}a_{33} - a_{42}a_{23}a_{34} - a_{22}a_{33}a_{44}.$$

[1] J. Chivian, W. Case, and D. Eden, Appl. Phys. Lett. **35**, 124 (1979).

[2] M. E. Koch, A. W. Kueny, and W. E. Case, Appl. Phys. Lett. **56**, 1083 (1990); T. Hebert, R. Wannemacher, R. M. Macfarlane, and W. Lenth, *ibid.* **60**, 2592 (1992).

[3] A. Kueny, W. E. Case, and M. E. Koch, J. Opt. Soc. Am. B **6**, 639 (1989).

[4] Q. Shu, Ph.D. thesis, University of Michigan, 1996.

[5] Q. Shu, H. Ni, and S. C. Rand, Opt. Lett. **22**, 123 (1997).

[6] A preliminary report of these findings was given by Q. Shu and S. C. Rand, in *Proceedings of the Conference on Lasers and Electro-optics, Anaheim, California, 1996 (CLEO/QELS' 1996)* (Optical Society of America, Washington D.C., 1996).

[7] See, for example, S. Stenholm, *Foundations of Laser Spectroscopy* (Wiley, New York, 1984).

[8] M. F. Joubert, S. Guy, and B. Jacquier, Phys. Rev. B **48**, 10 031 (1993).

[9] P. Xie and S. Rand, J. Opt. Soc. Am. B **11**, 901 (1994).

[10] H. Ni and S. C. Rand, Opt. Lett. **16**, 1424 (1991).

[11] D. Redman, Q. Shu, A. Lenef, and S. C. Rand, Opt. Lett. **17**, 175 (1992).

[12] M. E. Fisher, Rev. Mod. Phys. **46**, 597 (1974).

[13] J. F. Scott, Rev. Mod. Phys. **46**, 83 (1974).

[14] For an excellent introduction to analogies in critical phenomena, see H. Haken, Rev. Mod. Phys. **47**, 67 (1975).